SPECIFIC HEAT AND MAGNETIC PROPERTIES OF Ni-Mn-In HEUSLER ALLOYS

A Dissertation

by

JING-HAN CHEN

Submitted to the Office of Graduate and Professional Studies of
Texas A&M University
in partial fulfillment of the requirements for the degree of

DOCTOR OF PHILOSOPHY

Chair of Committee,	Joseph H. Ross, Jr.
Committee Members,	Roland E. Allen
	Glenn Agnolet
	Raymundo Arróyave
Head of Department,	George R. Welch

August 2015

Major Subject: Applied Physics

ABSTRACT

The recent discovery of giant magnetocaloric effects (MCE) at around room temperature has triggered the possibility of the development of a magnetic refrigerator that operates at ambient temperature. One of the main characteristics of giant magnetocaloric materials is the existence of a first order magnetic phase transition coupled with variations of the lattice parameter. This causes a huge entropy change which can be utilized practically. The martensitic transformation in these materials can be driven by either sweeping the magnetic field or the temperature and this property provides the flexibility to design thermodynamic cycles. Therefore, investigation of the entropy and the cooling power generated across this martensitic transition becomes important for practical purposes. However, the details of the correlation between the martensitic transition and magneto-elastic coupling in giant MCE materials have not been completely understood.

Among new magnetocaloric materials, Ni-Mn-In Heusler alloys have attracted considerable attention as novel rare-earth free magnetic refrigerants. In order to fully understand the properties of the martensitic phase transition in Ni-Mn-In Heusler alloys and its influence on the MCE, we studied four well-characterized materials with nominal compositions $Ni_{50}Mn_{36}In_{14}$, $Ni_{50}Mn_{35.5}In_{14.5}$, $Ni_{48}Mn_{35}In_{17}$ and $Ni_{48}Mn_{38}In_{14}$, which differ in that the former two materials exhibit a paramagnetic to antiferromagnetic transition, whereas the others exhibit an additional ferromagnetic transition. We performed magnetization and field-dependent calorimetry measurements. The results provide a firm basis for the analytic evaluation of field-induced entropy changes and relative cooling power in these and related materials. We find that two of the samples ($Ni_{50}Mn_{36}In_{14}$ and $Ni_{50}Mn_{35.5}In_{14.5}$) include an additional entropy contribution beyond that due to magnetic spins due to the magneto-elastic coupling, which can be explained in terms of the renormalization of the phonon contributions. We also showed that the magnetization and calorimetry results give a consistent measure of antiferromagnetic plus superparamagnetic behavior of these materials to a model with Mn showing local moment behavior. The analysis provides a specific picture of the superparamagnetic properties of $Ni_{50}Mn_{36}In_{14}$ and the spin canting behavior of $Ni_{50}Mn_{35.5}In_{14.5}$. Further analysis of the relative cooling power provides a prediction which is shown to give a firm foundation for understanding the practical behavior of compositions with ferromagnetic and martensitic transformation nearly coinciding.

ACKNOWLEDGEMENTS

This thesis is based upon work supported by the National Science Foundation under Grant No. DMR-1108396, and by the Robert A. Welch Foundation (Grant No. A-1526).

NOMENCLATURE

MCE	Magnetocaloric effect
C_p	Specific heat under a constant pressure p
C_v	Specific heat under a constant volume v
RCP	Relative Cooling Power
k_B	Boltzmann constant
R	Gas constant
T_c	Curie temperature
T_N	Néel temperature
T_F	Fermi temperature
μ_B	Bohr magneton
PPMS	Physical Property Measurement System

TABLE OF CONTENTS

Page

ABSTRACT ii

ACKNOWLEDGEMENTS iv

NOMENCLATURE v

TABLE OF CONTENTS vi

LIST OF FIGURES viii

LIST OF TABLES xiv

1. MAGNETOCALORIC EFFECT 1

    1.1 Introduction 1
    1.2 Magnetic Refrigeration 2
    1.3 Magnetocaloric Materials 4
        1.3.1 Gd(Ge$_{1-x}$Si$_x$)$_4$ 4
        1.3.2 Ni-Mn-Z Heusler Alloys 6
        1.3.3 MnAs Based Compounds 7
        1.3.4 La(Fe,Si)$_{13}$ and Related Compounds 9
    1.4 Experimental Field-induced Isothermal Entropy 10
    1.5 Relative Cooling Power 11

2. MAGNETIC ORDER AND TRANSITION IN MATERIALS 13

    2.1 Paramagnetism 13
    2.2 Ferromagnetism 14
    2.3 Antiferromagnetism 15
    2.4 Field-cooled and Zero-field-cooled Measurements 19
    2.5 Thermodynamics of Phase Transitions 21
    2.6 Arrott Plot 21
    2.7 First Order Magnetic Transitions 24
        2.7.1 Clausius-Clapeyron Relation 26
        2.7.2 Model of Exchange-inversion Magnetization 28
        2.7.3 The Bean-Rodbell Model 30

3. MEASUREMENT METHODS FOR THE SPECIFIC HEAT 33

3.1 Introduction 33
3.2 Adiabatic Calorimetry 34
3.3 Differential Scanning Calorimetry 36
3.4 AC Calorimetry 36
3.5 Heat-pulse Method 38
    3.5.1 Simple Model 40
    3.5.2 Two-τ Model 41
    3.5.3 Across a First-order Transition 42

4. THEORETICAL ENTROPY CONTRIBUTIONS 46

4.1 Vibrational Contributions from Debye Model 46
4.2 Electronic Contributions in Metals 48
4.3 Magnetic Contribution 51

5. ENTROPY ENHANCEMENT OF GIANT MAGNETOCALORIC EFFECT 53

5.1 Motivation 53
5.2 Entropy Change in Calorimetric Processes 56
5.3 Sample Preparation 57
5.4 Magnetization Analysis 59
5.5 Specific Heat Analysis 70
5.6 Entropy Analysis 78
5.7 Summary 84

6. RELATIVE COOLING POWER IN PARAMAGNETIC MAGNETOCALORIC SYSTEMS 86

6.1 Motivation 86
6.2 Sample Preparations 87
6.3 Magnetization Analysis 87
6.4 Isothermal Entropy Change 92
6.5 Relative Cooling Power Analysis 99
6.6 Molecular Field Theory Prediction 103
    6.6.1 Theory and $Ni_{50}Mn_{36}In_{14}$ (Ni50A) Results 103
    6.6.2 $Ni_{50}Mn_{35.5}In_{14.5}$ (Ni50B) Results 106
6.7 Summary 107

7. CONCLUSION 108

REFERENCES 110

LIST OF FIGURES

FIGURE Page

1.1 The temperature dependences of the total entropy of a MCE material in two different fields (H_1 and H_2). ΔS_M and ΔT_{ad} are shown schematically. 2

1.2 Schematic temperature-dependent entropy diagram of (a) Ericsson cycles (b) Brayton cycles used for magnetic refrigeration without a first order transition. 4

1.3 The heat capacity of $Gd_5Si_2Ge_2$ as a function of temperature and magnetic field. The inset shows total entropy of $Gd_5Si_2Ge_2$ as a function of temperature and magnetic field from 250 to 350 K as determined from the heat capacity. Reprinted with permission from [5]. 5

1.4 Schematic view of (a) the $L2_1$ structure and (b) the underlying cubic sublattice [31]. 6

1.5 Temperature dependences of the magnetizations of $Ni_{50}Mn_{50-x}X_x$ (X = Ga [43], Sn [44], In [45], and Sb [46]) in a magnetic field of 5 T. The symbols in the form of triangles, squares, circles, and asterisks correspond to the alloys with Z = Ga, Sn, In, and Sb, respectively. Reprinted with permission from [47]. 8

1.6 The isothermal entropy change in $La(Fe_{13-x}Si_x)$ as a function of x for a field change of 0 to 20 kOe. Reprinted with permission from [55]. . 9

2.1 The magnetic specific heat C_v/Nk_B, calculated from a molecular field theory as discussed in the text. 17

2.2 Temperature dependence of susceptibility in antiferromagnetic materials below and above T_N, shown schematically. 18

2.3 ZFC and FC magnetization for a sample of $Ni_{48}Mn_{35}In_{17}$ which will be discussed in later chapters. The error bars are smaller than the symbols. Curie temperature (T_c) and martensitic transition (T_m) are labeled. 20

2.4 Gibbs free energy, entropy, and specific heat as a function of temperature for a first-order phase transition. 22

2.5 Gibbs free energy, entropy, and specific heat as a function of temperature for a second-order phase transition. 22

2.6 Schematic Arrott plot for a ferromagnetic material near the Curie temperature with $\gamma = 1$ and $\beta = 1/2$. 24

2.7 Schematic representation of the absolute entropy and field-induced entropy change for ideal inverse MCE materials in the vicinity of a first-order phase transition. In ideal cases, the first order transition will happen at a single temperature. 25

2.8 Schematic representation of the absolute entropy and field-induced entropy change for real inverse MCE materials in the vicinity of a first-order phase transition. In real MCE materials, the first order martensitic transition happens across a temperature region instead of at a single ideal temperature. 27

3.1 Principles of adiabatic calorimetry. I_H, Heating current; U_H, voltage across heater resistance; T_E, final temperature (after heating); T_A, initial temperature (before heating); Δt_H, heating time; ΔT, temperature increment. Reprinted with permission from [104]. 35

3.2 Schematic diagram of the Sullivan-Seidel AC calorimetry method. Reprinted with permission from [105]. 37

3.3 The overview of a Quantum Design PPMS. 38

3.4 Schematic experimental apparatus for PPMS heat-capacity measurements. 39

3.5 Principles of heat-pulse calorimetry: A square-pulse of height P_0 is applied (upper diagram), resulting in a temperature change of the sample platform the lower diagram. 39

3.6 The wire conductance vs. temperature from the calibration measurement. 41

3.7 Example of raw temperature response data with a plateau near a first-order transition and the corresponding heat capacity obtained by the analysis described in the text. 43

4.1 Fermi-Dirac distribution for $T = 0$ and for T slightly above zero. . . . 50

5.1 Schematic field-induced isothermal entropy change for non-ideal magnetocaloric effect materials is shown. ΔS saturation can be observed if the applied field is large enough to drive the martensitic transformation completely. 55

5.2 Back-scattered electron image of the $Ni_{50}Mn_{36}In_{14}$ sample after heat treatment (scale bar $20\mu m$ in the bottom of the figure). The very dark regions are empty cavities and image contrast shows grain size. 58

5.3 Temperature dependence of the magnetization for the Ni48 samples at 0.05 T and the error bars are smaller than the symbols. The data include results for both heating and cooling processes, as shown in the inset for the Ni50B sample. The low-T bifurcation corresponds to field-cooled (FC) and zero-field cooled (ZFC) as shown. Samples include Ni_{48} compositions, A=$Ni_{48}Mn_{35}In_{17}$, B=$Ni_{48}Mn_{38}In_{14}$. 60

5.4 Temperature dependence of the magnetization for the Ni50 samples at 0.05 T and the error bars are smaller than the symbols. The data include results for both heating and cooling processes, as shown in the inset for the Ni50B sample. Samples include Ni_{50} compositions, A=$Ni_{50}Mn_{36}In_{14}$, B=$Ni_{50}Mn_{35.5}In_{14.5}$. 61

5.5 Temperature dependence of the magnetization for the martensite of Ni50A sample ($Ni_{50}Mn_{36}In_{14}$) at B=0.05, 1, 3, 5, 7 T and the error bars are smaller than the symbols. The black line is the fitting from the combination of paramagnetic and antiferromagnetic model. 65

5.6 ZFC and FC magnetization curves for the Ni50A sample are shown in 0.05 T and the error bars are smaller than the symbols. 66

5.7 Arrott plots with the standard critical exponents for $Ni_{48}Mn_{35}In_{17}$ (Ni48A sample) obtained from the isothermal $M-H$ magnetization and the error bars are smaller than the symbols. $M-H$ measurements are done in 10 K, 100 K, 150 K, 160 K, 180 K, 190 K and 200 K (from right to left). 67

5.8 Temperature dependence of the magnetization for $Ni_{48}Mn_{35}In_{17}$ (Ni48A sample) at B=0.05, 1, 7 T and the error bars are smaller than the symbols. 68

5.9 Temperature dependence of the magnetization for $Ni_{48}Mn_{38}In_{14}$ (Ni48B sample) at B=0.05, 1, 2, 7 T and the error bars are smaller than the symbols. 69

5.10 The post-process method (densely plotted small symbols) vs. 2-τ model (open rectangles) for $Ni_{50}Mn_{36}In_{14}$ (Ni50A) and the error bars are smaller than the symbols. These two data sets agree very well outside of the regime where the 1st order transition happens [59]. . . 71

5.11 The post-process method (densely plotted small symbols) vs. 2-τ model (open circles) for $Ni_{50}Mn_{35.5}In_{14.5}$ (Ni50B) and the error bars are smaller than the symbols. These two data sets agree very well outside of the regime where the 1st order transition happens. 72

5.12 The post-process method (small symbols) vs. 2-τ model (open circles) for $Ni_{48}Mn_{38}In_{14}$ (Ni48B) and the error bars are smaller than the symbols. These two data agree very well outside of the regime where the 1st order transition happens. 73

5.13 The post-process method (small symbols) vs. 2-τ model (open circles) for $Ni_{48}Mn_{35}In_{17}$ (Ni48A) and and the error bars are smaller than the symbols. These two data agree very well outside of the regime where the 1st order transition happens. Note that the low-temperature end of cooling curve appears to be higher than it should be, which is believed due to the heating of the sample stage after the long heat pulse. 74

5.14 Experimental specific heat and analysis for $Ni_{50}Mn_{36}In_{14}$ (Ni50A) and the error bars are smaller than the symbols. The solid curve is the simulation according to an electronic and Debye contribution with $\gamma = 0.0124$J/mole K^2 and $\theta_D = 315$ K respectively. The low temperature measurements (< 10 K) in the inset shows the experimental data (dots) and fitting (solid line) in 0, 1, 2 Tesla. γ is found to be field independent. 76

5.15 C/T vs. T is shown for four samples. Solid curves are straight line fits. The intercepts on the y-axis represent the γ values due to conduction electrons. 77

5.16 Temperature dependence of the specific heat for the Ni-Mn-In samples without applied fields and the error bars are smaller than the symbols. The fitting curve is for Ni50A samples from a Debye model plus electronic contribution as described in text. 79

5.17 The magnetic entropy for the Ni-Mn-In samples, per mole of Mn. The solid curve represents the analysis as described in the text. The dashed curve is the antiferromagnetic curve obtained for $T_N = 540$ and $J = 2$. The horizontal line is the magnetic entropy limit for $J = 2$. 81

6.1 Temperature dependence of the magnetization for the $Ni_{50}Mn_{36}In_{14}$ (Ni50A) sample in different fields (0.05, 1, 3, 5 and 7 T as shown) and the error bars are smaller than the symbols. 88

6.2 Temperature dependence of the magnetization for the $Ni_{50}Mn_{35.5}In_{14.5}$ (Ni50B) sample in different fields (0.05, 1, and 7 T as shown) and the error bars are smaller than the symbols. 89

6.3 Temperature dependence of the magnetization comparison between $Ni_{50}Mn_{36}In_{14}$ (Ni50A) and $Ni_{50}Mn_{35.5}In_{14.5}$ (Ni50B) samples in 0.05 T and the error bars are smaller than the symbols. $Ni_{50}Mn_{35.5}In_{14.5}$ (Ni50B) has a relatively lower martensitic transition temperature. . . 90

6.4 Three selected isothermal magnetization measurements for Ni50A sample. Magnetic hysteresis was only observed between 341 and 353 K (including the 347 K trace shown) and the error bars are smaller than the symbols. Inset: Iso-field measurements for 0.05 T and 7 T, along with Curie-Weiss fittings (black lines) showing strong linearity of the results in the paramagnetic austenite phase [59]. 93

6.5 Schematic phase diagram of a typical inverse magnetocaloric effect material near the martensitic transition. Martensite starting and ending states are labelled as red lines while austenite starting and ending states are labelled as blue lines. (a) The horizontal dashed lines with arrows represents the isofield specific heat measurement. Each isofield measurement starts in the complete martensite phase and ends in the complete austenite phase. (b) The vertical dashed lines with arrows represents an isothermal magnetization measurement. The martensitic transition is not transformed completely by the available magnetic field shown. In order to do a comparison with the specific heat properly, we must go to complete martensite phase before proceeding to any higher temperature isothermal experiment. 94

6.6 Reverse (martensite to austenite) field-induced entropy changes ($S(T,H)-S(T,0)$) based on the heating-curve specific heat results (solid curve) for Ni50A ($Ni_{50}Mn_{36}In_{14}$) sample along with entropy results from the corresponding magnetic analysis (symbols). 96

6.7 The specific heat measurement for $Ni_{50}Mn_{36}In_{14}$ (Ni50A) sample under various fields by using long-pulse method and the error bars are smaller than the symbols. Data both for heating and cooling protocol are shown as arrows. 97

6.8 The specific heat measurement for $Ni_{50}Mn_{35.5}In_{14.5}$ sample under various fields by using long-pulse method and the error bars are smaller than the symbols. Data both for heating and cooling protocol are shown. 98

6.9 Reverse (martensite to austenite) field-induced entropy changes ($S(T,H)-S(T,0)$) based on the heating-curve specific heat results for Ni50B ($Ni_{50}Mn_{35.5}In_{14.5}$) sample. 100

6.10 Integrated entropy obtained from specific heat (solid curves) for Ni50A ($Ni_{50}Mn_{36}In_{14}$) along with RCP for complete transformation, compared to values obtained from the difference of isothermal magnetic measurements (symbols). 102

6.11 Relative cooling power vs. martensitic transformation temperature calculated for Ni-Mn-In compositions with paramagnetic austenite phase i.e. $T_m/Tc \geq 1$, as described in text. The circles represent the experimental RCP for $Ni_{50}Mn_{36}In_{14}$ (Ni50A) while the triangles represent those for $Ni_{50}Mn_{35.5}In_{14.5}$ (Ni50B). Inset: computed austenite average spin moment for the indicated fields. 105

6.12 Integrated entropy obtained from specific heat for $Ni_{50}Mn_{35.5}In_{14.5}$ (Ni50B). 106

LIST OF TABLES

TABLE Page

5.1 Table of the Ni-Mn-In compositions/notations and the corresponding analysis are listed. T_{mh} is defined as the maximum peak of the specific heat from the heating measurement. 63

1. MAGNETOCALORIC EFFECT

1.1 Introduction

Magnetocaloric effect (MCE) materials, first discovered in 1881 [1], undergo a temperature and/or entropy change in response to a change in the external magnetic field. Interest in the magnetocaloric effect has increased in recent decades because of the prospects of creating magnetic cooling machines using these magnetic materials as working refrigerants. Such materials are found to have potential applications as refrigerants in solid-state magnetic refrigerators near room temperature and have been employed on a regular basis in low-temperature laboratory research [2]. Magnetic refrigeration technology as a new alternative to the conventional vapor compression approach has also grown considerably, coinciding with rising international concerns about global warming due to an ever increasing energy consumption [3].

In 1976, the first design of a magnetic refrigerator operating near room temperature was developed by using Gadolinium [4]. Searching for magnetocaloric materials for room-temperature magnetic refrigeration has attracted significant attention only since Pecharsky and Gschneidner discovered a giant magnetocaloric effect in $Gd_5(Si,Ge)_4$ in 1997 [5] with a first-order transition below room temperature. A number of other magnetocaloric materials with a first-order magnetic phase transition have been intensively explored, such as MnAs-based alloys [6], $La(Fe_{1-x}Si_x)_{13}$ and their hydrides [7, 8], $MnFeP_{1-x}As_x$ and Fe_2P-based alloys [9–11], NiMn-based alloys [12–14], and $MnCoGeB_x$ [15]. In these materials, a first-order structural transition in the vicinity of the magnetic phase transition enhances the magnetocaloric effect. Moreover, the maximum isothermal entropy change is often significantly greater than that of the benchmark material, Gd, which presents a second-order magnetic phase

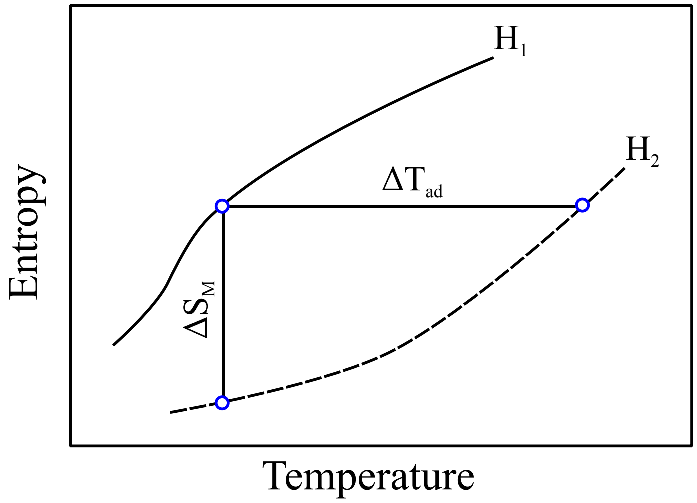

Figure 1.1: The temperature dependences of the total entropy of a MCE material in two different fields (H_1 and H_2). ΔS_M and ΔT_{ad} are shown schematically.

transition.

MCE can be characterized by the entropy change or by the temperature change of the material caused by a change of the external magnetic field. The former is the isothermal magnetic entropy change (ΔS_M) caused by scanning the magnetic field isothermally, while the latter is the adiabatic temperature change (ΔT_{ad}), caused by changing the magnetic field adiabatically [16–19].

1.2 Magnetic Refrigeration

Refrigerators of the same general type as those that we know today first came about in the early 20th century. These operate with the vapor-compression method, initially using steam engines with open drive compressors operating with dangerous and environmentally unfriendly refrigerants. In 1930, systems using CFCs (chlorofluorocarbons) for refrigeration were developed and rapidly dominated the market. Still later research revealed that the use of uncontrolled CFCs was significantly hazardous to the stratospheric ozone layer and due to the Montreal protocol, the use of these was substituted by that of HFCs (hydrochlorofluorocarbons). Although these do not damage the ozone layer, they contribute to the greenhouse effect and to the rise of the earth's average temperature and.

Magnetic refrigeration is an emerging technology. It is based on the magnetocaloric effect in solid-state refrigerants. Compared with conventional vapor compression systems, magnetic refrigeration can be an environment-friendly and efficient technology. In 1997, Ames Laboratory and Astronautics demonstrated a proof-of-principle magnetic refrigerator competitive with conventional gas compression cooling [3]. Since then, over 25 magnetic cooling units have been built and tested all over the world. Contrarily to vapor compression, since this technology resorts to materials in solid form and does not use hazardous gases, and is able to reach a maximum efficiency of about 60% [2, 20] of the Carnot limit in 5 T, such refrigerators have a bright promise for the future.

In a magnetic refrigerator, the refrigeration process occurs due to the application/removal of a magnetic field in the magnetic refrigerant. In addition, water or fluids not harmful to the environment can be used for heat exchange. In order to extract heat from a cold reservoir and release it to a heat sink, the magnetic refrigerant should work in a given thermodynamic cycle. The main thermodynamic cycles suitable to implement magnetic refrigeration are the Carnot cycle, Stirling cycle, Ericsson cycle and Brayton cycle. Among these, the Ericsson and Brayton cycles are most applicable for room temperature magnetic refrigeration and may easily achieve a large temperature span [20]. Magnetic Ericsson and Brayton thermodynamic cycles are illustrated in Fig. 1.2. The Ericsson cycle consists of two isothermal processes and two isofield processes while the Brayton cycle consists of two adiabatic processes and two isofield processes.

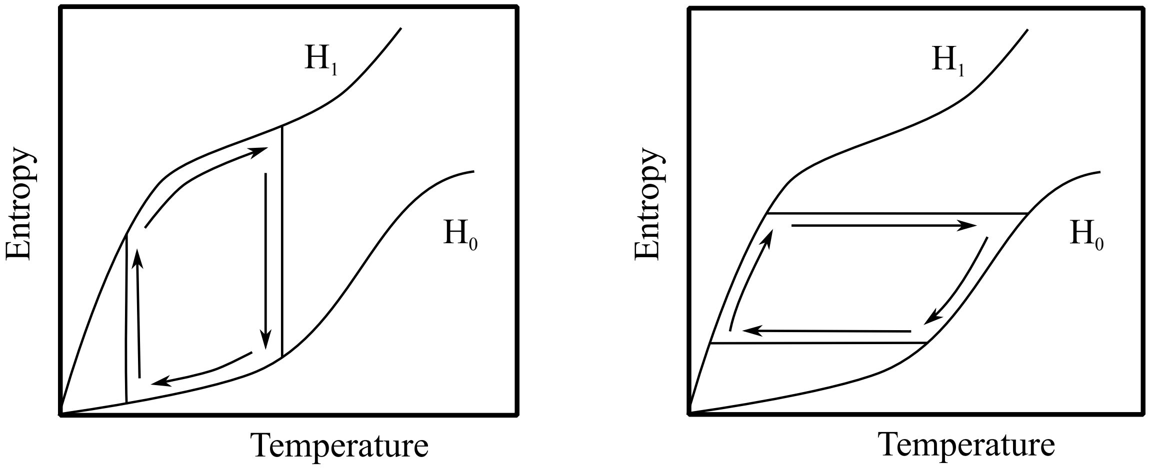

(a) Ericsson Cycles (b) Brayton Cycles

Figure 1.2: Schematic temperature-dependent entropy diagram of (a) Ericsson cycles (b) Brayton cycles used for magnetic refrigeration without a first order transition.

1.3 Magnetocaloric Materials

Recent extensive reviews of giant MCE materials systems have been presented [21–23]. In this section, I will attempt to introduce some of the giant MCE systems of most interest, and give a general idea of their characteristics.

1.3.1 Gd(Ge$_{1-x}$Si$_x$)$_4$

The Gd(Ge$_{1-x}$Si$_x$)$_4$ alloys ($0.3 \leq x \leq 0.5$), first discovered in 1997, are the first of the so-called "giant" MCE alloys [5, 24, 25] as shown in Fig. 1.3. Large magnetocaloric effects are observed in these alloys as the result of a magneto-structural phase transition between a low-temperature ferromagnetic phase and a high temperature paramagnetic or antiferromagnetic phase. At temperatures near the magneto-structural transition, the presence of a magnetic field stabilizes the high magnetization (lower temperature) phase, shifting the phase transition to higher temperatures. This results in an entropy change in the material related to the latent heat

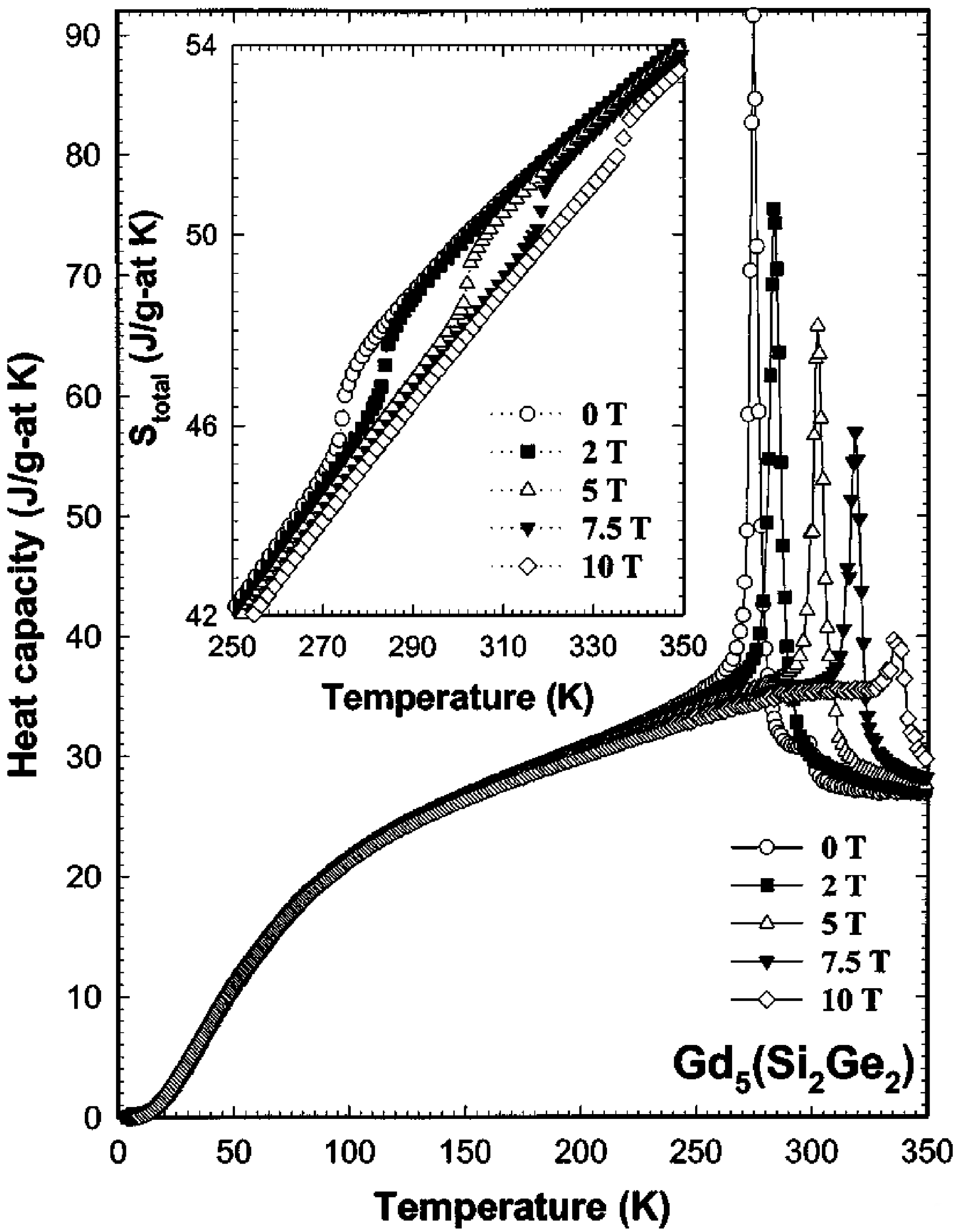

Figure 1.3: The heat capacity of $Gd_5Si_2Ge_2$ as a function of temperature and magnetic field. The inset shows total entropy of $Gd_5Si_2Ge_2$ as a function of temperature and magnetic field from 250 to 350 K as determined from the heat capacity. Reprinted with permission from [5].

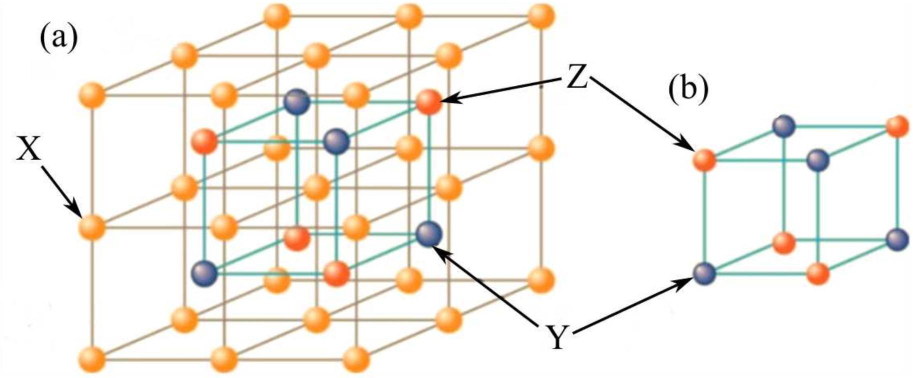

Figure 1.4: Schematic view of (a) the $L2_1$ structure and (b) the underlying cubic sublattice [31].

of the phase transition [26]. Although the magnetic entropy changes measured in $Gd(Ge_{1-x}Si_x)_4$ alloys remain among the largest among MCE materials (up to 45 J /kg K at $\mu_0 H = 5T$) [27], the material suffers from significant hysteresis [28] and kinetic [29, 30] limitations associated with the first-order phase transition. This will also influence the optimal operation-frequency and the efficiency of a magnetic refrigerator.

1.3.2 Ni-Mn-Z Heusler Alloys

Among new magnetocaloric materials, an interesting class is Heusler materials. It is these materials on which this dissertation focuses. These are ordered intermetallics with the generic formula X_2YZ in which the three components occupy the crystallographic non-equivalent positions of an $L2_1$ structure. In this formula, X and Y are 3d elements and Z is a group IIIA-VA element with positions as shown in Fig. 1.4. These alloys often show magnetism, which is due to the X and/or Y elements. Many Heusler alloys undergoing magneto-structural transitions have been reported to have a large MCE around the transition temperature [5, 7]. These magnetic and metamagnetic shape-memory alloys have attracted considerable attention as candidates for novel rare-earth free magnetic refrigerants [12, 14, 23, 32–35]. A common characteristic feature of many Heusler alloys is that their magnetoelastic interaction substantially affects the phase transformations and other properties.

In the important Ni-Mn-based family (Ni-Mn-Z, Z = Ga, In, Sn, Sb), the magnetic moment is confined primarily to the Mn atoms [36] and a giant MCE due to the first order martensitic transition has been reported [12, 37–39]. In inverse MCE materials, an increase in applied field causes a decrease in the temperature of the material while the opposite temperature response is typically observed in conventional MCE materials. The giant conventional MCE was first reported in Ni-Mn-Ga [40, 41] while inverse MCEs have been observed in the Ni-Mn-X (X=Sn, Sb, In) Heusler alloy system [12, 42]. Some of the representative experimental magnetization curves for Ni-Mn Heusler alloys from the literature are shown in Fig. 1.5.

1.3.3 MnAs Based Compounds

MnAs exists in two distinct crystallographic structures [48], similar to $Gd_5Ge_2Si_2$. At low and high temperatures the hexagonal NiAs structure is found whereas for a narrow temperature range of 307-393 K the orthorhombic MnP structure exists. The high temperature transition in the paramagnetic region is second order. The low temperature transition is a combined the first-order structural and ferro-paramagnetic transition with large thermal hysteresis. The change in volume at this transition amounts to 2.2% [49]. Very large magnetic entropy changes are observed at this transition, between 307 K and 317 K [6, 50]. Substitution of Sb for As leads to a lowering of T_c and the reduction of hysteresis [51, 52]. The materials costs of MnAs are quite low. However, processing of As containing alloys is complicated due to the biological activity of As. In the MnAs alloy, As is covalently bound to the Mn and would not be easily released into the environment. However, this should be ex-

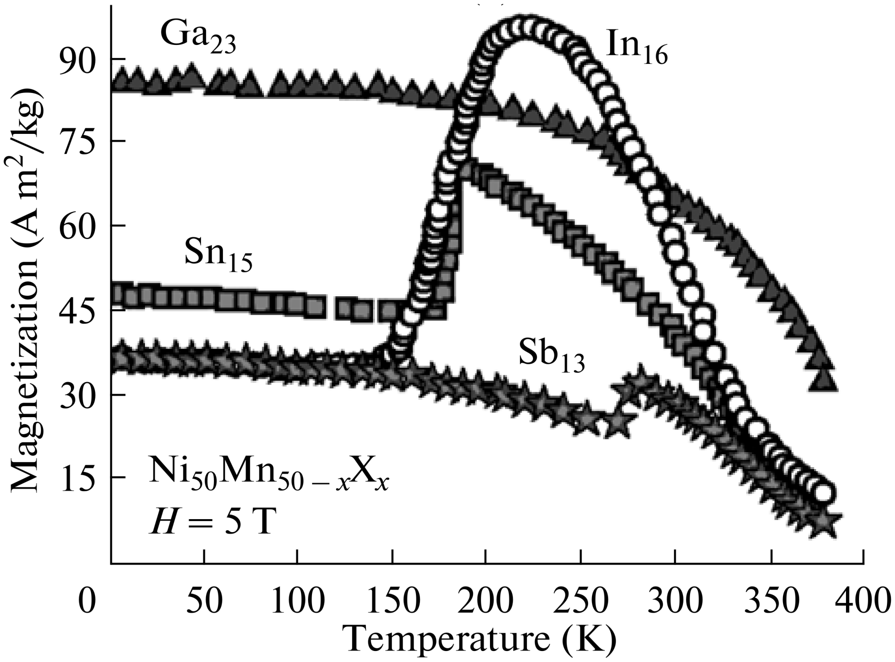

Figure 1.5: Temperature dependences of the magnetizations of $\mathrm{Ni}_{50}\mathrm{Mn}_{50-x}\mathrm{X}_x$ (X = Ga [43], Sn [44], In [45], and Sb [46]) in a magnetic field of 5 T. The symbols in the form of triangles, squares, circles, and asterisks correspond to the alloys with Z = Ga, Sn, In, and Sb, respectively. Reprinted with permission from [47].

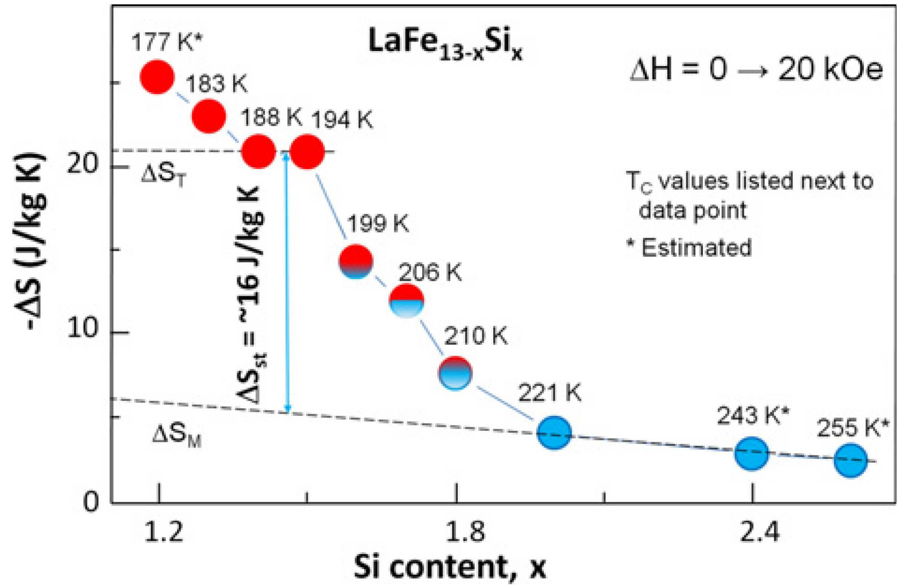

Figure 1.6: The isothermal entropy change in La(Fe$_{13-x}$Si$_x$) as a function of x for a field change of 0 to 20 kOe. Reprinted with permission from [55].

perimentally verified, especially because in a non-stoichiometric alloy second phases frequently form that may be less stable.

1.3.4 La(Fe,Si)$_{13}$ and Related Compounds

Another interesting type of material is rare-earth-transition-metal compounds crystallizing in the cubic NaZn$_{13}$ type of structure. The giant MCE in the itinerant electron metamagnet La(Fe$_{11.4}$Si$_{1.6}$) phase was first reported by Hu *et al* [7]. It exhibits a large volume change of 1.5% and a substantial hysteresis as a function of field or temperature [53]. Further investigations revealed that the entropy is enhanced with lower Si content (down to La(Fe$_{11.8}$Si$_{1.2}$)) but the transition temperature decrease from 195 K to 180 K. On the other hand, increasing the Si content destroys the first-order transition and raises T_C to 220 K at the compositions La(Fe$_{11.0}$Si$_{2.0}$), where the magnetic transition is purely second order [22, 54] as shown in Fig. 1.6.

From the materials cost point of view the La(Fe,Si)$_{13}$ type of alloys appear to be very attractive. La is the cheapest of the rare-earth series, and both Fe and Si are available in large amounts. On the other hand, the transformation including such a volume change is performed very frequently the material will definitely become very brittle and probably break into smaller grains. This can have a distinct influence on the corrosion resistance of the material and thus on the lifetime of a refrigerator. The suitability of this material definitely needs to be tested further.

1.4 Experimental Field-induced Isothermal Entropy

Generally speaking, the entropy of a solid is made up of contributions from the magnetic ions, crystalline lattice, and conduction electrons. For the sake of simplicity, we consider that the total entropy of a solid can be written as a sum of these three contributions,

$$S_{tot}(T,B) = S_{mag}(T,B) + S_{lat}(T) + S_{el}(T) \tag{1.1}$$

where S_{mag} is the magnetic contribution including the variation of the magnetic field, S_{lat} is the contribution from the crystalline lattice, and S_{el} is the contribution from the conduction electrons. We suppose here that only the magnetic part of the entropy depends on the magnetic field.

From the experimental point of view, the entropy curve can be determined from heat capacity measurements using the thermodynamic relation $\Delta S = \int C(T)/T dT$, where $C(T)$ is the heat capacity. The isothermal entropy change upon magnetic-field variation can be obtained from the heat capacity vs temperature curves as [56]

$$\Delta S(T, B_0 \rightarrow B_1) = \int_0^T \frac{C_p(T', B_1) - C_p(T', B_0)}{T'} dT'. \tag{1.2}$$

The field-induced entropy change can also be determined indirectly from the measurement of M versus H with sufficiently small temperature increments. The field-induced entropy change is then obtained as [57, 58]

$$\Delta S(T, B_0 \to B_1) = \lim_{\Delta T \to 0} \frac{1}{\Delta T} \left[\int_{B_0}^{B_1} M(T + \Delta T, B) dB - \int_{B_0}^{B_1} M(T, B) dB \right]. \quad (1.3)$$

In order to characterize MCE materials, isothermal magnetic measurements and field dependent specific heat measurements are crucial. Understanding the hysteresis in the phase diagram is important when performing experiments and data analysis because non-equilibrium thermodynamic states are involved. In our study [59], an improved specific heat measurement technique has been applied to measure across first order transitions successfully. Also, additional temperature cycles in the $M - H$ measurements were performed to ensure a consistent forward martensitic transformation for each measurement [59]. In a later chapter we will describe several traditional experimental methods and a method for tracing the specific heat across the first order phase transition by this analysis. In addition, in the experimental section we will describe how to overcome the phase coexistence issue in magnetization measurements in order to properly compare results from calorimetric measurements.

1.5 Relative Cooling Power

Another relevant quantity for evaluating the performance of MCE materials is the amount of transferred heat between cold and hot reservoirs in an Ericsson magnetic refrigeration cycle [60–62] as shown in Fig. 1.2. The relative Cooling Power (RCP) is a measure of a MCE material's ability to work as a heat/cool engine [21] and it is commonly used to determine the performance of the MCE material.

Its mathematical formula can be expressed as,

$$\mathrm{RCP}(H) = \int_{T_{cold}}^{T_{hot}} \Delta S(T, 0 \to H) dT, \quad (1.4)$$

where T_{cold} and T_{hot} are the temperatures of the two reservoirs. Therefore we can obtain RCP by calculating the area under the ΔS curves. Similar to the field-induced isothermal entropy described in the previous section, RCP can be obtained by using two distinct experimental methods. Here, I expand Eq. 1.4 by using Eq. 1.3 [63], giving

$$\mathrm{RCP}(H) = \int_{T_{cold}}^{T_{hot}} \Delta S(T, 0 \rightarrow H) dT = \int_0^H M(T_{hot}, H') dH' - \int_0^H M(T_{cold}, H') dH' \tag{1.5}$$

which indicates that RCP can be determined from isothermal magnetic measurements at only two temperatures without knowing the details of the magnetic entropy at points between. Thus, even if a broad temperature transition happens experimentally, a large number of magnetic isotherms is not required. On the other hand, since the entropy change data obtained from specific heat are usually much denser, we can also calculate the entropy integral directly from the data. The comparison of the results provide additional useful information for us to better understand MCE materials.

2. MAGNETIC ORDER AND TRANSITION IN MATERIALS

The macroscopic magnetic properties of materials are a consequence of magnetic moments associated with individual electrons. It is known from experiment that every material which is put in a magnetic field acquires a magnetic moment. The dipole moment per unit volume defined as the magnetization will be denoted here by the M. In many materials, M is proportional to the applied field H. The relation is then written as

$$M = \chi H \tag{2.1}$$

where χ is the magnetic susceptibility of the material. Generally, χ values are used to categorize the material. In the following section, we will introduce paramagnetism, antiferromagnetism, and ferromagnetism [64, 65].

2.1 Paramagnetism

For some solid materials, each atom possesses a permanent dipole moment by virtue of incomplete cancellation of electron spin and/or orbital magnetic moments. In the absence of an external magnetic field or interactions between atoms, the orientations of these atomic magnetic moments are random, such that a piece of material possesses no net macroscopic magnetization. These atomic dipoles are free to rotate, and paramagnetism results when they preferentially align with an external field. The magnetization response to magnetic fields and temperatures can be expressed as [66]

$$M = NgJ\mu_B B_J(x) \tag{2.2a}$$

$$x = \frac{gJ\mu_B H}{k_B T} \tag{2.2b}$$

$$B_J(x) = \frac{2J+1}{2J}\coth\left(\frac{2J+1}{2J}x\right) - \frac{1}{2J}\coth\left(\frac{1}{2J}x\right), \tag{2.2c}$$

where μ_B is the Bohr magneton, N is the total number of magnetic ions in the specimen and $B_J(x)$ is a Brillouin function.

2.2 Ferromagnetism

A small number of crystalline substances exhibits strong magnetic effects called ferromagnetism [67]. Some examples of ferromagnetic substances are iron, cobalt, nickel, gadolinium, and dysprosium. These substances contain permanent atomic magnetic moments that tend to align parallel to each other even in a weak external magnetic field. Once the moments are aligned, the substance remains magnetized after the external field is removed at least within each domain. This permanent alignment is due to exchange interactions between neighboring spin moments. In the Heisenberg model, the Hamiltonian for atoms with the spin moments $\vec{s_i}$ (or $\vec{s_j}$) in the magnetic field H can be written in the form

$$\mathcal{H} = -\sum_{i,j} J_{i,j}\vec{s_i}\cdot\vec{s_j} - \mu_B H\sum_i \vec{s_i} \tag{2.3}$$

with

$$J_{i,j} = \begin{cases} J & \text{if } i,\ j \text{ are neighbors} \\ 0 & \text{otherwise.} \end{cases} \tag{2.4}$$

When the temperature of a ferromagnetic substance reaches or exceeds a critical temperature T_c, called the Curie temperature, the substance loses its residual magnetization. Below the Curie temperature, the magnetic moments are aligned and the substance is ferromagnetic. Above the Curie temperature, the thermal agitation is great enough to cause a random orientation of the moments, and the substance becomes paramagnetic. The magnetic response due to small magnetic fields in the paramagnetic regime can be expressed as [68]

$$M = \frac{\mu_0 N g^2 \mu_B^2 J(J+1)}{3k_B} \frac{H}{T - T_c}. \tag{2.5}$$

2.3 Antiferromagnetism

In materials that exhibit antiferromagnetism, the magnetic moments of atoms align in opposite directions on different sublattices. Generally speaking, antiferromagnetic order exists at sufficiently low temperatures, vanishing at and above a certain temperature, the Néel temperature T_N. Above T_N, the material is paramagnetic.

In the molecular field theory of antiferomagnetism, the system is composed of two sublattices with an opposite and identical magnitude of magnetic moments The induced magnetization M of the sublattice in the presence of an effective field H' caused by its immediate neighbors is paramagnetic. Hence, M is expressed as

$$M = NSg\mu_B B_S \left(\frac{g\mu_B S H'}{k_B T} \right), \tag{2.6}$$

where B_S is the Brillouin function. Note that each atom is neighbor to atoms possessing fields with opposite directions in an ideal antiferromagnetic material. Thus, apart from a trivial additive constant, we may take [69, 70]

$$H' = -2|J| \cdot \sum_j S_j / g\mu_B = -2z|J| \cdot \bar{S} / g\mu_B, \tag{2.7}$$

where z is the number of neighbors possessed by a given atom and $\bar{S}$ is the magnetization of a sublattice. The variation of $\bar{S}$ with temperature can be obtained by substituting the molecular field H' in place of H in Eq. 2.6. This gives the implicit equation

$$\bar{S} = SB_S\left(\frac{2|J|zS\bar{S}}{k_BT}\right) \tag{2.8}$$

The solution $\bar{S}$ of this equation is S as $T \rightarrow 0$ but falls catastrophically to zero as T approaches a critical temperature T_N, given by

$$T_N = \frac{2}{3}|J|zk_B^{-1}S(S+1). \tag{2.9}$$

The magnetic internal energy and the magnetic or excess specific heat can be obtained as

$$C_v = \frac{dE}{dT} = \frac{d}{dT}\left(-N|J|z\bar{S}^2\right) = -2N|J|z\bar{S}\frac{d\bar{S}}{dT} = -3Nk_B\frac{T_N}{S(S+1)}\bar{S}\frac{d\bar{S}}{dT} \tag{2.10}$$

and the numerical results for different S are illustrated in Fig. 2.1. Note that the specific heat contributions due to ferromagnetism and antiferromagnetism are actually identical based on the molecular field theory although the magnetization behaviors are apparently different.

Van Vleck applied Eq. 2.6 to each sub-lattice separately, replacing H by the appropriate effective field which is the vector sum of H and the molecular field due to the atoms on the other sub-lattice. He obtained the following results for the susceptibility in the limit of low fields [71]. Below T_N, χ depends on whether the applied field is parallel to the direction of spontaneous antiferromagnetism ($\chi_{\parallel}$) or whether it is perpendicular to this axis ($\chi_{\perp}$), resulting in

$$\chi_{\parallel} = \frac{Ng^2\mu_B^2J^2B_S(y)}{k_B[T+3T_NS(S+1)^{-1}]B_S(y)} \text{ where } y = 2z|J|S\bar{S}/k_BT \tag{2.11a}$$

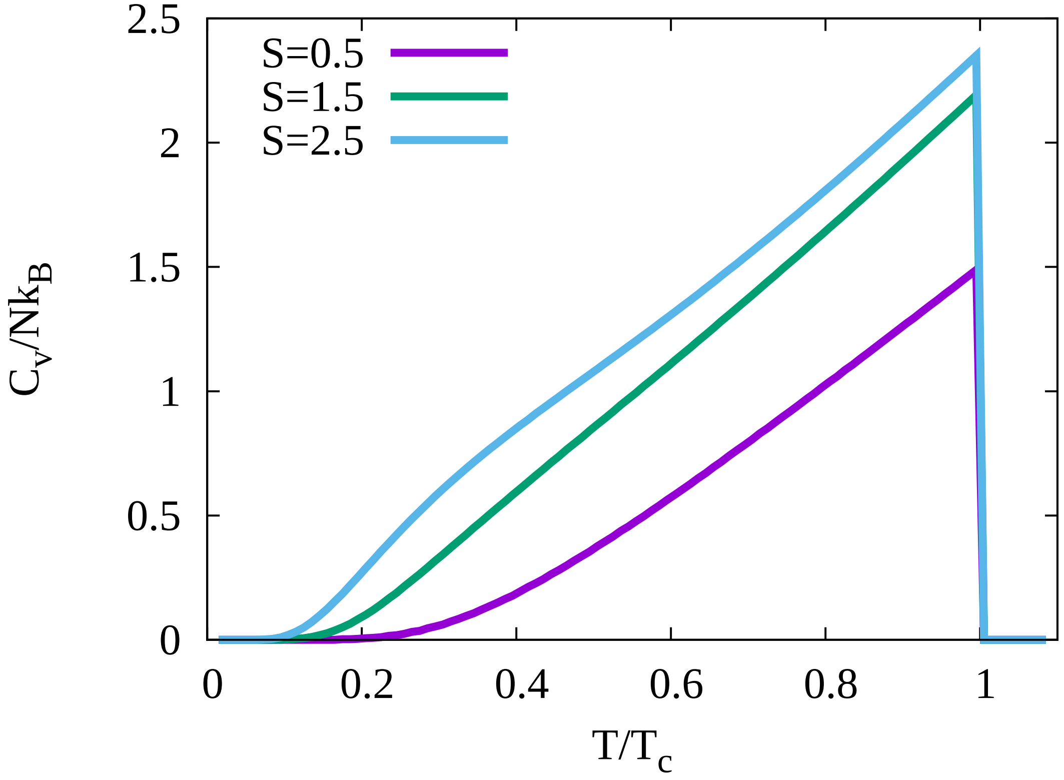

Figure 2.1: The magnetic specific heat C_v/Nk_B, calculated from a molecular field theory as discussed in the text.

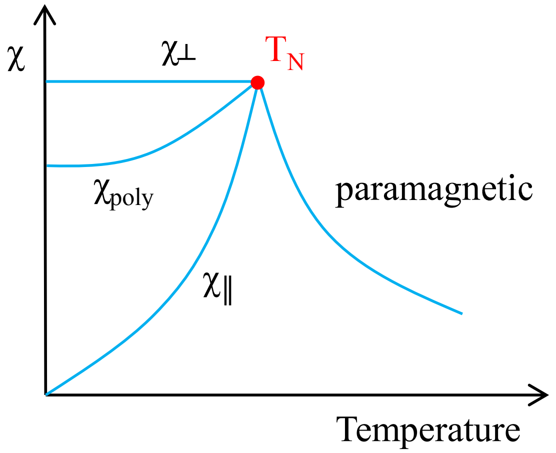

Figure 2.2: Temperature dependence of susceptibility in antiferromagnetic materials below and above T_N, shown schematically.

$$\chi_{\perp} = \frac{Ng^2\mu_B^2 S(S+1)}{6k_B T_N} \tag{2.11b}$$

and the results are illustrated as Fig. 2.2. However, many antiferromagnets are studied experimentally as powders or polycrystals, and these we must expect to contain a random distribution of antiferromagnetic axes and therefore to be isotropic, so that, averaging over all directions of the axis of spontaneous antiferromagnetism we find that the powder susceptibility is

$$\chi_p(T) = \frac{2}{3}\chi_{\perp}(T) + \frac{1}{3}\chi_{\parallel}(T) \tag{2.12}$$

and $\chi(0)$ should have the average value of $\frac{2}{3}\chi_{\perp}$. Above T_N, there is no spontaneous antiferromagnetism and the crystal is isotropic:

$$\chi = \frac{Ng^2\mu_B^2 J(J+1)}{3k_B(T+T_N)}. \tag{2.13}$$

Ideal antiferromagnetism is composed of the two sublattices with identical magnitude of magnetic moments but opposite direction. The system is considered to be "ferrimagnetic" when the two sublattices possesses unequal magnitude of magnetic moments.

2.4 Field-cooled and Zero-field-cooled Measurements

Certain magnetic systems undergoing transitions to ordered ferromagnetic [72–77], antiferromagnetic [78] and ferrimagnetic [79] states are reported to show irreversibility, indicated by the difference between their field-cooled (FC) and zero-field-cooled (ZFC) susceptibilities. ZFC magnetization is achieved by applying a small field and cooling to a low temperature and then the sample is then warmed in a constant field with the magnetization being measured as a function of temperature. FC magnetization is obtained starting at a high temperature and in an applied field and then taking measurements as the temperature is lowered gradually in this constant field.

The irreversible FC vs. ZFC magnetic behavior is also one of the characteristic features of a spin glass. T_g is defined as the temperature at which the irreversibility disappears as the sample temperature is increased. However, whether this corresponds to glass transition need be determined by additional measurements such as frequency dependent susceptibility. The irreversibility appears in many of the materials in the thesis. In Fig. 2.3, I demonstrated FC and ZFC magnetization results from one of our material ($Ni_{48}Mn_{35}In_{17}$). Besides hysteretic martensitic transformation (T_m), Curie temperature (T_c) are also observed in this material. Additional measurements are typically used to definitively distinguish spin glass effects from other ordered magnetic states; not discussed here.

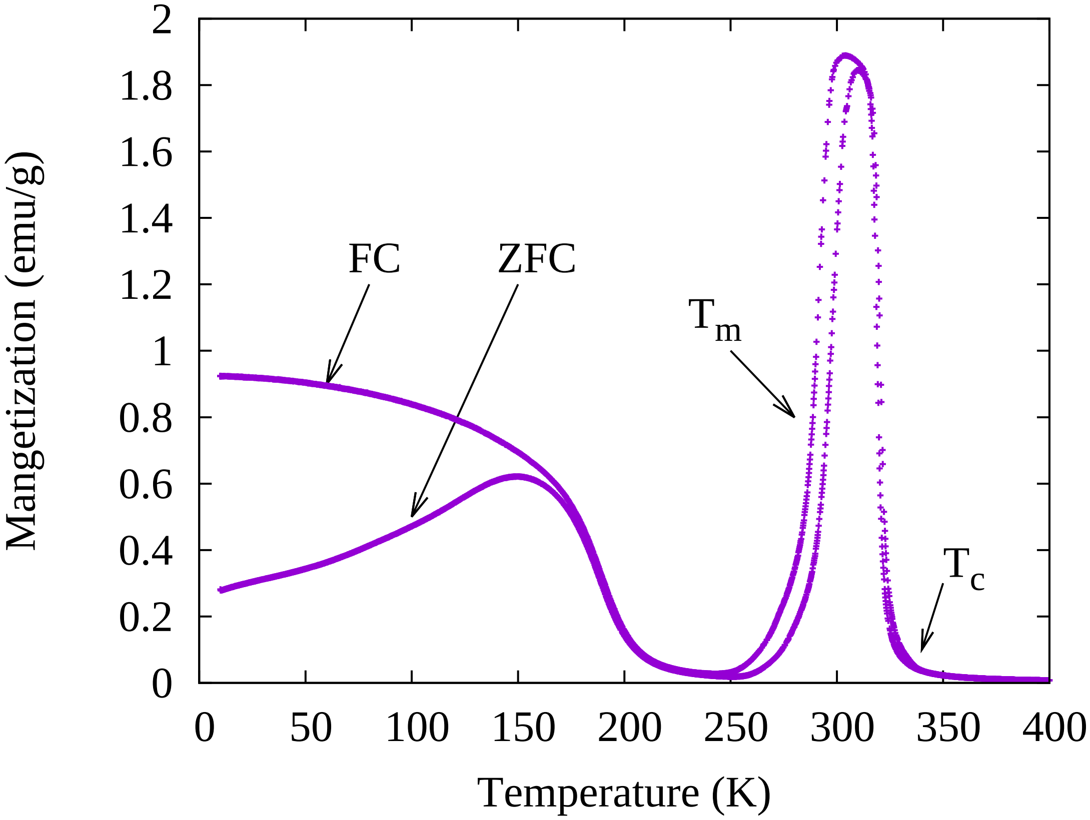

Figure 2.3: ZFC and FC magnetization for a sample of $Ni_{48}Mn_{35}In_{17}$ which will be discussed in later chapters. The error bars are smaller than the symbols. Curie temperature (T_c) and martensitic transition (T_m) are labeled.

2.5 Thermodynamics of Phase Transitions

Changes of phase are called phase transitions, and phase transitions are ubiquitous in nature. In the modern classification scheme, phase transitions are divided into two broad categories [80, 81]. Phase transitions which are connected with an entropy discontinuity are called discontinuous or phase transitions of first order. On the other hand, phase transitions where the entropy is continuous are called continuous or of second or higher order.

For a first-order phase transition, the first derivative of the Gibbs free energy with respect to the temperature is discontinuous, as is the entropy:

$$S = -\left(\frac{\partial G}{\partial T}\right)_P . \tag{2.14}$$

This discontinuity produces a divergence in the higher derivatives such as the specific heat C_p (see Fig. 2.4)

$$C_p = T\left(\frac{\partial S}{\partial T}\right)_P = -T\left(\frac{\partial^2 G}{\partial^2 T}\right)_P . \tag{2.15}$$

For a phase transition of second order, the first derivative of the free enthalpy is continuous. However, the second derivatives, such as specific heat, are discontinuous or divergent. Fig. 2.5 shows how a kink in the entropy due to a second order transition causes the discontinuity of the specific heat around the transition.

2.6 Arrott Plot

One of the standard experimental methods for establishing the presence of ferromagnetic order is the Arrot plot [82, 83] in which the square of the magnetization M

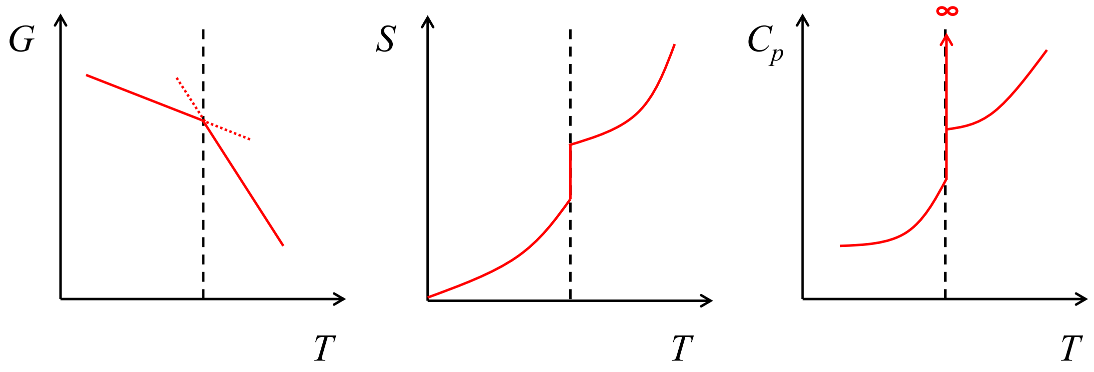

Figure 2.4: Gibbs free energy, entropy, and specific heat as a function of temperature for a first-order phase transition.

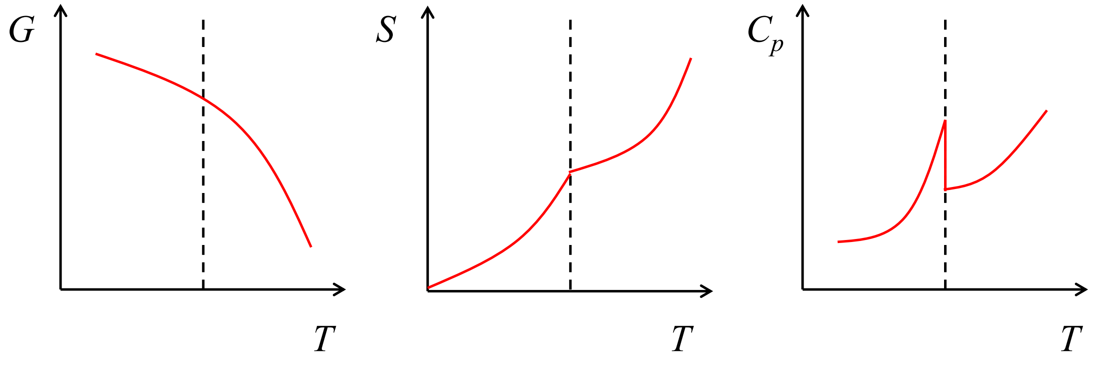

Figure 2.5: Gibbs free energy, entropy, and specific heat as a function of temperature for a second-order phase transition.

in a field H is plotted as a function of H/M for a fixed temperature T. The Arrott plot technique is based on the Weiss-Brillouin treatment of molecular field theory. Eq. 2.17 gives the proposed equation for magnetization as a function of both applied field and temperature:

$$M = M_0 \tanh\left(\frac{\mu(H+\lambda M)}{k_B T}\right) \tag{2.16}$$

where M_0 is the spontaneous magnetization at absolute zero, μ is the magnetic moment per atom and λ is the molecular field constant. This equation can be rewritten by assuming M/M_0 to be very small at the Curie temperature and we get

$$\frac{\mu H}{k_B T} + \lambda\frac{\mu M}{k_B T} = \tanh^{-1}\left(\frac{M}{M_0}\right) = \frac{M}{M_0} + \frac{1}{3}\left(\frac{M}{M_0}\right)^3 + \frac{1}{5}\left(\frac{M}{M_0}\right)^5 + \cdots . \tag{2.17}$$

Ignoring higher order terms in M/M_0 and differentiating the equation with respective M, we get

$$\frac{1}{\chi} = \left(\frac{k_B T}{\mu M_0}\right) - \lambda. \tag{2.18}$$

At the Curie temperature, $1/\chi = 0$ and the Curie temperature can be expressed as

$$T_c = \left(\frac{\mu\lambda}{k_B}\right) M_0. \tag{2.19}$$

Thereby, Eq. 2.17 can be rewritten in term of T_c

$$\frac{\mu H}{k_B T} = \epsilon\frac{M}{M_0} + \frac{1}{3}\left(\frac{M}{M_0}\right)^3 + \frac{1}{5}\left(\frac{M}{M_0}\right)^5 + \cdots , \tag{2.20}$$

where $\epsilon = \frac{T-T_c}{T}$. Considering terms only up to third order and introducing the critical exponents γ and β into Eq. 2.20 to accommodate for deviations from the mean field

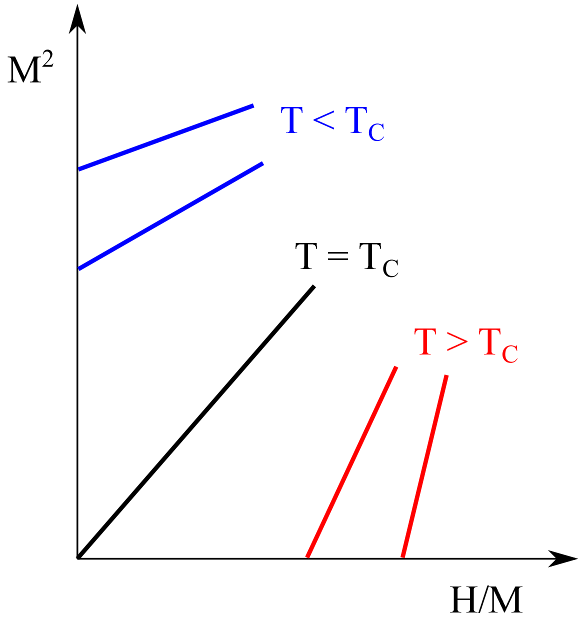

Figure 2.6: Schematic Arrott plot for a ferromagnetic material near the Curie temperature with $\gamma = 1$ and $\beta = 1/2$.

approximation, we get [84]

$$\left(\frac{H}{M}\right)^{1/\gamma} = \frac{T - T_c}{T_1} + \left(\frac{M}{M_1}\right)^{1/\beta}, \tag{2.21}$$

where M_1 and T_1 are constants. Eq. 2.21 is used to identify the best values of the critical exponents γ and β under which isothermal $M - H$ curves are straight and parallel lines. When this is done, the isotherm which passes through the origin of the plot of $(H/M)^{1/\gamma}$ vs. $M^{1/\beta}$ represents the Curie temperature. A schematic Arrott plot for a ferromagnetic material near the Curie temperature with $\gamma = 1$ and $\beta = 1/2$ is shown in Fig. 2.6

2.7 First Order Magnetic Transitions

One of the main characteristics of giant magnetocaloric materials is the coexistence of a first order magnetic phase transition coupled with variations of the lattice

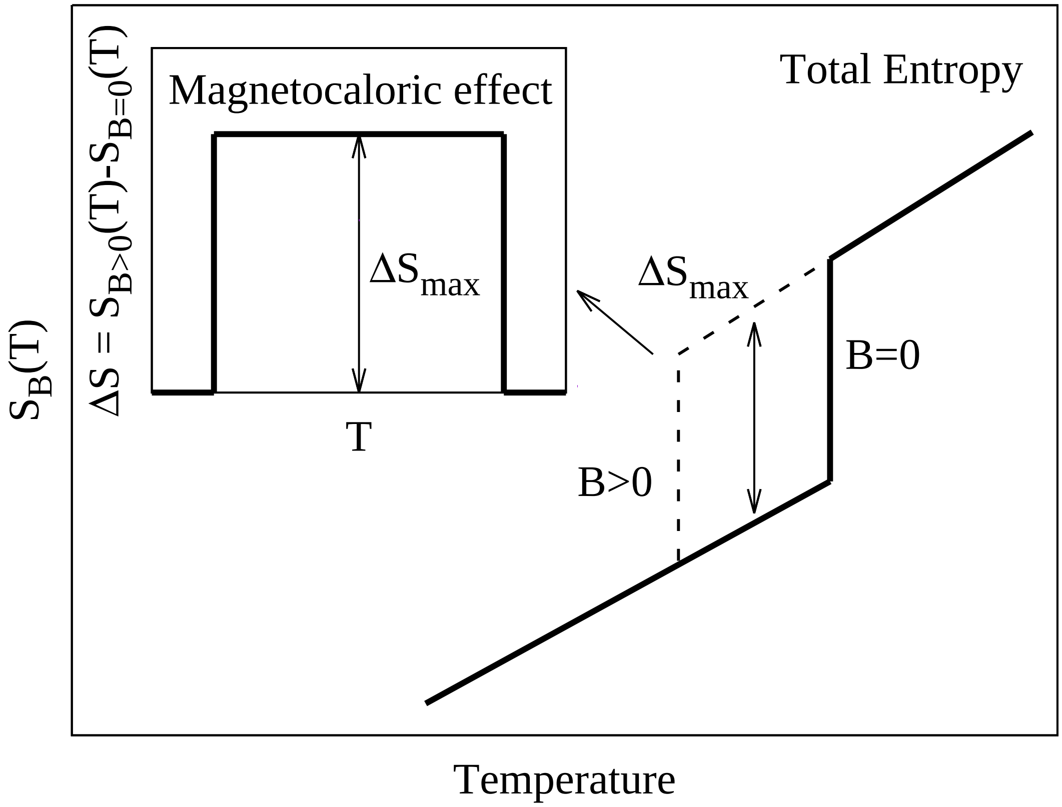

Figure 2.7: Schematic representation of the absolute entropy and field-induced entropy change for ideal inverse MCE materials in the vicinity of a first-order phase transition. In ideal cases, the first order transition will happen at a single temperature.

parameters. This first order solid-solid phase transition, which has a diffusionless nature consisting of a homogeneous lattice deformation leading to a new crystal structure, is also known as a martensitic transition. An ideal first order transition should happen at a single temperature as shown in Fig. 2.7, and the corresponding isothermal entropy due to external fields should always be a step function. However, in real MCE materials, the first order transition happens over a finite range of temperatures. In the temperature range where the first order transition happens, the portion of one phase increases while the other decreases as the temperature in the materials increases or decreases. A schematic representation of the entropy behavior and field-induced entropy change for inverse MCE materials in the vicinity of a first-order phase transition is shown in Fig. 2.8. Across the temperature region where the first order transition happens, the entropy changes abruptly and the first derivative of the Gibbs free energy is discontinuous. As distinct from a second order transition, a latent heat is observed experimentally in a first order transition. For MCE materials, the variation of the lattice parameter drives a variation in the lattice-elastic energy which, in the equilibrium condition, must be counterbalanced by the exchange energy among the magnetic ions so it is expected to find a strong dependence of the exchange parameter with the volume in these materials [85]. Two of the most common theoretical models for this behavior based on Landau theory will be described in the following sections.

2.7.1 Clausius-Clapeyron Relation

The Clausius-Clapeyron relation is a way of characterizing a first order phase transition between a two-phase and one-component system in equilibrium [86]. For a first-order magnetic phase transitions the magnetic Clausius-Clapeyron equation is valid:

$$\mu_0 \frac{dH}{dT} = -\frac{\Delta S}{\Delta M} \tag{2.22}$$

where $\Delta S = S_{M_2} - S_{M_1}$ and $\Delta M = M_2 - M_1$ are the entropy differences and the magnetization difference between states 2 and 1 at the transition temperature (T) and the transition field (H). Using this equation one can calculate the entropy change (and consequently the MCE) at the transition on the basis of magnetization data and the magnetic phase diagram $H - T$.

In the case of a magnetostructural phase transition, the Clausius-Clapeyron re-

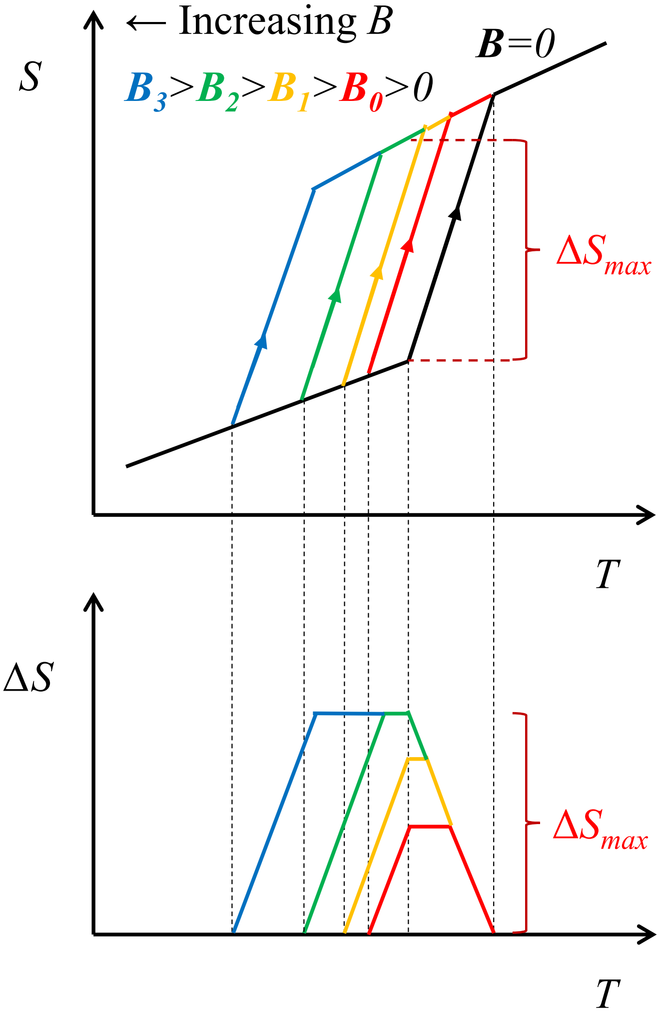

Figure 2.8: Schematic representation of the absolute entropy and field-induced entropy change for real inverse MCE materials in the vicinity of a first-order phase transition. In real MCE materials, the first order martensitic transition happens across a temperature region instead of at a single ideal temperature.

lation is modified so that the dissipated energy is taken into account: [36, 87]

$$\mu_0 \frac{dH}{dT} = -\frac{\Delta S}{\Delta M} + \frac{1}{\Delta M} \frac{dE_{diss}}{dT}, \tag{2.23}$$

where E_{diss} is dissipated energy. Notice that E_{diss} is usually weakly dependent on temperature, and thus the last term is claimed to be negligible in Heusler alloys which shows that the Clausius-Clapeyron equation is still a good approximation [36, 88].

2.7.2 Model of Exchange-inversion Magnetization

The exchange-inversion theory, proposed by Kittel [89] considers the dependence of the exchange interaction on the interatomic distance and describes quite well the antiferromagnetic to ferromagnetic transitions in Mn_2Sb and in FeRh [90–95]. According to this model, we assume that the interlattice exchange energy of a specimen of volume V can be written as

$$-\rho(a - a_c)V\mathbf{M_A} \cdot \mathbf{M_B} \tag{2.24}$$

where a is the relevant lattice parameter and a_c, is the value at which the interlattice exchange interaction changes sign; ρ denotes $\partial\lambda/\partial a$, where λ is the molecular field constant connecting the sublattice magnetizations $\mathbf{M_A}$ and $\mathbf{M_B}$. We have no a priori knowledge of the sign of ρ, which may be positive or negative, according to the substance. If we may neglect the intrinsic dependence of the sublattice magnetization on the parameter a, the parts of the Gibbs free energy at zero pressure including the exchange-interaction energy and the elastic energy of a volume V can be written to the lowest relevant order as,

$$G = \frac{1}{2}RV(a - a_T)^2 - \rho(a - a_c)V\mathbf{M_A} \cdot \mathbf{M_B}, \tag{2.25}$$

where R represents the appropriate elastic stiffness constant divided by a^2 and a_T stands for the equilibrium value of a at temperature T for the orientation $\mathbf{M_A} \perp \mathbf{M_B}$. Obviously, the free energy of the system is dependent on strain. The equilibrium value of a is given by

$$\left(\frac{\partial G}{\partial a} \right)_T = RV(a - a_T) - \rho V \mathbf{M_A} \cdot \mathbf{M_B} = 0. \tag{2.26}$$

Therefore, one obtains

$$a = a_T + \frac{\rho}{R} \mathbf{M_A} \cdot \mathbf{M_B}. \tag{2.27}$$

A combination of eqs. 2.25 and 2.27 yields

$$\frac{G}{V} = -\frac{\rho^2}{2R} (\mathbf{M_A} \cdot \mathbf{M_B})^2 - \rho(a_T - a_c)(\mathbf{M_A} \cdot \mathbf{M_B}). \tag{2.28}$$

Given $M_A = M_B = M_0$ and a transition driving force $2\mu_0 H_c M_0$, the energies of the two phases must be equal at the transition so that

$$\left(\frac{G}{V} \right)_{AF} + 2\mu_0 H_c M_0 = \left(\frac{G}{V} \right)_{FM}. \tag{2.29}$$

Substitution of Eq. 2.28 and 2.29 gives

$$\mu_0 H_c = -\rho M_0 (a_T - a_c). \tag{2.30}$$

The critical distance is independent of temperature and, for an isotropic material, $(a_T - a_c)/a_c$ is proportional to the thermal expansion during the transition, $\Delta L/L_0$. Therefore, it can be expected that $\mu_0 H_c/M_0$ is proportional to $\Delta L/L_0$ [96]. Taking into account the temperature dependence of the ρ coefficient, it is possible to describe the magnetocaloric and elastocaloric effects within the framework of the same model

[97].

2.7.3 The Bean-Rodbell Model

Bean and Rodbell [98, 99] have proposed a phenomenological model that describes a first-order magneto-structural phase transition. This model has been used to explain the first-order magnetic phase transition observed for MnAs [100] and $\mathrm{MnFeP}_{1-x}\mathrm{As}_x$ [101] quantitatively.

This model correlates strong magnetoelastic effects with the occurrence of a first-order phase transition. The central assumption in this model is that the exchange interaction (or Curie temperature) is strongly dependent on the interatomic spacing. In this model, the dependence of Curie temperature on the volume is represented by

$$T_c = T_0 \left[1 + \beta \frac{V - V_0}{V_0} \right], \tag{2.31}$$

where T_c is the Curie temperature, whereas T_0 would be the Curie temperature if the lattice were not compressible, and V_0 would be the volume in the absence of exchange interaction. The coefficient β can either be positive or negative.

The critical behavior of the magnetic system is analyzed on the basis of the Gibbs free energy consisting of the following contributions

$$G = G_{exchange} + G_{Zeeman} + G_{elastic} + G_{entropy} + G_{press} \tag{2.32}$$

where $G_{exchange}$, G_{Zeeman}, $G_{elastic}$, $G_{entropy}$ and G_{press} represent the exchange interaction, the Zeeman energy, the elastic energy, the entropy term, and the pressure terms, respectively. This formula can be expressed within the molecular-field approximation, for materials with arbitrary spin j as

$$G = -\frac{3}{2}\left(\frac{j}{j+1}\right) Nk_B T_c \sigma^2 - g\mu_B BjN\sigma + \frac{1}{2K}\omega^2 - T(S_{mag} + S_{lat}) + P\omega. \quad (2.33)$$

Here, N is the number of magnetic atoms, k_B is the Boltzmann constant, σ is the normalized magnetization, g is the Landé factor and B is the external magnetic field, $K = -1/V(\partial V/\partial P)_{T,B}$ is the compressibility, ω is the volume change, S_{mag} is the magnetic entropy and S_{lat} is the lattice entropy.

In order to obtain the magnetic state equation, the variables σ and ω should assume values that minimize the Gibbs free energy. Therefore, fixing σ and assuming that S_{mag} depends only on σ, the Gibbs energy is minimized for the following volume deformation:

$$\omega = \frac{3}{2}\left(\frac{j}{j+1}\right) Nk_B T_0 \beta \sigma^2 - PK + KT\frac{\partial S_{lat}}{\partial \omega}. \quad (2.34)$$

Neglecting the last term and substituting the above equilibrium deformation into Eq. 2.33, we get a final expression for the Gibbs free energy. Performing the derivative of this Gibbs free energy with respect to σ and considering the relation $\sigma = B_j^{-1}(\sigma) = -\frac{1}{Nk_B}\frac{\partial S_mag}{\partial \sigma}$ we get the following magnetic state equation [102]:

$$\sigma = B_j\left\{\frac{1}{T}\left[\left(\frac{T_0 j}{j+1}\right)(3 - 3\beta PK)\sigma + \frac{g\mu_B j}{k_B}B + \frac{9}{5}\left(\frac{(2j+1)^4 - 1}{[2(j+1)^4]}\right)T_0\eta\sigma^3\right]\right\} \quad (2.35)$$

where B_j is the Brillouin function and the parameter η is given by:

$$\eta = \frac{5}{2}\left(\frac{[4j(j+1)]^2}{[(2j+1)]^4 - 1}\right) Nk_B K T_0 \beta^2. \quad (2.36)$$

This parameter η controls the nature of the magnetic phase transition in the model.

The first order phase transition occurs under the following condition [102]:

$$PK\beta > 1 - \eta. \tag{2.37}$$

Note that the traditional Bean-Rodbell model assumes that the lattice entropy change across the first order transition is negligible and it greatly simplifies the mathematical algorithm. However, this restrictions of the model can be lessened by approximating the lattice entropy when $T > \theta_D$ by the expression

$$S_{lat} = 3R\left[\ln T - \ln \theta_D + \frac{4}{3}\right]. \tag{2.38}$$

By doing so, the colossal MCE is claimed to be explained and the readers are recommended to follow the discussion in reference [85] if interested. The fundamental physical concepts and mathematical treatment are similar to the above so we won't discuss the detail of the extended model in this thesis.

3. MEASUREMENT METHODS FOR THE SPECIFIC HEAT

3.1 Introduction

A process involving only infinitesimal changes in the thermodynamic coordinates of a system is known as a infinitesimal process. For such a process, the general statement of the first law becomes

$$dU = dQ + dW. \tag{3.1}$$

If the infinitesimal process is quasi-static, then dU and dW can be expressed in terms of thermodynamic coordinates only. An infinitesimal quasi-static process is one in which the system passes slowly from an initial equilibrium state to a neighboring equilibrium state. It should be recognized that dU refers to a property within the system (internal energy), whereas dQ and dW are not related to properties of the system; rather, they refer to the transfer of energy to the system by surrounding objects. The quantity dW is expressible in terms of the product of an intensive generalized force and an extensive generalized displacement such as $-PdV$ for a hydrostatic system, $\mathscr{F}dL$ for a stretched wire, $\mathscr{E}dZ$ for an electrochemical cell, $Ed\mathscr{P}$ for a dielectric slab and $\mu_0 HdM$ paramagnetic systems.

Eq. 3.1 shows that the internal energy can be changed either by heat or work. As a practical matter, it is much easier to produce heat from combustion or electricity passing through a resistor than it is to produce work from falling weights or compressed springs. As a result, when systematic experiments were performed to measure the capability of a substance to store internal energy, heat rather than work was used, and the results came to be known as the heat capacity of the sample. If a system experiences a change of temperature from T_i to T_f during the transfer of Q units of heat, the average heat capacity of the system is defined as the ratio:

$$\text{Average heat capacity} = \frac{Q}{T_f - T_i}. \tag{3.2}$$

As both Q and $(T_f - T_i)$ become smaller, this ratio approaches a limiting value, known as the heat capacity C, thus:

$$C = \lim_{T_f \to T_i} \frac{Q}{T_f - T_i} = \frac{dQ}{dT}. \tag{3.3}$$

Calorimetric data are indispensable in any thermodynamic study. Specific heat measurements and their corresponding entropies are regarded as the most reliable direct measurements of thermodynamic quantities.

In this chapter the various methods for the measurement the of specific heat are compared. These common used experimental methods are [103]:

1. Adiabatic calorimetry
2. Differential scanning calorimetry
3. AC calorimetry
4. Heat-pulse methods

3.2 Adiabatic Calorimetry

This is one of the oldest methods for the measurement of specific heat. The basic principle of this method is that a steady heat input is supplied to the sample and the resultant temperature rise of the sample is measured. By equating the heat supplied

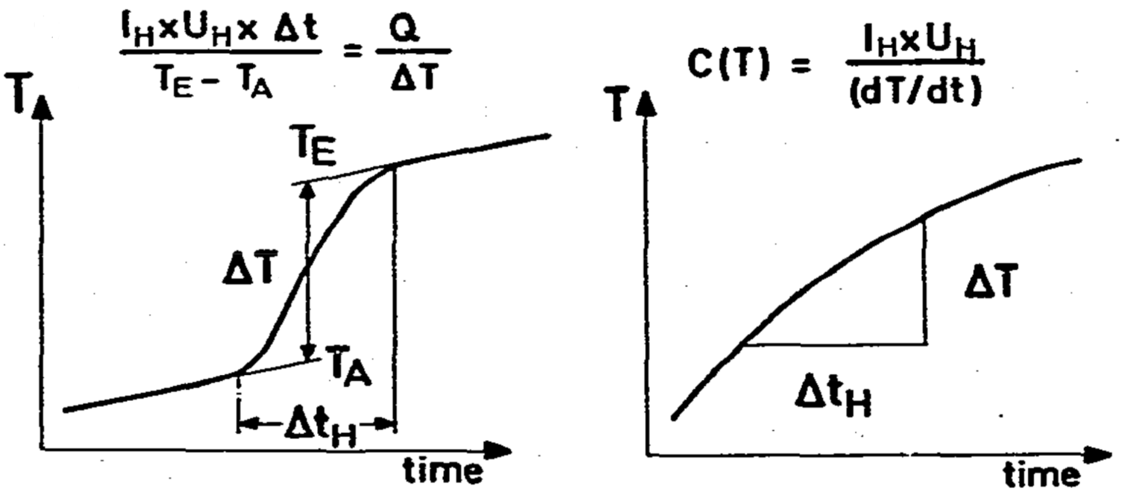

(a) Nernst Step heating method (b) Continuous heating method

Figure 3.1: Principles of adiabatic calorimetry. I_H, Heating current; U_H, voltage across heater resistance; T_E, final temperature (after heating); T_A, initial temperature (before heating); Δt_H, heating time; ΔT, temperature increment. Reprinted with permission from [104].

to the sample, the heat capacity can be calculated [104].

$$C_p(T) = \lim_{\Delta T \to 0} \frac{Q}{\Delta T}. \tag{3.4}$$

In experiments, the heat given to the sample can be pulsed or continuous as illustrated in Fig. 3.1. In an adiabatic calorimeter the heat exchange between the sample and the environment has to be reduced as far as possible. However, the complete thermal isolation of the sample from the surroundings is very difficult to achieve and the corrections for the heat loss to the surroundings are hard to evaluate. This method is primarily used for the study of chemical reactions.

3.3 Differential Scanning Calorimetry

In this method, the reference material is heated at a constant rate. The sample and the reference are maintained at the same temperature by supplying different quantities of heat. By recording the power difference between the sample and the reference, the heat capacity can be evaluated by the following formula

$$C_p(T) = K \times \frac{\Delta P}{\frac{dT}{dt} \times m} \tag{3.5}$$

where

K = Calibration constant

ΔP = heater power difference between the sample and the reference

m = the mass of the sample.

The basic advantage of the differential techniques is firstly the high relative accuracy when the absolute heat capacity of the reference sample is confirmed. Secondly the systematic errors due mainly to uncontrolled heat exchange with the surroundings are eliminated since both samples are subject to identical experimental conditions. However, the internal equilibrium time within the sample and the surroundings causes uncertainty and difficulty in obtaining the absolute heat capacity.

3.4 AC Calorimetry

This method was originally developed by Sullivan and Seidel [105] as illustrated in Fig. 3.2. The basic principle of this method is that a periodic heat input is supplied to the sample. It can be shown that the resultant equilibrium temperature of the sample contains a dc part and an ac part.

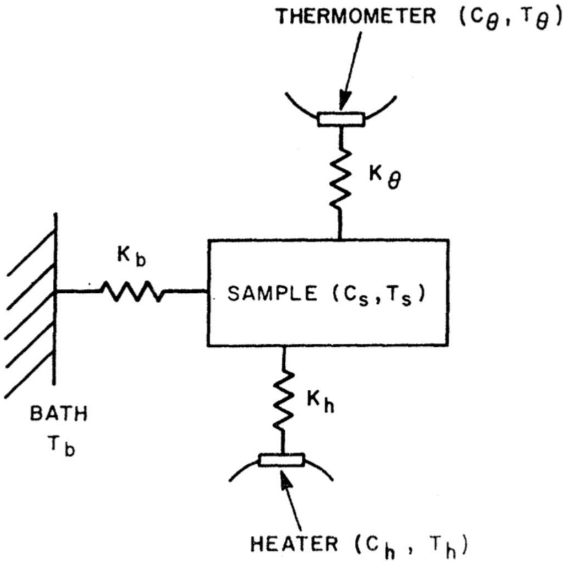

Figure 3.2: Schematic diagram of the Sullivan-Seidel AC calorimetry method. Reprinted with permission from [105].

The heater power in the circuit is [106]

$$P = P_{ac}[1 + \cos(2\omega t)]. \tag{3.6}$$

The temperature variations are controlled to be sufficiently small so the heat capacity can be considered constant. The steady-state temperature response due to the heater will be $T_\theta = T_b + T_{dc} + |T_{ac}|\cos(2\omega t + \phi)$ and

$$|T_{ac}| = \frac{P_{ac}}{2\omega C_p(T)}|\sin(\phi)| \tag{3.7}$$

A sample with large thermal conductivity is required in this measurement in order for the prevention of temperature gradients inside the sample. The accuracy will be lower if the thermal conductivity of the sample is too small.

Figure 3.3: The overview of a Quantum Design PPMS.

3.5 Heat-pulse Method

This method is the same as the thermal relaxation-time method, which has been wide used for decades since it was proposed [107]. However, this method becomes inappropriate when the specific heat has steep changes during a small temperature range and this issue will be addressed in Sec. 3.5.3.

The discussion in this section is mostly based on the Physical Properties Measurement System (PPMS) manufactured by Quantum Design. The overview of the instrument is shown in Fig. 3.3 and the schematic experimental apparatus for heat-capacity measurements is set up as in the Fig. 3.4.

In this technique, the sample is heated by power P_0 during a certain time. The thermometer on the platform starts to record the data once the heater is turned on as shown in Fig. 3.5

Two mathematical analysis methods are used in the built-in PPMS software. One

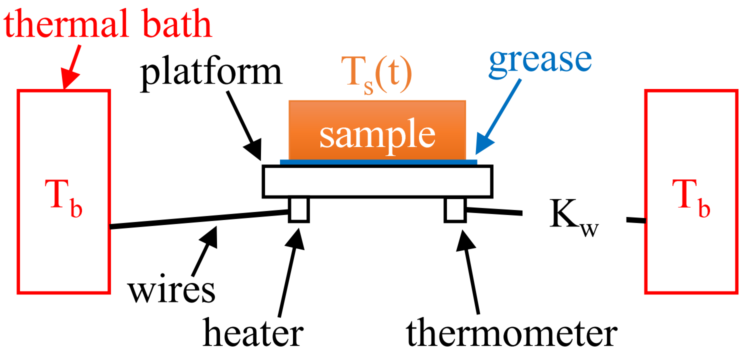

Figure 3.4: Schematic experimental apparatus for PPMS heat-capacity measurements.

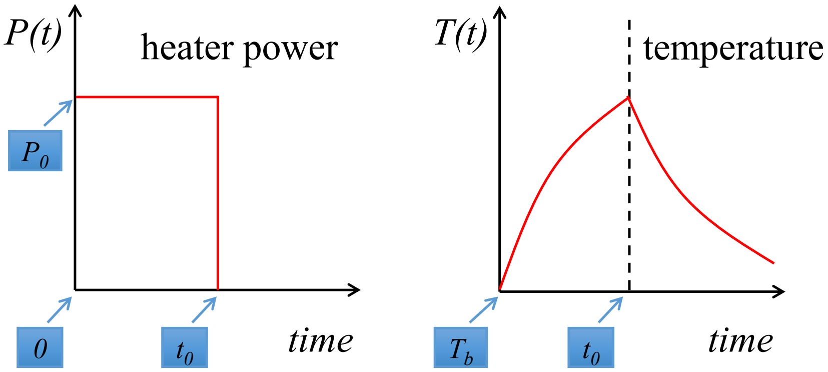

Figure 3.5: Principles of heat-pulse calorimetry: A square-pulse of height P_0 is applied (upper diagram), resulting in a temperature change of the sample platform the lower diagram.

is a simple model (also known as one-τ) and the other is called the two-τ model. These two models use different mathematical methods to do the analysis but the experimental measurement is identical.

3.5.1 Simple Model

In the simple model, the temperature T of the platform as a function of time (t) obeys the equation

$$C_{total}\frac{dT}{dt} = -K_w(T - T_b) + P(t) \tag{3.8}$$

where C_{total} is the total heat capacity of the sample and sample platform; K_w is the thermal conductance of the supporting wires; T_b is the temperature of the thermal bath (puck frame); and $P(t)$ is the power applied by the heater. Notice that K_w is considered for the case of a small temperature pulse and its value has to be calibrated before doing the sample measurements. The heater power $P(t)$ is equal to P_0 during the heating portion of the measurement and equal to zero during the cooling portion. Supposing that the heater is turned on at $t = 0$ and is turned off at $t = t_0$, the solution of this equation is

$$T(t) = \begin{cases} P_0\tau(1 - e^{-t/\tau})/C_{total} + T_b & \text{if } 0 \leq t \leq t_0 \\ P_0\tau(1 - e^{-t/\tau})e^{-(t-t_0)/\tau}/C_{total} + T_b & \text{if } t \geq t_0 \end{cases} \tag{3.9}$$

where $\tau = \frac{K_w}{C_{total}}$, P_0 and t_0 are controlled experimentally and $T(t)$ is the reading on the thermometer on the platform. C_{total}, K_w and T_b are varied in order to obtain a minimum of S

$$S = (C_{total}, K_w, T_b) = \sum_i (T(t_i) - T_i) \tag{3.10}$$

where t_i is the measured time, $T(t_i)$ is the temperature in Eq. 3.9 and T_i is the measured temperature.

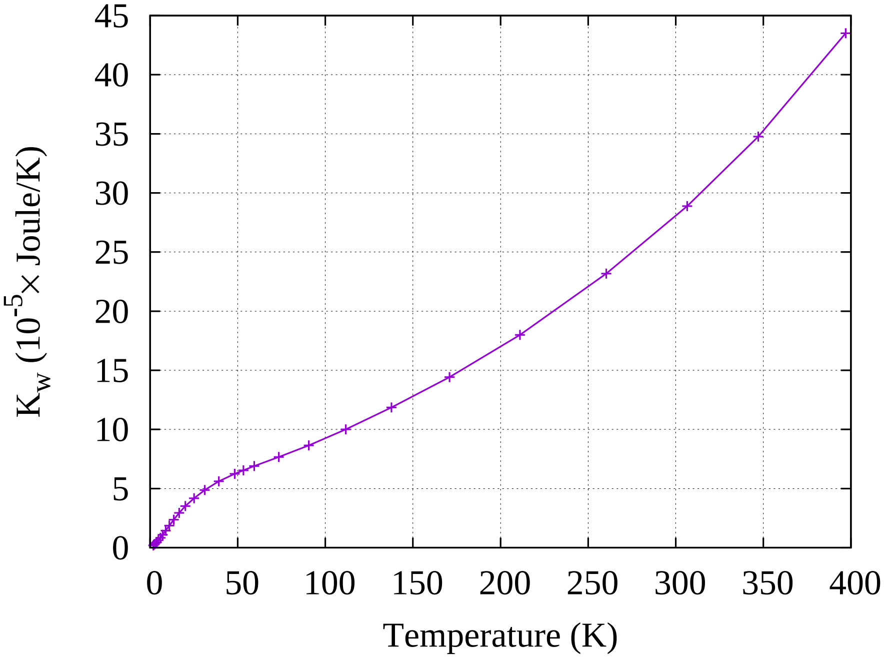

Figure 3.6: The wire conductance vs. temperature from the calibration measurement.

The simple model assumes that the sample and sample platform are in good thermal contact with each other and are at the same temperature during the measurement. This model is used in the calibration when only the grease is applied on the sample platform. One of the typical K_w measurement is shown in Fig. 3.6.

3.5.2 Two-τ Model

The two-τ model is usually used when the sample is placed on top of the grease. The grease temperature is assumed to be the same as the platform temperature. This model simulates the effect of heat flowing between the sample platform and sample through the grease, and the effect of heat flowing between the sample platform and puck. The following equations express this model [108, 109]:

$$\begin{aligned} C_{platform}\frac{dT_p(t)}{dt} &= P(t) - K_w(T_p(t) - T_b) + K_g(T_s(t) - T_p(t)) \\ C_{sample}\frac{dT_s(t)}{dt} &= -K_g(T_s(t) - T_p(t)), \end{aligned} \tag{3.11}$$

where $C_{platform}$ is the heat capacity of the sample platform with the grease, C_{sample} is the heat capacity of the sample, and K_g is the thermal conductance between the two due to the grease. The respective temperatures of the platform and sample are given by $T_p(t)$ and $T_s(t)$.

Suppose that the heater is turned on at $t = 0$ and is turned off at $t = t_0$. The solution of this equation is

$$T(t) = \begin{cases} \frac{P_0}{K_w} + T_b + \frac{P_0}{2\beta K_w} + \frac{P_0}{2\beta K_w}\left[\frac{e^{t/\tau_2}}{\tau_1} - \frac{e^{t/\tau_1}}{\tau_2}\right] & \text{if } 0 \leq t \leq t_0 \\ P_0\tau(1 - e^{-t/\tau})e^{-(t-t_0)/\tau}/C_{total} + T_b & \text{if } t \geq t_0. \end{cases} \tag{3.12}$$

Neither the simple model nor the two-τ model are applicable to temperature regions involving a first order transitions. In next section, we will describe an improved experimental method and modified model to overcome this issue.

3.5.3 Across a First-order Transition

As described above, the simple model and 2-τ model are built into PPMS for the automated measurements. This technique is both fast and accurate for temperatures not too high (T <400 K), but some problems can arise when dealing with sharp structures in the heat capacity especially when a first-order transition is involved.

When the sample temperature crosses a first-order or a very sharp second-order phase transition, the temperature relaxation curve is modified as illustrated in Fig. 3.7. When the sample temperature crosses the first-order phase transition, a plateau ap-

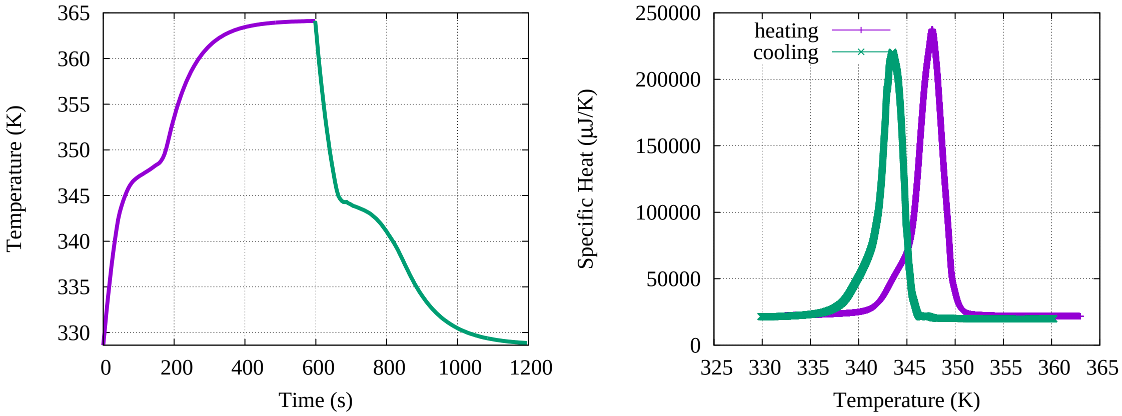

Figure 3.7: Example of raw temperature response data with a plateau near a first-order transition and the corresponding heat capacity obtained by the analysis described in the text.

pears in the relaxation curve. In this case, the conventional 2-τ fitting model must give an erroneous curve since the heat capacity is no longer constant over the temperature increment. Various alternative analysis methods have been proposed to account for this in the past few years [110, 111], with some questions such as how to properly account for the heat leak and wire conductance terms remaining not entirely resolved.

In our approach, we focused on the "scanning method" instead of fitting the whole curve. Experimentally, the heater pulse and measurement time have to increase in order to cover the whole transition [111]. In this method, extra time must be allowed in order to increase the stability of the initial temperature. We take the advantage of the PPMS which can record the temperature vs. time during and after a single heat pulse. To do the analysis point-by-point, we write down the heat capacity equation obtained from the 1-τ model

$$C_{total}(T) = \frac{-K_w(T)(T - T_b) + P}{dT/dt}. \tag{3.13}$$

where P is the given constant heat power, T is the sample temperature from the thermometer on the platform, T_b is the initial temperature and K_w is the wire conductance. Instead of treating the wire conductance as a fitting variable, we started with the wire conductance from the small ΔT calibration measurement as shown in Fig. 3.6. However, the experimental conditions entail a rather large ΔT, necessitating an additional analysis step.

These issues have been addressed in various ways [33, 110, 111], including models introduced to consider changes in the wire conductance and also changes in the base temperature during a long heat pulse. In our study, to probe the phase transition region we recorded changes in temperature during a long heat pulse, turned on in the temperature range of complete martensite and turned off when complete austenite was achieved. This requires optimizing the pulse settings by trial and error to cover the transition region, and long wait times to increase the base temperature stability. The raw temperature vs. time traces were obtained from the system controller, and analyzed separately. From measurements away from the hysteresis region using the 2-τ measurement scheme, we also determined that the thermal conductance of the grease exceeds that of the wires by a factor of at least 100 in all cases. This ensured that the temperature discrepancy between the platform and sample is negligible.

In order to calibrate K_w for the conditions of large $\Delta T (= T - T_b)$ in Eq. 3.13, we made use of the lack of hysteresis outside of the transition, as known physically and confirmed in our measurements. Because of this feature, for heating-cooling cycles bracketing the transition, the 2-τ model remains valid for extracted K_w values at large-ΔT. In the small-ΔT region, the conditions of the standard calibration procedure are reproduced, so the standard calibration provided these values. In our study, a modified wire conductance K'_w is used

$$K'_w(T) = K_w((1-x)T_b + xT), \tag{3.14}$$

where $K_w(T)$ is obtained from the standard calibration, and a single extrapolation parameter x was adjusted until the heating and cooling curves became consistent for temperatures above the transition. Finally, from the time recordings of temperature during and after the heat pulse, we obtained the heating and cooling specific heats by utilizing Eq. 3.13 and K'_w.

4. THEORETICAL ENTROPY CONTRIBUTIONS

The total entropy for our materials should be described by the three main contributions which are the electronic, vibrational and magnetic:

$$S_{total} = S_{el} + S_{vib} + S_{mag}. \tag{4.1}$$

In the following section, I will introduce the fundamental concepts of each contribution.

4.1 Vibrational Contributions from Debye Model

In this section an expression for the vibration specific heat will be written down. This expression will then be approximated by something that can actually be evaluated. The method of approximation used is called the Debye model.

Consider a crystal with N atoms in the each unit cell and the volume of each unit cell is V. In the harmonic approximation, the system of N vibrating atoms is equivalent to a system of $3N$ independent (one-dimensional) oscillators of frequency $\omega = \omega(q,p)$, where p and q represent the two canonical variables of the oscillator. The average number of phonons in mode (q,p) is

$$\bar{n}_{q,p} = \frac{1}{e^{\hbar\omega_{q,p}/k_B T} - 1}. \tag{4.2}$$

The average energy per mode is

$$\hbar\omega_{q,p}\bar{n}_{q,p}, \tag{4.3}$$

so the average vibrational energy of the harmonic crystal is the sum of independent phonon contributions

$$U_{vib} = \sum_{q,p} \left[\frac{\hbar\omega_{q,p}}{\hbar\omega_{q,p}/k_B T - 1} + \frac{1}{2}\hbar\omega_{q,p} \right] \tag{4.4}$$

The specific heat at constant volume is then given by

$$C_{vib}(T) = \frac{\partial U_{vib}}{\partial T} = \frac{\partial}{\partial T} \sum_{q,p} \frac{\hbar\omega_{q,p}}{e^{\hbar\omega_{q,p}/k_B T} - 1}. \tag{4.5}$$

The above expression allows the numerical calculation of the lattice heat capacity of crystals, once the phonon dispersion curves $\omega_{q,p}$ are known. The Debye model is a model based on the exact expression in Eq. 4.5 in which the sum is evaluated by replacing it by an integral in which there is a specific density of states. Any three-dimensional crystal, with or without a basis, presents three acoustic branches with linear dispersion $\omega = v_s q$ for small q. For simplicity we assume the same sound velocity v_s for each of the three acoustic branches and extend the linear dispersion relation to the whole Brillouin zone. To avoid inessential details, the Debye approximation replaces the the Brillouin zone with a sphere of equal volume. We indicate with q_D the radius of the sphere and define $\omega_D = v_s q_D$ as the cutoff Debye frequency. The density of phonon states corresponding to a branch with linear dispersion relation $\omega = v_s q$ is easily obtained. In fact the number of states $D(\omega)d\omega$ with frequency in the interval $[\omega,\, \omega + d\omega]$ equals the number of states in reciprocal space with wavevector between $[q,\, q + dq]$; namely:

$$D(\omega)d\omega = \frac{V}{(2\pi)^3} 4\pi q^2 dq = \frac{V}{(2\pi)^3} 4\pi \frac{\omega^2}{v_s^2} d\frac{\omega}{v_s}. \tag{4.6}$$

It follows that

$$D(\omega) = \frac{V}{(2\pi)^3} 4\pi \frac{\omega^2}{v_x^3} = \frac{N\Omega}{(2\pi^3)} \frac{4\pi q_D^3}{3} \frac{3\omega^2}{\omega_D^3} = N \frac{3\omega^2}{\omega_D^3}, 0 \le \omega \le \omega_D, \tag{4.7}$$

where N is the number of unit cells of the crystal. Therefore, Eq. 4.5 can be rewritten as the integration over the frequencies [68, 112, 113]

$$C_{vib}(T) = \frac{\partial}{\partial T}\left(3\int_0^{\omega_D} N\frac{3\omega^2}{\omega_D^3}\frac{\hbar\omega}{e^{\hbar\omega/k_BT}-1}d\omega\right) = 9Nk_B\left(\frac{T}{\theta_D}\right)^3\int_0^{\theta_D/T}\frac{x^4e^x}{(e^x-1)^2}dx. \tag{4.8}$$

where $\theta_D = \hbar\omega_D/k_B$ is the Debye temperature. The vibrational entropy contribution can be obtained from the integration of the specific heat

$$S_{vib}(T) = \int\frac{C_{vib}(T)}{T}dT = -3Nk_B\ln\left[1-e^{-\frac{\theta_D}{T}}\right] + 12Nk_B\left(\frac{T}{\theta_D}\right)^3\int_0^{\theta_D/T}\frac{x^3}{e^x-1}dx. \tag{4.9}$$

However, the Debye model simplifies the motion of atoms as that of ideal harmonic oscillators, and this causes the deviation compared with the experimental data. This deviation usually is most significant below the Debye temperature and it becomes smaller as the temperature goes higher. Overall, the Debye model has been extremely successful in explaining specific heats of solids[114].

4.2 Electronic Contributions in Metals

Up to this point, we have only considered contributions to the heat capacity from vibrations within the solid. In metals, the free conduction electrons also contribute to the specific heat. In the free electron model of metals, the conduction electrons are treated as a perfect gas obeying Fermi-Dirac statistics. Interactions of the electrons with the positively charged atomic ions and with the other electrons are neglected.

A major success of Fermi's consideration of electrons in metals is that it could explain the excess specific heat in metals (beyond that given by the phonons). Combining the density of states and thermal distribution, the total electron energy is given by an integral over all energies:

$$U_{el} = \int_0^\infty D(E)f(E,T)EdE, \tag{4.10}$$

where E is the energy of free electrons, $D(E)$ is the density of states and $f(E,T)$ is Fermi-Dirac distribution. Consider the perturbation of the Fermi-Dirac distribution due to temperature as shown in Fig. 4.1. The electronic contribution of specific heat can be expressed as

$$\begin{aligned} C_{el}(T) = \frac{\partial U_{el}}{\partial T} = \frac{\partial}{\partial T}(U_{el} - NE_F) = \frac{\partial}{\partial T}\int_0^\infty D(E)f(E,T)(E-E_F)dE \\ = \int_0^\infty D(E)\frac{\partial f(E,T)}{\partial T}(E-E_F)dE, \end{aligned} \tag{4.11}$$

where

$$\frac{\partial f(E,T)}{\partial T} = \frac{e^x}{(1+e^x)^2}\frac{E-E_F}{k_BT^2} \text{ with } x = \frac{E-E_F}{k_BT}. \tag{4.12}$$

The term $\frac{\partial f}{\partial T}$ only becomes large near $E = E_F$, so we can approximate $D(E) \approx D(E_F) = const.$ Thus

$$C_{el} = D(E_F)\int_0^\infty \frac{e^x}{(1+e^x)^2}\frac{(E-E_F)^2}{k_BT^2}dE = k_B^2TD(E_F)\int_{-\frac{E_F}{k_BT}}^\infty \frac{e^x x^2}{(1+e^x)^2}dE \tag{4.13}$$

If $E_F \gg k_BT$, then $-\frac{E_F}{k_BT} \to -\infty$, and the integral becomes

$$\int_{-\infty}^\infty \frac{x^2e^x}{(e^x+1)^2} = \frac{\pi^2}{3} \tag{4.14}$$

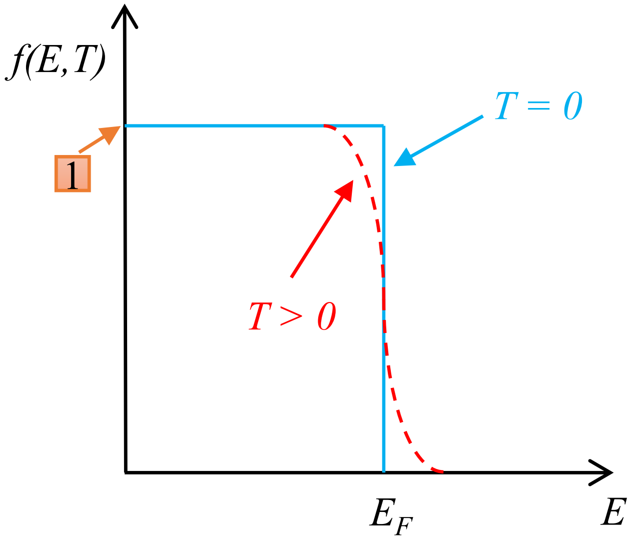

Figure 4.1: Fermi-Dirac distribution for $T = 0$ and for T slightly above zero.

Thus the specific heat becomes [112]

$$C_{el}(T) = \frac{\pi^2}{3} k_B T D(E_F), \tag{4.15}$$

and the electronic entropy contribution becomes

$$S_{el}(T) = \int_0 \frac{C_{el}(T)}{T} dT = \frac{\pi^2}{3} k_B T D(E_F). \tag{4.16}$$

The above linear variation of electronic specific heat is valid only at low temperatures ($T << T_F$, note that T_F generally very large so it is valid in metal at most temperatures). The electronic contribution generally becomes negligible at high temperatures since the vibrational contribution dominates.

4.3 Magnetic Contribution

The entropy S_{mag} at a given field (H) due to the orientation of otherwise non-interacting ions can be written in terms of the partition function:

$$S_{mag} = R\frac{d}{dT}(T \ln Q_{mag}), \tag{4.17}$$

where Q_{mag} is the sum of all magnetic states

$$Q_{mag} = \sum_{m=-J}^{m=J} e^{mg\mu_B H/k_B T}. \tag{4.18}$$

Carrying out the differentiation one finds

$$S_{mag} = R\left[\ln Q_{mag} - \frac{\sum_{m=-J}^{m=J} \frac{mg\mu_B H}{k_B T} e^{mg\mu_B H/k_B T}}{\sum_{m=-J}^{m=J} e^{mg\mu_B H/k_B T}}\right]. \tag{4.19}$$

The first term can be simplified by expanding the summation

$$\begin{aligned} \ln Q_{mag} &= \ln \sum_{m=-J}^{m=J} e^{mg\mu_B H/k_B T} \\ &= \ln[e^{(J+1/2)g\mu_B H}/k_B T - e^{-(J+1/2)g\mu_B H/k_B T}] - \ln[e^{g\mu_B H/2k_B T} - e^{-g\mu_B H/2k_B T}] \\ &= \ln \sinh\left(\frac{J+\frac{1}{2}}{J}y\right) - \ln \sinh\left(\frac{1}{2J}y\right), \end{aligned} \tag{4.20}$$

with

$$y = \frac{Jg\mu_B H}{k_B T}. \tag{4.21}$$

In addition, the second term in Eq. 4.19 can be rewritten in terms of

$$M = \frac{\sum_{m=-J}^{m=J} mg\mu_B e^{mg\mu_B H/k_B T}}{\sum_{m=-J}^{m=J} e^{mg\mu_B H/k_B T}} = Jg\mu_B B_J\left(\frac{Jg\mu_B H}{k_B T}\right) = Jg\mu_B B_J(y). \tag{4.22}$$

Therefore, the final expression of the entropy is obtained as

$$S_{mag} = R\left[\ln\sinh\left(\frac{J+\frac{1}{2}}{J}y\right) - \ln\sinh\left(\frac{1}{2J}y\right) - yB_J(y)\right]. \tag{4.23}$$

S_{mag} varies from $R\ln(2J+1)$ at $y=0$ to zero as y approaches infinity ($T \to 0$ or $H \to \infty$).

The physical principle of this model is simple. In the absence of a magnetic field, the random orientation of the angular angular momentum vectors of the (magnetically active) ions introduces an entropy $R\ln(2J+1)$ in excess of that due to lattice vibrations and electronic carrers. The application of a strong magnetic field, while the material is kept at constant temperature, tends to orient all the moments into the direction of the magnetic field, reducing the entropy toward zero.

The error made in this analysis lies in the assumption that a random orientation of the magnetic moments would prevail at all temperatures in the absence of a field. If any interaction at all exists between the moments, either through a true magnetic force or owing to an interaction with the electric crystalline field, some particular configuration with zero entropy will be stable at 0 K. However, the entropy will approach the high temperature value of $R\ln(2j+1)$ only at temperatures for which kT exceeds the energy of interaction[115].

5. ENTROPY ENHANCEMENT OF GIANT MAGNETOCALORIC EFFECT

5.1 Motivation

The magnetocaloric effect (MCE) is defined as an intrinsic thermodynamic property of magnetic solids, which manifests as an adiabatic temperature change or as an isothermal entropy change due to the application of a magnetic field. Materials showing MCE have been a source of growing interest because of their potential for the replacement of vapor-compression refrigeration in use today due to their environmentally friendly and energy efficient prospects [3]. Recently, a giant MCE at room temperature based on a first-order phase transition was observed in several materials, such as, Ni-Mn based Heusler alloys [12, 37–39, 116–119], $Gd_5Si_{2-x}Ge_x$ [5], MnAs-based compounds [9, 51, 120] and $LaFe_{13-x}Si_x$ [7, 121]. Composition maps in the Ni-Mn-In system have been recently developed allowing the design of alloys at different working temperatures [122] and the austenite phase can be tuned to be either paramagnetic or ferromagnetic. In this chapter, we present Ni-Mn-In materials with four different compositions. Two of them have a ferromagnetic austenite phase while the others have a paramagnetic austenite phase.

In general, first-order magnetic transitions are often accompanied by structural transitions, which enforce the magnetization change suddenly and, consequently, enhance the magnetocaloric effect. Therefore magnetocaloric materials often display magneto-elastic or magneto-structural transitions. The entropy of a MCE material includes contributions due to magnetism (S_{mag}), lattice vibration (S_{vib}) and conduction electrons (S_{el}). Thus, the isothermal field-induced total entropy change can be expressed by:

$$\Delta S_{iso} = \Delta S_{mag} + \Delta S_{vib} + \Delta S_{el}. \tag{5.1}$$

Theoretically, a giant magnetocaloric effect can be obtained if the above contributions have the same sign. However, they may partially cancel each other if they have opposite signs.

One of the common ways to understand the inverse MCE in Heusler alloys is to characterize the field-induced isothermal entropy through the magnetization. However, this method may suffer from non-equilibrium thermodynamic states in the coexistence phase region especially when the external field used to drive the complete martensitic transformation is too large to achieve experimentally. Hence, this method may fail to interpret the maximum field-induced entropy if the experiment is not performed properly. On the other hand, the temperature region of the first order transition is usually small and it is easy to scan the temperature across the complete martensitic transformation. Also, calorimetric data are indispensable in any thermodynamic study. Heat capacity measurements and their corresponding entropies are regarded as the most reliable direct measurements of thermodynamic quantities. The maximum isothermal entropy can be obtained from calorimetric measurement at zero field.

In the following section, we will give a introduction of vibrational and electronic entropy contributions. In the calorimetric experiment, we develop a method to cross the first order transitions and evaluate the additional entropy by subtracting the well-known vibrational and electronic contributions. Four samples with different compositions are studied and strong magnetoelastic couplings have been found in two of them whereas the others appear to agree well with the maximum magnetic entropy due to local Mn moments ($J = 2$).

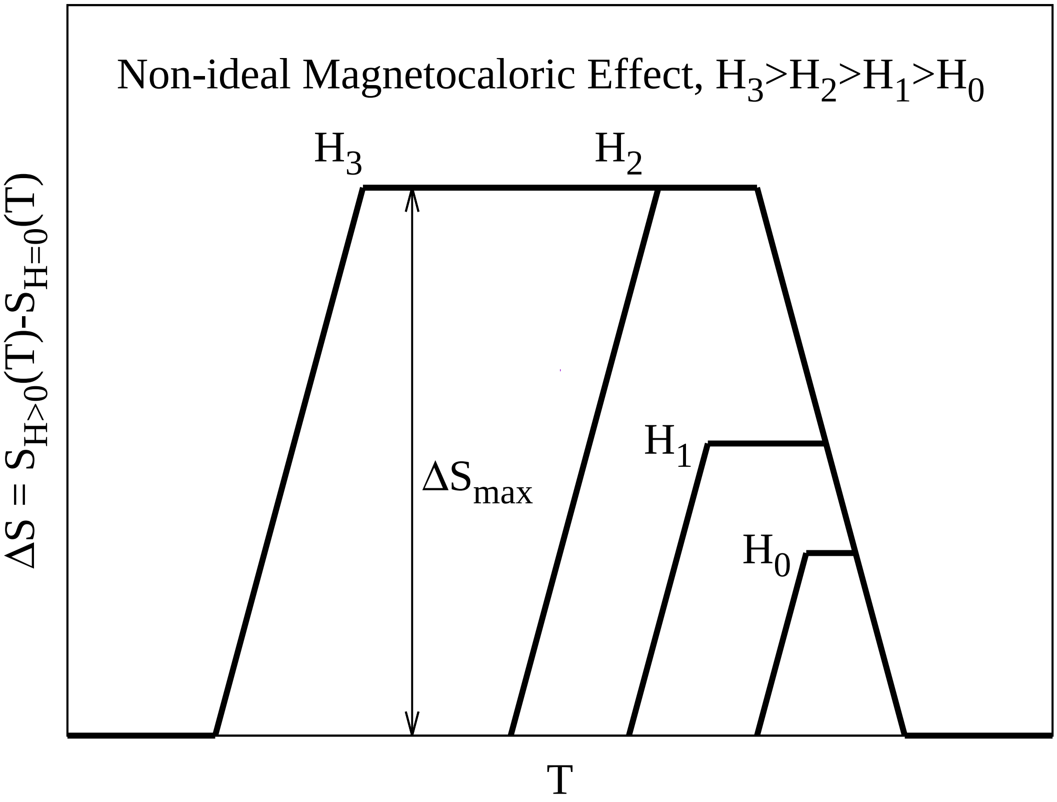

Figure 5.1: Schematic field-induced isothermal entropy change for non-ideal magnetocaloric effect materials is shown. ΔS saturation can be observed if the applied field is large enough to drive the martensitic transformation completely.

5.2 Entropy Change in Calorimetric Processes

A method to determine the entropy change of a system is to determine the specific heat from T_1 up to the wanted T_2. If we know the specific heat of a system over this temperature range, we can then find the corresponding entropy change. This is given by [123]:

$$S(T_2) - S(T_1) = \int_{T_1}^{T_2} \frac{C}{T} dT. \tag{5.2}$$

If C is measured at constant volume, $S(T_2)$ and $S(T_1)$ refer to that volume. If $C(T)$ is measured at constant pressure, $S(T_2)$ and $S(T_1)$ then refer to that pressure. In many cases the measurement of an entropy change thus involves simply the measurement of the heat capacity of the substance. The third law of thermodynamics requires that the entropy of all states of a system in internal thermodynamic equilibrium should be the same at the absolute zero of temperature. Therefore we can set the entropy at absolute zero temperature to be any finite constant and for convenience, we set it equal to zero. We can then rewrite our definition of the entropy as

$$S(T) - S(T=0) = S(T) = k_B \ln \Omega = \int_0^T \frac{C}{T} dT, \tag{5.3}$$

where Ω is the number of microstates consistent with the macroscopic configuration. The counting of states is relative to the reference state of absolute zero, which corresponds to the entropy of $S(T = 0)$. This equation provides the basis for our statistical interpretation of entropy and gives an experimental way to evaluate its value directly. The total entropy for our materials should be described by the three main contributions which are the electronic, vibrational and magnetic:

$$S_{total} = S_{el} + S_{vib} + S_{mag}. \tag{5.4}$$

In the following section, I will discuss our specific heat results and magnetization measurements. Last but not least, any additional anomalous entropy contributions can be obtained from our analysis.

5.3 Sample Preparation

Bulk polycrystalline Ni-Mn-In alloys were prepared using arc melting in a protective argon atmosphere from 99.9% pure constituents. Ingots were flipped and re-melted three times to promote homogeneity. The resulting alloy buttons were cut into plates using a high speed diamond wafering blade. The samples were quenched in ice water after they were then homogenized (solutionized) at 900°C for 24 hours in a quartz vial under a protective argon atmosphere to prevent oxidation.

Electron microprobe measurements were carried out using wavelength dispersive spectrometry (WDS) methods on a Cameca SX50 equipped with four wavelength-dispersive x-ray spectrometers and an electron backscattering image from these measurements for the $Ni_{50}Mn_{36}In_{14}$ sample is shown in Fig. 5.2. We prepared materials for the studies described here with four targeted compositions which are, $Ni_{50}Mn_{36}In_{14}$, $Ni_{50}Mn_{35.5}In_{14.5}$, $Ni_{48}Mn_{35}In_{17}$ and $Ni_{48}Mn_{38}In_{14}$. The final compositions were found to be $Ni_{49.54}Mn_{36.12}In_{14.34}$, $Ni_{49.88}Mn_{35.70}In_{14.42}$, $Ni_{49.53}Mn_{35.22}In_{15.22}$ and $Ni_{47.22}Mn_{38.45}In_{14.33}$ respectively, which is very close to the targeted compositions. In this chapter, I label the samples as $Ni_{50}Mn_{36}In_{14} \rightarrow$Ni50A, $Ni_{50}Mn_{35.5}In_{14.5} \rightarrow$Ni50B, $Ni_{48}Mn_{35}In_{17} \rightarrow$Ni48A and $Ni_{48}Mn_{38}In_{14} \rightarrow$Ni48B.

The sample preparation and WDS were done by our collaborators from the School of Materials Science and Engineering in Shanghai Jiaotong University by Yujin Huang and Department of Mechanical Engineering in Texas A&M University by Nickolaus Bruno. Also, Nickolaus Bruno performed the SQUID measurements, whereas I carried out all specific heat measurements and analysis. An identical

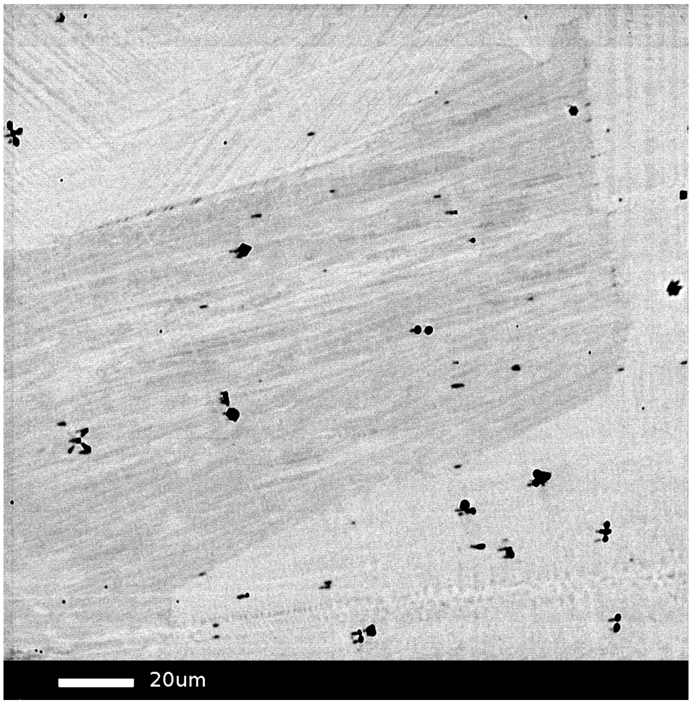

Figure 5.2: Back-scattered electron image of the $Ni_{50}Mn_{36}In_{14}$ sample after heat treatment (scale bar $20\mu m$ in the bottom of the figure). The very dark regions are empty cavities and image contrast shows grain size.

preparation method was used used for all different compositions of Ni-Mn-In shown in this thesis.

5.4 Magnetization Analysis

The magnetization measurements were carried out using a Quantum Design Magnetic Property Measurement System by Nickolaus M. Bruno. The results shown in Fig. 5.3 and Fig. 5.4 for the four samples indicate a martensitic transition from a paramagnetic/ferromagnetic austenite to an anti-ferromagnetic (or low-moment) martensite upon cooling. The austenite to martensite transformation is observed on cooling the samples and the reverse transformation is observed on sample heating. These transformations are in good agreement with reported phase diagrams for similar compositions [36], with both Ni_{50} compositions remaining paramagnetic at all temperatures above the martensitic transition, while the Ni_{48} compositions exhibit a ferromagnetic Curie temperature (T_c) within the austenite phase. Furthermore, as shown below, the magnetization can be fitted very well in terms of fixed local moments residing on the Mn ions.

The Curie-Weiss law,

$$M = \frac{N_A}{3k_B}\mu_{eff}^2 \frac{H}{T - T_c} \times n, \tag{5.5}$$

where $\mu_{eff} = g\mu_B\sqrt{J(J+1)}$, T_c is the Curie temperature and $g = 2$, was used to fit the high temperature magnetization curves in the paramagnetic region i.e. above T_c for Ni_{48} compositions. This fitting was obtained by assuming that densities of magnetic moments (n) is identical to the manganese ion density. For four compositions, the fittings yield J close to 2 as displayed in Table 5.1. The consistency of these results with a model corresponding to a local magnetic moment of $gJ\mu_B = 4\mu_B$ per Mn ion agrees with computed results [36, 124–126]. Therefore, it appears that

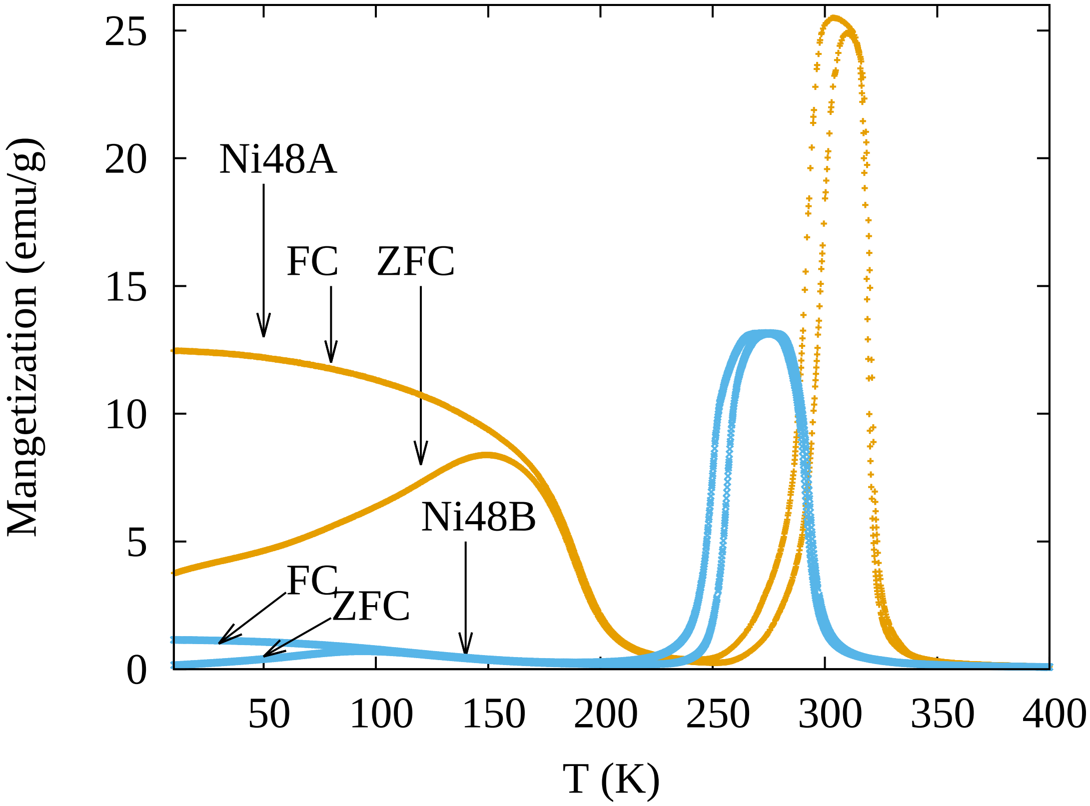

Figure 5.3: Temperature dependence of the magnetization for the Ni48 samples at 0.05 T and the error bars are smaller than the symbols. The data include results for both heating and cooling processes, as shown in the inset for the Ni50B sample. The low-T bifurcation corresponds to field-cooled (FC) and zero-field cooled (ZFC) as shown. Samples include Ni_{48} compositions, A=$Ni_{48}Mn_{35}In_{17}$, B=$Ni_{48}Mn_{38}In_{14}$.

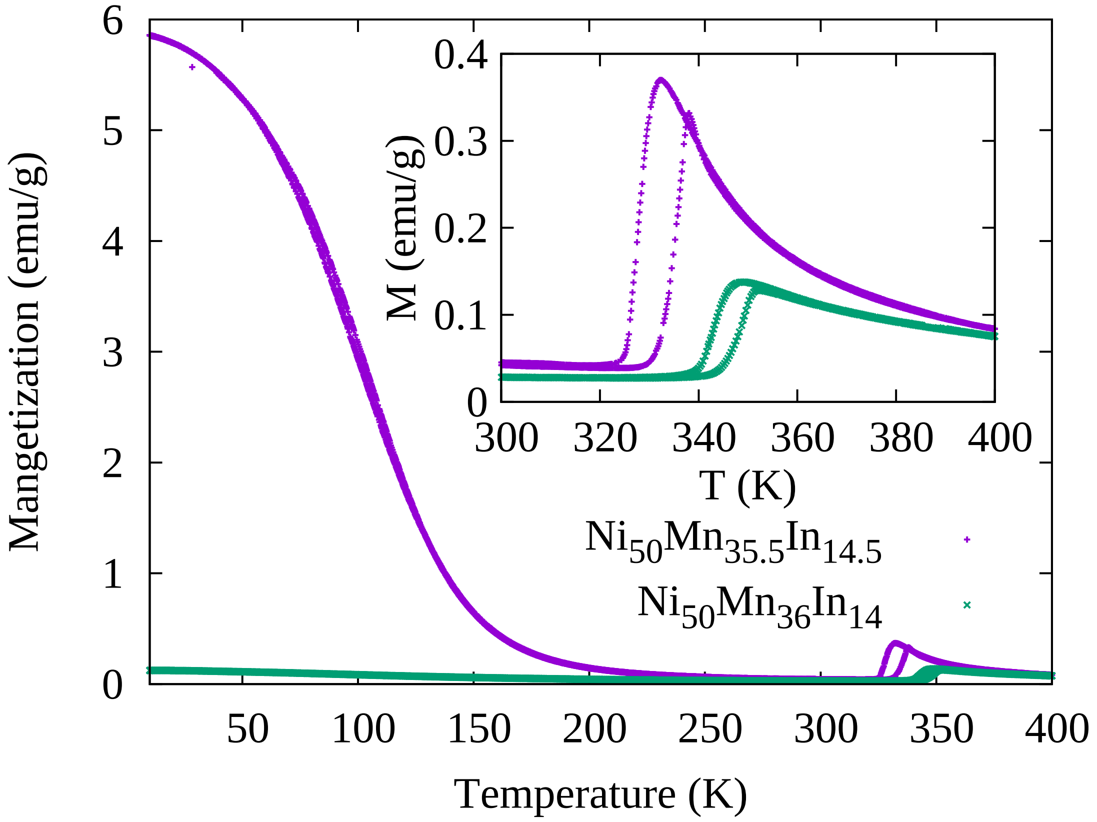

Figure 5.4: Temperature dependence of the magnetization for the Ni50 samples at 0.05 T and the error bars are smaller than the symbols. The data include results for both heating and cooling processes, as shown in the inset for the Ni50B sample. Samples include Ni_{50} compositions, A=$Ni_{50}Mn_{36}In_{14}$, B=$Ni_{50}Mn_{35.5}In_{14.5}$.

the moments can be treated as local moments which are indirectly coupled through RKKY interactions. Similar behavior has previously been identified in other X_2MnY Heusler systems [127, 128], and we show below that such a prescription also agrees with the specific heat results. Fitted T_c values are also given in Table 5.1. Notice that for the two Ni_{50} materials, the fitted T_c is lower than the martensite transition temperatures, which indicates that the austenite phase is paramagnetic while the two compositions Ni_{48} go into a ferromagnetic regime before becoming paramagnetic upon heating through a second order magnetic transition.

At low temperatures, the magnetization of each of the samples tends to saturate at a value lower than $4\mu_B$ per Mn, due to the antiferromagnetic behavior of the martensite phases. For the case of Ni50A, good agreement with the M vs. T curves above about 100 K (Fig. 5.5) was obtained by assuming a small fraction of the magnetic moments from small superparamagnetic clusters with the remainder corresponding to an antiferromagnetic matrix. Such a model has been used previously for Ni-Co-Mn-Sn Heusler alloys [129]. Since the Néel temperatures of our materials are high ($> 500°$C, as shown below), we can treat the antiferromagnetic susceptibility as nearly temperature-independent at these temperatures. Therefore, the martensite magnetization curves in different fields can be fitted by a combination of paramagnetic and antiferromagnetic contributions

$$M = NgJ'\mu_B B_{J'}\left(\frac{gJ'\mu_B H}{k_B T}\right) + \chi_{af}H, \tag{5.6}$$

where $B_{J'}$ is Brillouin function for the clusters with total spin J' and χ_{af} is the constant magnetic susceptibility due to antiferromagnetism. In this fitting (between 100 K and 300 K for all measurement fields), we obtained $J' = 26$, and a cluster density $N = 3.9 \times 10^{-5}$ mole/g. Assuming the clusters to be locally ferromagnetic with

nom. comp.	WDS comp.	label	J	$T_c(K)$	$T_{mh}(K)$	$\gamma(J/mole K^2)$	$\theta_D(K)$
$Ni_{50}Mn_{36}In_{14}$	$Ni_{49.54}Mn_{36.12}In_{14.34}$	Ni50A	2.002(4)	292±0.3	347	0.0124	315
$Ni_{50}Mn_{35.5}In_{14.5}$	$Ni_{49.88}Mn_{35.70}In_{14.42}$	Ni50B	1.992(2)	310±0.1	333	0.0128	318
$Ni_{48}Mn_{35}In_{17}$	$Ni_{49.53}Mn_{35.22}In_{15.22}$	Ni48A	2.003(4)	323±0.2	299	0.0117	316
$Ni_{48}Mn_{38}In_{14}$	$Ni_{47.22}Mn_{38.45}In_{14.33}$	Ni48B	1.998(1)	298±0.1	257	0.0163	316

Table 5.1: Table of the Ni-Mn-In compositions/notations and the corresponding analysis are listed. T_{mh} is defined as the maximum peak of the specific heat from the heating measurement.

fully-aligned Mn ions (individually with $J = 2$ consistent with the Curie-law fitting), this corresponds to 9.3% of the Mn atoms contained in the superparamagnetic clusters with the remaining Mn atoms contained in an antiferromagnetic (AF) matrix. Note that as is well established for an antiferromagnet with ordering temperature T_N, similar to Eq. 5.5, $M = (N_A n H \mu_{eff}^2/(6k_B T_N)$, within a molecular field model, while for a powder sample the magnetization will drop slowly to 2/3 of this value approaching $T = 0$. Equating the fitted susceptibility $\chi_{af} = 9.37 \times 10^{-6}$emu/g G to the value at T_N, and assuming the antiferromagnetic matrix to include 91% of the Mn ions as established in the fitting, we obtain $T_N = 610$ K, while renormalizing this value to the small decrease in χ_{af} in the fitted range gives $T_N \approx 500K$. As shown below, this extrapolated T_N is also consistent with the measured entropy of the AF phase.

At lower temperatures (Fig. 5.5) the departure of the Ni50A magnetization data from the fitted curves is likely due to super-spin glass behavior similar to what has been established in related alloys [129], possibly combined with blocking behavior due to anisotropy of individual clusters. In the Ni50A sample, a FC vs. ZFC bifurcation near 100 K was also observed as shown in Fig. 5.6. Similar behavior is seen more clearly for the Ni48B sample in Fig. 5.3.

The fitting procedure establishing superparamagnetic behavior in an AF matrix in Ni50A works particularly well for Ni50A sample since there is a large temperature region below T_m over which this behavior could be established. However, in Ni48B the amplitude of the low-temperature M-T curves vs. field (Fig. 5.9) also corresponds to approximately 10% of the Mn moment in superparamagnetic clusters. Ni50B exhibits a larger magnetic response at low temperatures which we have not fully characterized, while in Ni48A a series of Arrott plots with the standard critical exponents (Fig. 5.7) confirm that the enhanced low-temperature magnetization

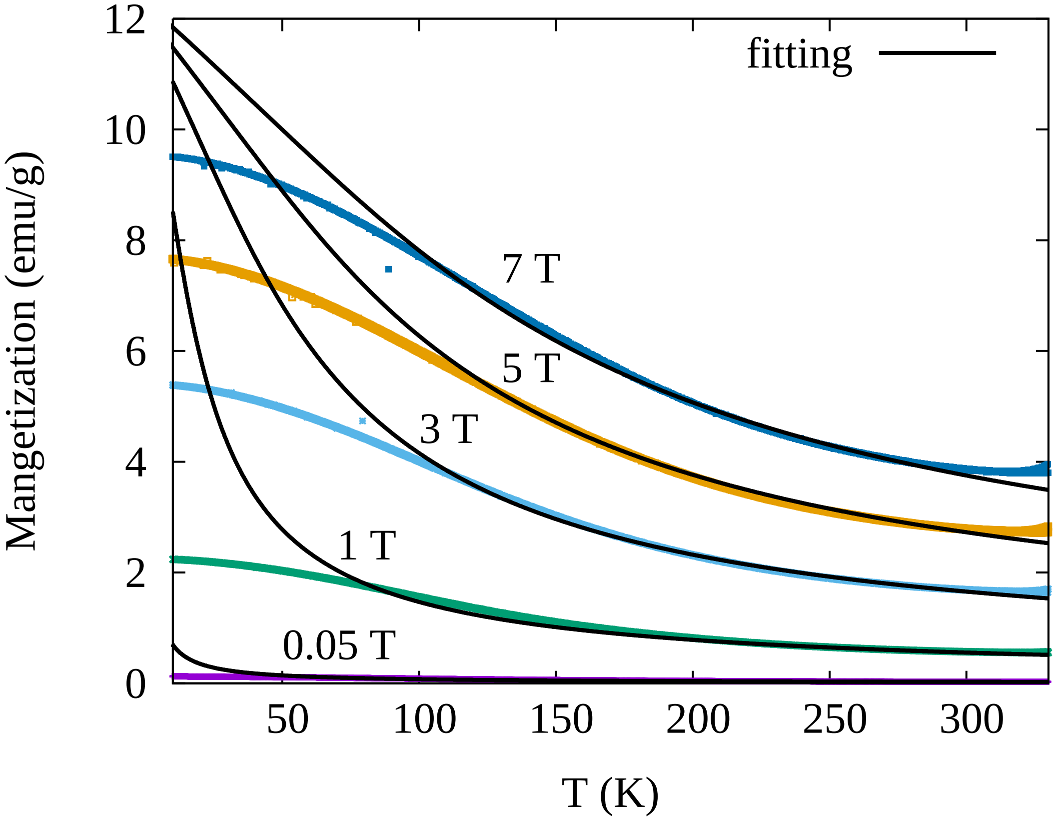

Figure 5.5: Temperature dependence of the magnetization for the martensite of Ni50A sample ($Ni_{50}Mn_{36}In_{14}$) at B=0.05, 1, 3, 5, 7 T and the error bars are smaller than the symbols. The black line is the fitting from the combination of paramagnetic and antiferromagnetic model.

corresponds to the development of a spontaneous moment due to spin canting at a critical temperature of 194 K, with an AF (or other zero moment) phase above it. This matches a previous report [36] for a low-temperature ferromagnetic transition in nearly identical compositions However, our result shows that this is not ferrimagnetic but a canted or similar phase.

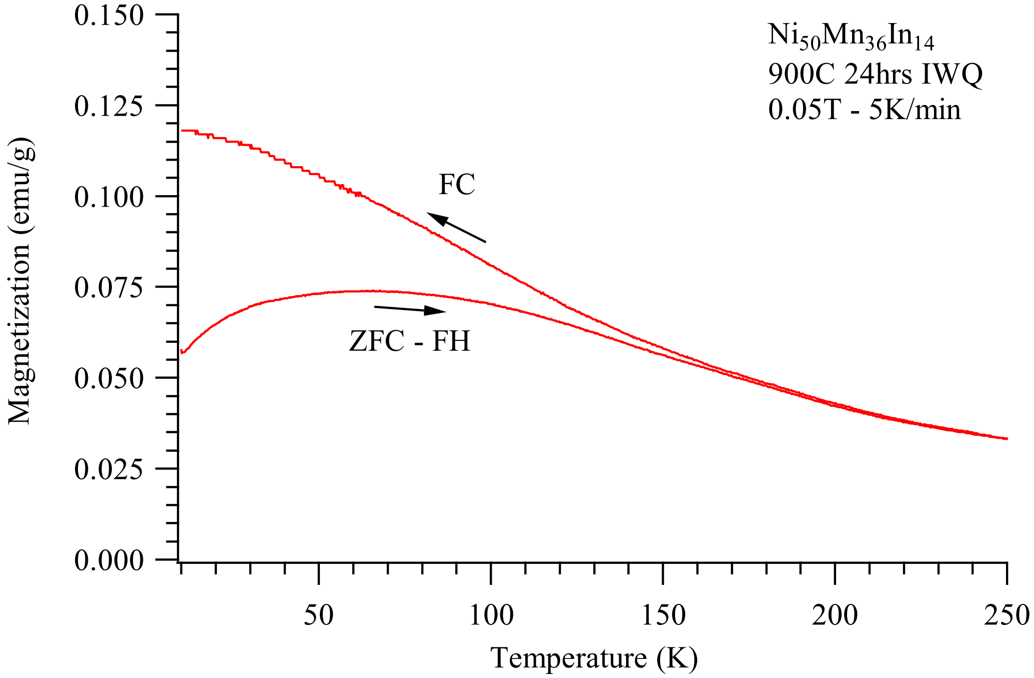

Figure 5.6: ZFC and FC magnetization curves for the Ni50A sample are shown in 0.05 T and the error bars are smaller than the symbols.

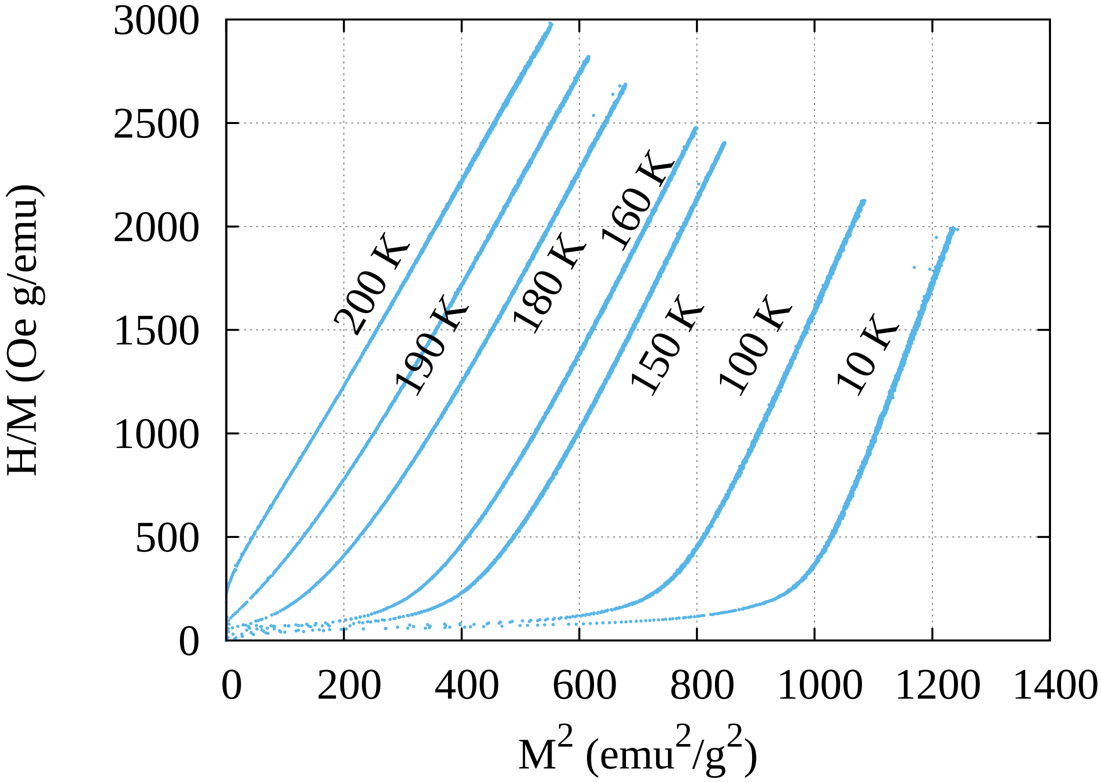

Figure 5.7: Arrott plots with the standard critical exponents for $Ni_{48}Mn_{35}In_{17}$ (Ni48A sample) obtained from the isothermal $M-H$ magnetization and the error bars are smaller than the symbols. $M-H$ measurements are done in 10 K, 100 K, 150 K, 160 K, 180 K, 190 K and 200 K (from right to left).

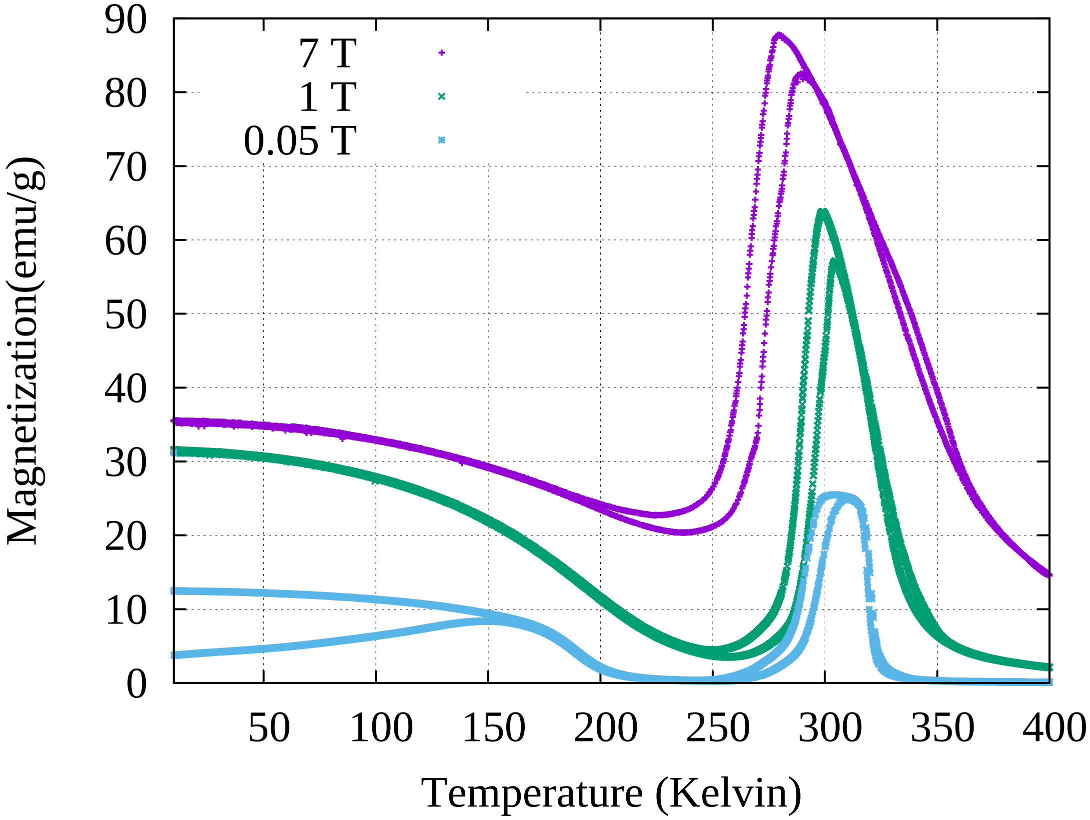

Figure 5.8: Temperature dependence of the magnetization for $Ni_{48}Mn_{35}In_{17}$ (Ni48A sample) at B=0.05, 1, 7 T and the error bars are smaller than the symbols.

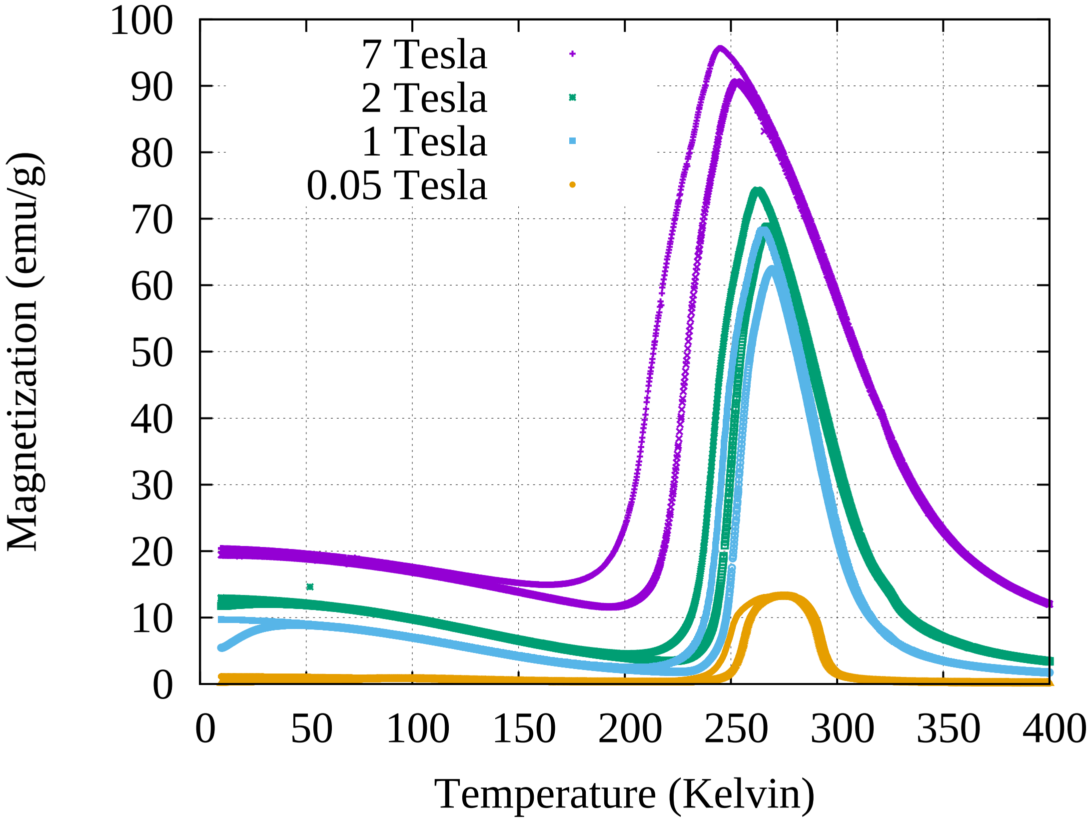

Figure 5.9: Temperature dependence of the magnetization for $Ni_{48}Mn_{38}In_{14}$ (Ni48B sample) at B=0.05, 1, 2, 7 T and the error bars are smaller than the symbols.

5.5 Specific Heat Analysis

In this section, I will give a detailed analysis about the specific heat measurements on the Ni-Mn-In samples. For $Ni_{50}Mn_{36}In_{14}$ sample, the 2-τ method and our method give consistent results as shown in Fig. 5.10 in the non-hysteretic regime. The open circles in Fig. 5.10 are analyzed by the 2-τ model and these results can not reflect the specific heat across the 1st order transition correctly. The method developed in Sec. 3.5.3 allows us to do a point-by-point analysis after scanning a long heat pulse across the transition. The post-process results are shown as the dense curves in the Fig. 5.10. The excellent agreement also was observed in the specific heat results for the other samples Ni48A, Ni48B, Ni50A and Ni50B (as shown below).

Having confirmed the accuracy of this modified analysis method, I will now discuss the decomposition of the individual specific heat contributions for these samples. The total specific heat for this system should be described by the three main contributions which are the electronic, vibrational and magnetic:

$$C_{total} = C_{el} + C_{vib} + C_{mag}. \tag{5.7}$$

This follows from the similar decomposition of the entropy as discussed in chapter 4. The electronic specific heat contribution can be described by the known formula [130]

$$C_{el}(T) = \left(\frac{\pi^2}{3}\right) k_B^2 D(E_F) T \equiv \gamma T, \tag{5.8}$$

where $D(E_F)$ is the density of states at Fermi energy. Thus this term is a linear function of the temperature. The vibrational contribution [130, 131] based on the Debye model is

$$C_{vib}(T) = 9k_B \left(\frac{T}{\theta_D}\right)^3 \int_0^{\theta_D/T} \frac{x^4 e^x}{(e^x - 1)^2} dx \tag{5.9}$$

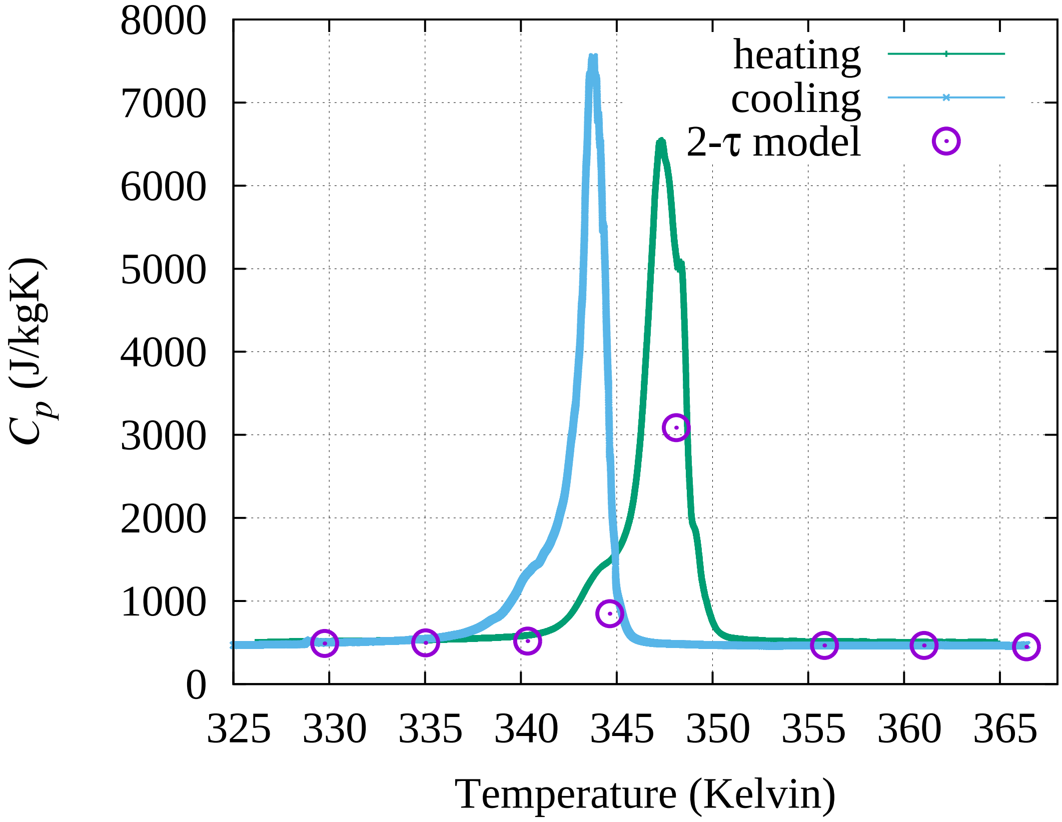

Figure 5.10: The post-process method (densely plotted small symbols) vs. 2-τ model (open rectangles) for $\mathrm{Ni}_{50}\mathrm{Mn}_{36}\mathrm{In}_{14}$ (Ni50A) and the error bars are smaller than the symbols. These two data sets agree very well outside of the regime where the 1st order transition happens [59].

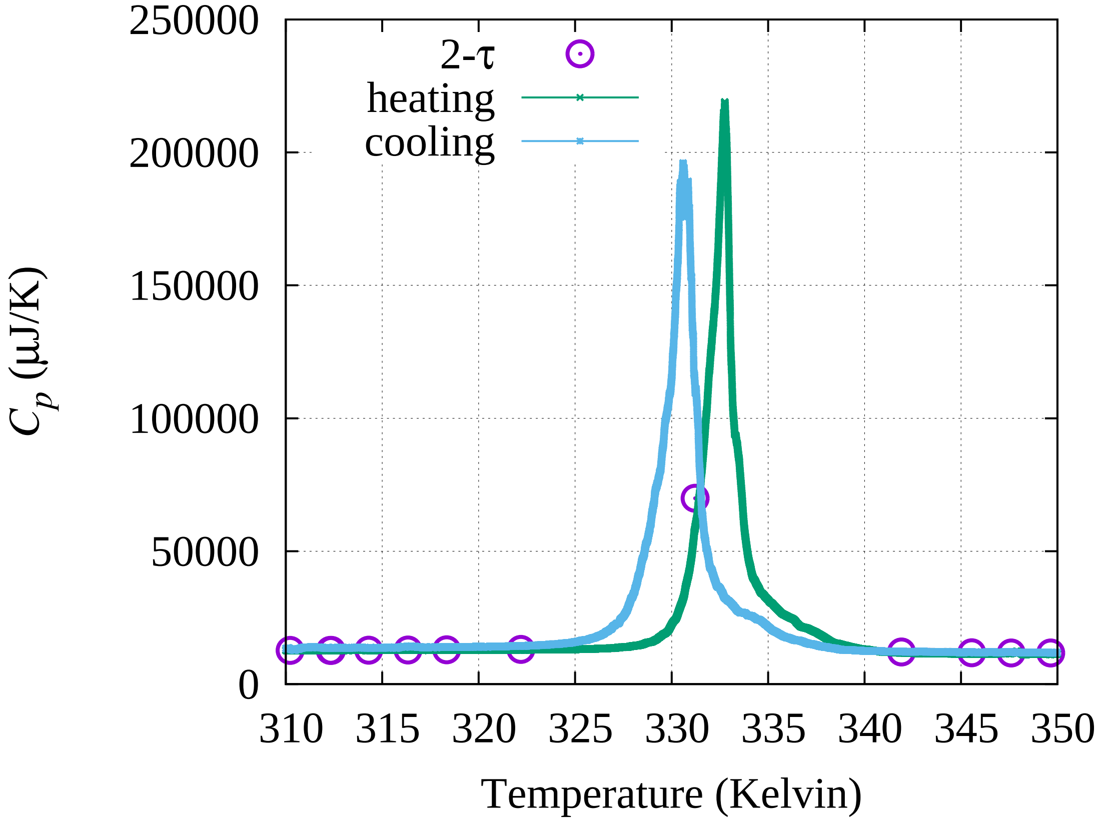

Figure 5.11: The post-process method (densely plotted small symbols) vs. 2-τ model (open circles) for $Ni_{50}Mn_{35.5}In_{14.5}$ (Ni50B) and the error bars are smaller than the symbols. These two data sets agree very well outside of the regime where the 1st order transition happens.

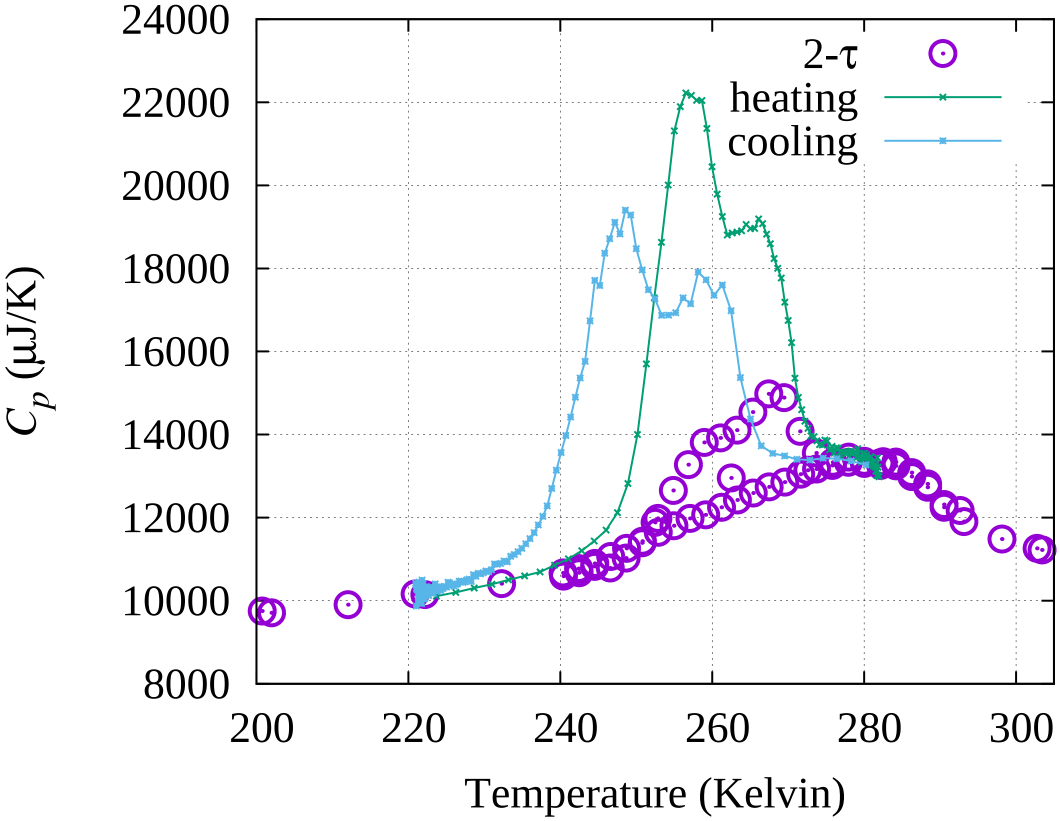

Figure 5.12: The post-process method (small symbols) vs. 2-τ model (open circles) for $Ni_{48}Mn_{38}In_{14}$ (Ni48B) and the error bars are smaller than the symbols. These two data agree very well outside of the regime where the 1st order transition happens.

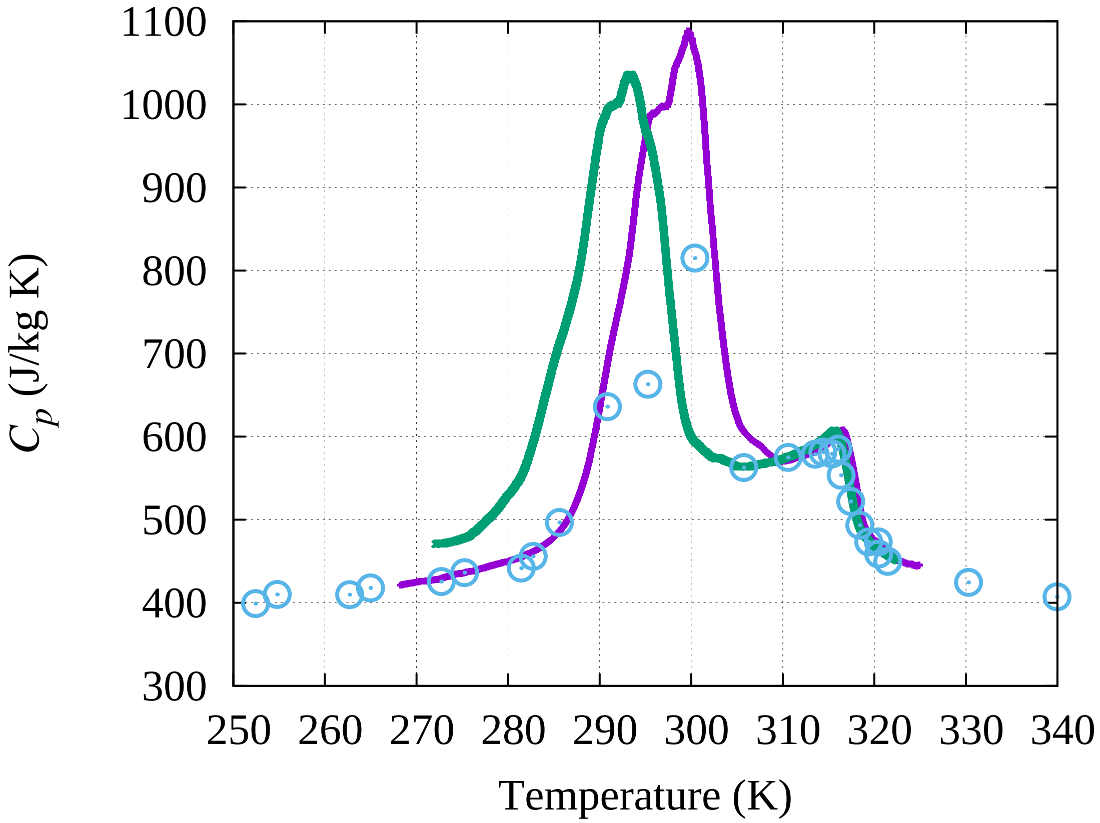

Figure 5.13: The post-process method (small symbols) vs. 2-τ model (open circles) for $Ni_{48}Mn_{35}In_{17}$ (Ni48A) and and the error bars are smaller than the symbols. These two data agree very well outside of the regime where the 1st order transition happens. Note that the low-temperature end of cooling curve appears to be higher than it should be, which is believed due to the heating of the sample stage after the long heat pulse.

where θ_D is the constant Debye temperature. Since the electronic and vibrational contributions dominate outside of the transition regime and the mathematical formulae are well-defined, I will analyze these two contribution first. The electronic contribution acts as a linear function as temperature at low temperature while the Debye model behaves as T^3 so we can write done the specific heat behavior as

$$\frac{C_{total}}{T} = \gamma + \beta T^2. \tag{5.10}$$

The applicability of the Debye model was discussed in chapter 4, however note that the T^3 behavior in the $T \to 0$ limit is exact and model independent for a harmonic network. Therefore, the electronic contribution can be obtained from the intercept of a plot of C/T vs. T^2 as shown in Fig. 5.15 for the four Ni-Mn-In samples. The γ results are listed in Table 5.1 and discussed below. We also found that in $Ni_{50}Mn_{36}In_{14}$ (Ni50A) $\gamma = 0.0124$ J/mole K^2 is independent of the external magnetic field up to 2 T (shown in the inset of Fig. 5.14). Note that these values are per mole formula unit, considering the 4-atom (A_2BC) formula unit of the parent Heusler structure.

In order to gain a systematic understanding of the entropy, we performed calorimetric measurements from 1.8 K to 400 K for all four samples. The low temperature part (< 10 K) has been shown in Fig. 5.15. Fig. 5.16 shows our heating curve specific heat results (martensite→austenite) for the four Ni-Mn-In samples over the full range. The martensitic transition temperatures and Curie temperatures seen in the specific heat results are consistent with the magnetic measurements shown in Fig. 5.3 and Fig. 5.4. Also we indeed cannot observe the Curie temperatures for the two Ni_{50} samples since they are found to be lower than the martensitic transformation temperatures ($T_{mh}/T_c > 1$), as shown above. Since $T_{mh}/T_c < 1$ for other two samples,

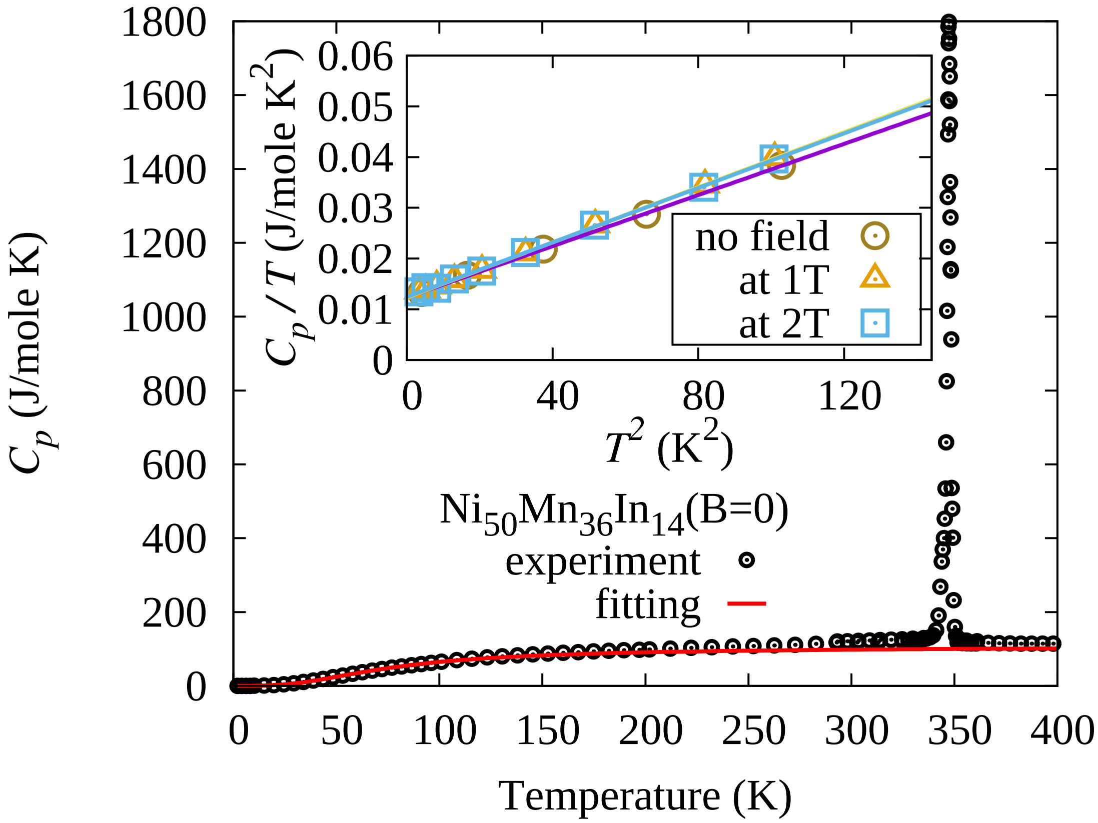

Figure 5.14: Experimental specific heat and analysis for $Ni_{50}Mn_{36}In_{14}$ (Ni50A) and the error bars are smaller than the symbols. The solid curve is the simulation according to an electronic and Debye contribution with $\gamma = 0.0124$J/mole K^2 and $\theta_D = 315$ K respectively. The low temperature measurements (< 10 K) in the inset shows the experimental data (dots) and fitting (solid line) in 0, 1, 2 Tesla. γ is found to be field independent.

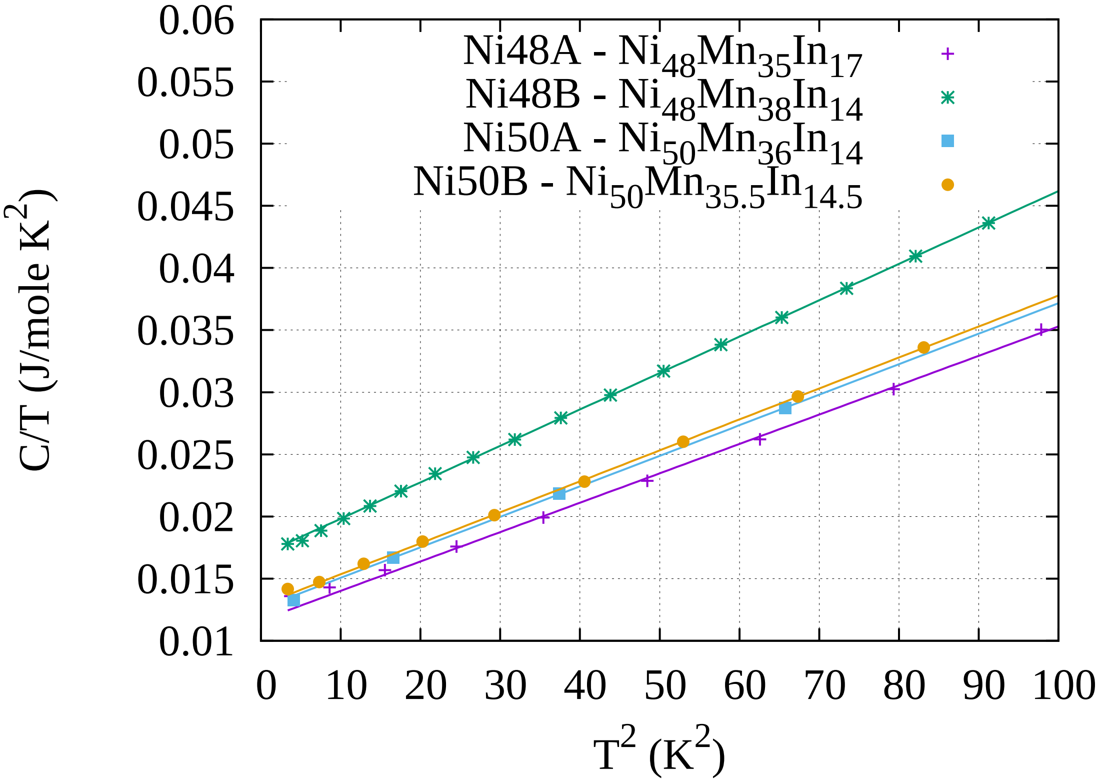

Figure 5.15: C/T vs. T is shown for four samples. Solid curves are straight line fits. The intercepts on the y-axis represent the γ values due to conduction electrons.

they go to a paramagnetic austenite phase through a second order ferromagnetic phase transition and the Curie temperature can be clearly observed in the specific heat measurements as shown in Fig. 5.16.

We did a least χ^2 fitting in the low temperature regime (< 10K) for each sample yielding $\gamma = 0.0117$ J/mole K^2 to $\gamma = 0.0163$ J/mole K^2, as shown in Table 5.1 as discussed above. With γ obtained from the low temperature fittings, the Debye model was applied in least χ^2 fittings to around 100 K for each sample. The fitted Debye temperatures range from 314 K to 318 K (shown in Table 5.1). With these parameters, we extended the specific heat by extrapolating this model to 400 K and obtained the solid curve shown for the case of Ni50A in Fig. 5.16. The parameters for the different samples are very close to each other, as a results of which the curves for different samples cannot be distinguished in the figure, and therefore we only drew the representative results for Ni50A.

In this chapter, we concentrated on the contributions obtained from sample heating. However, in limited tests we found that the cooling curves (shown in the beginning of this chapter) gives similar results as what was observed in heating curves. For further analysis discussed below, we used exclusively the results from the heating curves.

5.6 Entropy Analysis

In the previous section, I described the specific contributions from experiments based on four Ni-Mn-In compositions. In this section, I will further dig into the specific heat contribution vs. varying composition. As compositions vary, the first order transformations change from corresponding to antiferromagnetic to ferromagnetic in some compositions and antiferromagnetic to paramagnetic in others, as shown in the last section. In Fig. 5.16, the heating curve specific heat results were shown. The

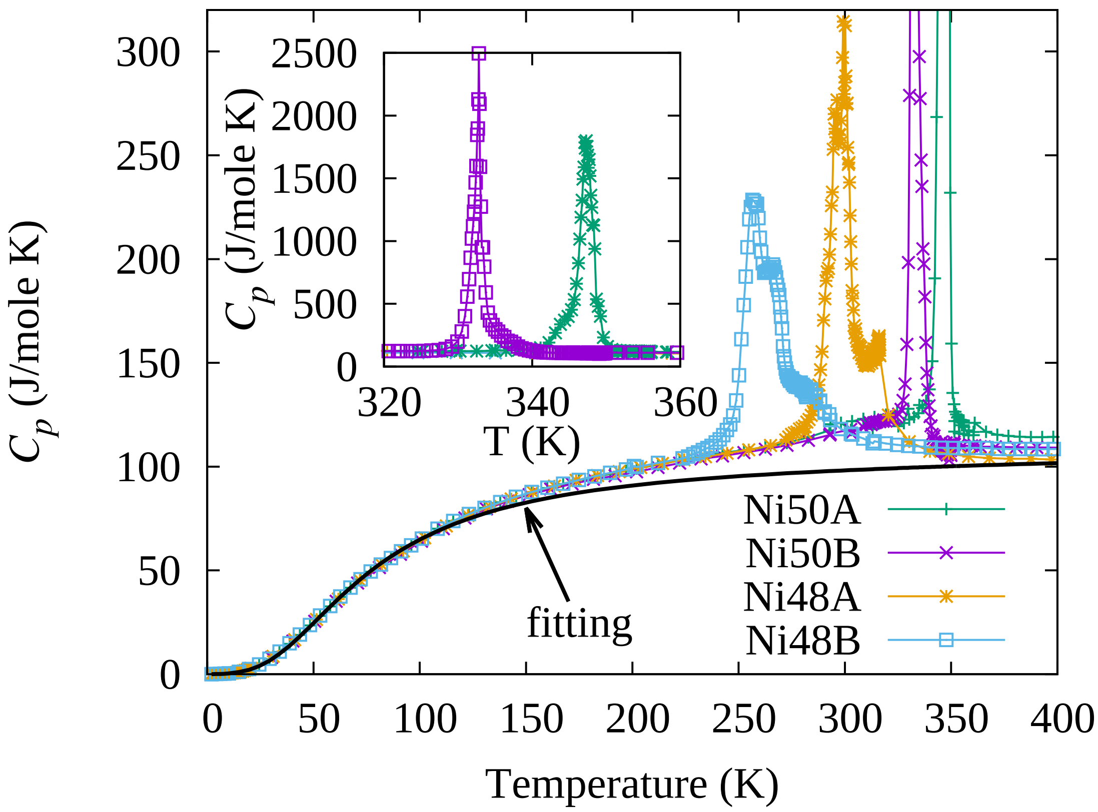

Figure 5.16: Temperature dependence of the specific heat for the Ni-Mn-In samples without applied fields and the error bars are smaller than the symbols. The fitting curve is for Ni50A samples from a Debye model plus electronic contribution as described in text.

two materials with compositions labeled Ni_{48} can be seen to have well-known contributions due to their second order magnetic transitions while the other two materials with higher Ni compositions show only the structural changes, with much sharper specific heat response.

The heating curve specific heat results for these materials turn out to be very close to each other below the martensitic transitions, and their vibrational and electronic contributions are quite similar to each other, as is apparent from the fitted values (Table 5.1) and also as seen in Fig. 5.16. As discussed in chapter 4, the magnetic entropy can be obtained from the equation

$$S_{mag} = \int \frac{C_{mag}}{T} dT = \int \frac{C_{total} - C_{vib} - C_{el}}{T} dT \leq R \ln(2J+1) \times N. \qquad (5.11)$$

The last inequality expresses the well-known limit for the magnetic entropy [115]. The magnetic moment concentration N is well-established in our samples since as shown above the results in all cases are consistent with Mn treated as local moments with $J = 2$. By extending the Debye and electronic contributions identified at low temperatures through the transition, we can identify deviations from this limit. The entropy difference, S_{excess}, plotted in Fig. 5.17, represents the integrated difference of Eq. 5.11 for each sample. These excess contributions are expected to be equal to S_{mag} if the fitted S_{el} and S_{vib} correctly account for the other contributions.

The Ni_{48} excess entropy contributions for both samples appear to be close to the classical magnetic entropy as shown in Fig. 5.17. These curves were obtained by subtracting the fitting parameters in Table 5.1 from the experimental heating curve specific heat as Eq. 5.11 and then dividing by their corresponding Mn densities. As shown before the Ni_{50} compositions have $T_{mh}/T_c > 1$ so that the second order transitions completely disappear and these materials transform to a paramagnetic

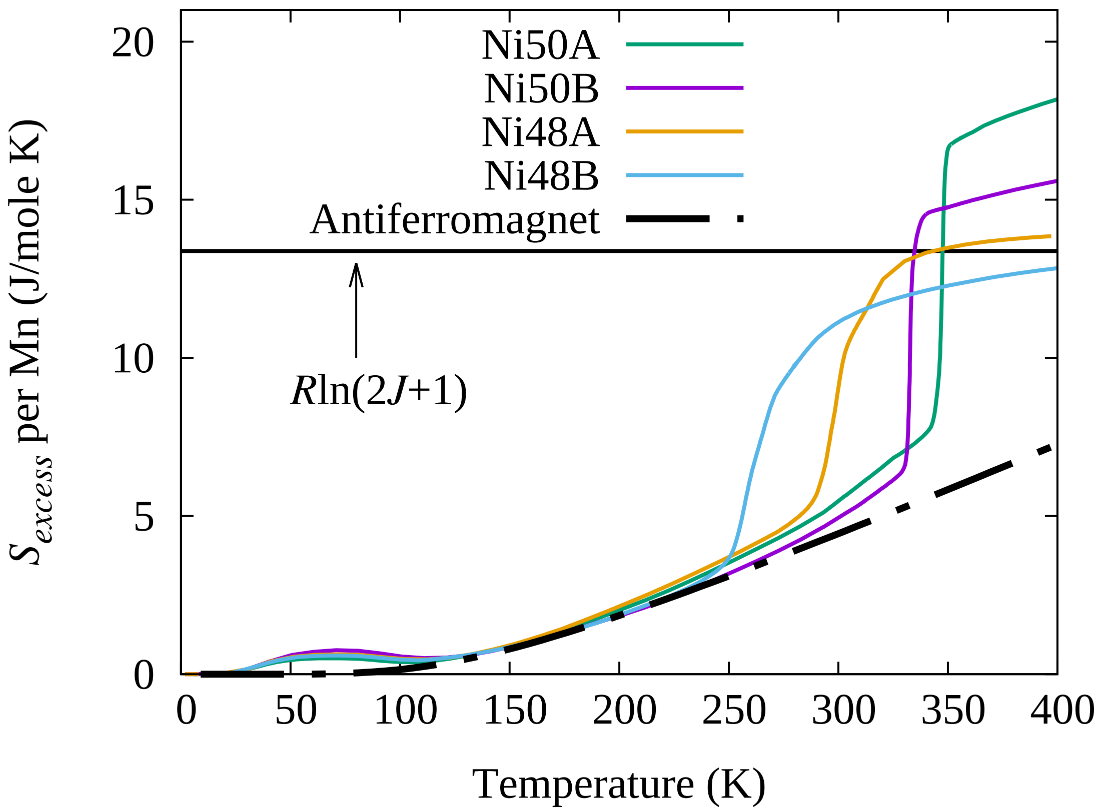

Figure 5.17: The magnetic entropy for the Ni-Mn-In samples, per mole of Mn. The solid curve represents the analysis as described in the text. The dashed curve is the antiferromagnetic curve obtained for $T_N = 540$ and $J = 2$. The horizontal line is the magnetic entropy limit for $J = 2$.

phase directly from the martensite phase, so that only one sharp transformation is apparent in $\Delta_S excess$.

A calculated antiferromagnetic contribution with $J = 2$ and $T_N \approx 540$ (shown as the dashed line in Fig. 5.17) fits all of the excess entropy curves qualitatively very well below the martensitic transition for all the samples. The antiferromagnetic analysis comes from a mean-field model, and is a numerical solution of the relationship described in Sec. 2.3 (and see Fig. 2.1) for which J and T_N are the only parameters. It is interesting that these materials all appear to have nearly identical magnetic interactions judging from the entropy results in this region, although this magnetic behaviors are rather different. For example the apparent spin-canting transition in Ni48A sample can not be observed here, indicating that this transitions has little effect on the magnetic entropy.

Above the martensitic transition, the entropy for the Ni_{50} samples surprisingly goes beyond the magnetic entropy limit while the Ni_{48} samples have entropy which agrees well with the magnetic limit for $J = 2$. This is the first time in the literature as far as we are aware of for a direct observation of the excess total entropy from calorimetric measurements.

The electronic entropy change as represented by a γ difference between the martensite and austenite phases is believed to be much smaller than the entropy change due to lattice vibrations related to the structural deformations. If we attribute all of the observed excess entropy change to an electronic contribution, this requires the γ change to be 14 mJ/mole K^2 in $Ni_{50}Mn_{36}In_{14}$, which means a doubling of the martensite γ. This appears to be too large to be possible. A change of 5 mJ/mole K^2 is required in $Ni_{50}Mn_{35.5}In_{14.5}$, which appears to be more conceivably correct. One recent experimental estimation [96] already addressed a significant lattice entropy contribution ($\approx$ 50%) in Ni-Mn-In with a composition different from ours. Also, a measurement at high magnetic fields in Ni-Co-Mn-In [88] found that the electronic contributions are relatively small (4 mJ/mole K^2) compared to the vibrational contribution. We also recently worked with James Monroe, from our collaborator I. Karaman's group [132] in preliminary studies of a NiCoMnIn material for which heat treatments can favor either the austenite or martensite structure at low temperatures. In this case also, we found only a small difference in γ of 1.8 mJ/mole K (a 13% difference). Based on these results we can not completely rule out the possibility of a γ change of 5 mJ/mole K^2 in $Ni_{50}Mn_{35.5}In_{14.5}$, or a partial contribution to the entropy change across the martensitic transition in $Ni_{50}Mn_{36}In_{14}$ being due to γ change, however the vibrational contribution is expected to be most important.

Aside from the references mentioned above, it has also been inferred in previous studies on other Hesuler alloys [133–135] that the electronic contribution (typically $\gamma = 5 - 10$ mJ K/mole) is negligible compared with the vibrational contributions. Also see reference [55] where giant MCE materials are summarized for additional discussion.

Here, if we attribute therefore the entire additional entropy change to vibrational contributions, the Debye temperature would be required to decrease from 315 K to 300 K in $Ni_{50}Mn_{36}In_{14}$ and from 318 K to 312 K in $Ni_{50}Mn_{35.5}In_{14.5}$. This comes from the entropy analysis in the Debye model presented in Sec. 4.1. It seems very likely that these contributions make up all or most of the excess giant MCE entropy in these materials. For a magneto-elastic coupled system, the lattice entropy can be connected to the magnetic subsystem through the dependence of the Debye temperature θ_D on the deformation [85, 136]

$$\theta = \theta_D \left(1 - \eta \frac{\Delta V}{V_0}\right), \tag{5.12}$$

where θ_D, η and $\frac{\Delta V}{V_0}$ are the Debye temperature in absence of lattice deformation, the Grüneisen constant and the volume change. This relationship has been used in a number of recent cases [85, 96, 136, 137] to estimate the entropy change starting from measured changes in lattice parameters, although a significant limitation is that the Grüneisen constant is not always well established. Usually, η is between 1 and 3 [65]. A first-principles calculation found that η is 2.405 for a Ni-Mn-Sb Heusler alloy [138] and we can adopt the same value in making an estimation for the present materials. This yields $\frac{\Delta V}{V_0}$ 2.0% based on our results for $Ni_{50}Mn_{36}In_{14}$ and 0.78% for $Ni_{50}Mn_{35.5}In_{14.5}$. As follow-up work to this dissertation, we hope to obtain temperature dependent synchrotron X-ray diffraction data to determine these values in the near future in order to further understand the relationship of entropy changes to changes in crystal structure for these materials.

5.7 Summary

In summary, a giant magneto-elastic coupling modified by changing chemical composition has been observed in Ni-Mn-In Heusler alloys. For $Ni_{48}Mn_{38}In_{14}$ and $Ni_{48}Mn_{35}In_{17}$ $T_{mh}/T_c < 1$, and the samples go to paramagnetic austenite state through a second order ferromagnetic phase transition, so that the Curie temperature can be clearly observed in specific heat measurements. For $Ni_{50}Mn_{36}In_{14}$ and $Ni_{50}Mn_{35.5}In_{14.5}$ materials $T_{mh}/T_c > 1$, so that the second order transitions completely disappears and the materials transformed paramagnetic state directly.

In the martensite phase, these samples were found to agree with a model in which the martensite is antiferromagnetic with a small portion of superparamagnetic clusters. The portion of superpagmanetic moments is small and contributes relatively minor amount to the specific heat results. As the temperature increases to the austenite phase region through first-order transitions, the materials were shown to be ferromagnetic with J close to 2 or else paramagnetic with ferromagnetic fluctuations, with the magnetic properties attributed to solely to a local moment of Mn atoms. The specific heat due to antiferromagnetism was modeled by molecular field theory and with T_N between 500 K and 600 K the resulting curves were found to give a qualitatively good agreement for all samples. In addition, by subtracting the well-established electronic and phonon contributions, the magnetic contributions and other excess contributions were evaluated. In the materials with $T_{mh}/T_c > 1$, an additional entropy contribution attributed to structural deformations was observed by comparing the analysis with the magnetic limit $R\ln(2J+1)$. This is the first time in the literature as far as we are aware of for a direct observation of the excess entropy from calorimetric measurements.

6. RELATIVE COOLING POWER IN PARAMAGNETIC MAGNETOCALORIC SYSTEMS

6.1 Motivation

One of the common physical quantities used to characterize MCE materials is the isothermal entropy change upon variation of the external magnetic field. We have explored this quantity using two methods, through the integration of specific-heat data, and also by indirect methods [56], based on magnetization measurements. This allows the examination of entropy contributions competing with magnetism as has already been discussed in the last chapter. However, care must be exercised in measuring both the specific heat and magnetization within the coexistence phase region due to the first-order martensitic transition. In addition, since the first order transformation is by nature hysteretic, the question remains as to how well relationships for the magnetization derived from equilibrium thermodynamics capture correctly the actual transformation entropy.

As further comparison of the MCE by these methods, we examine the relative cooling power (RCP) [139] which represents the amount of transferred heat between the hot and cold reservoirs under a magnetic refrigeration cycle [140]. Values extracted from direct and indirect methods provide a compelling demonstration that the corresponding entropies are in very close agreement. The RCPs for the two investigated materials are smaller than comparable materials operating at lower temperatures, which we show results from the separation between the austenite Curie temperature (T_c) and the operating temperature. However, further analysis shows that a significant RCP would be achievable in such systems by suitable tuning of structural and magnetic transition temperatures.

6.2 Sample Preparations

Bulk polycrystalline $Ni_{50}Mn_{36}In_{14}$ and $Ni_{50}Mn_{35.5}In_{14.5}$ (nom. at. %) alloys are studied in this chapter. These two samples are identical to two of the four samples which have been discussed in the previous chapter (Ni50A and Ni50B respectively). The readers are referred to Sec. 5.3 for the sample preparation and Table 5.1 for their common properties.

6.3 Magnetization Analysis

Iso-field magnetization measurements were carried out using a Quantum Design Magnetic Property Measurement System. Fig. 6.1 and Fig. 6.2 show the magnetization measurement results at different fields. The transition curves as shown in Fig. 6.1 and Fig. 6.2 correspond to the well-known martensitic transformation. The results indicate a transition from a paramagnetic austenite to an anti-ferromagnetic (or similar low-moment) martensite upon cooling. These magnetic properties have already been discussed in detail in the last chapter. The forward (austenite to martensite) transformation is observed on cooling the samples and the reverse transformation (martensite to austenite) is observed on sample heating. Outside of the transformation hysteresis region, the transition is nominally complete. As shown in Fig. 6.1 and Fig. 6.2, the transition temperatures slightly shift to lower temperatures as the field increases.

Comparing these two samples, $Ni_{50}Mn_{35.5}In_{14.5}$ (Ni50B) has a slightly lower martensitic transition temperature as shown in Fig. 6.3 measured at 0.05 T. The martensitic transition temperature also shifts to lower temperature as the field increases as shown before.

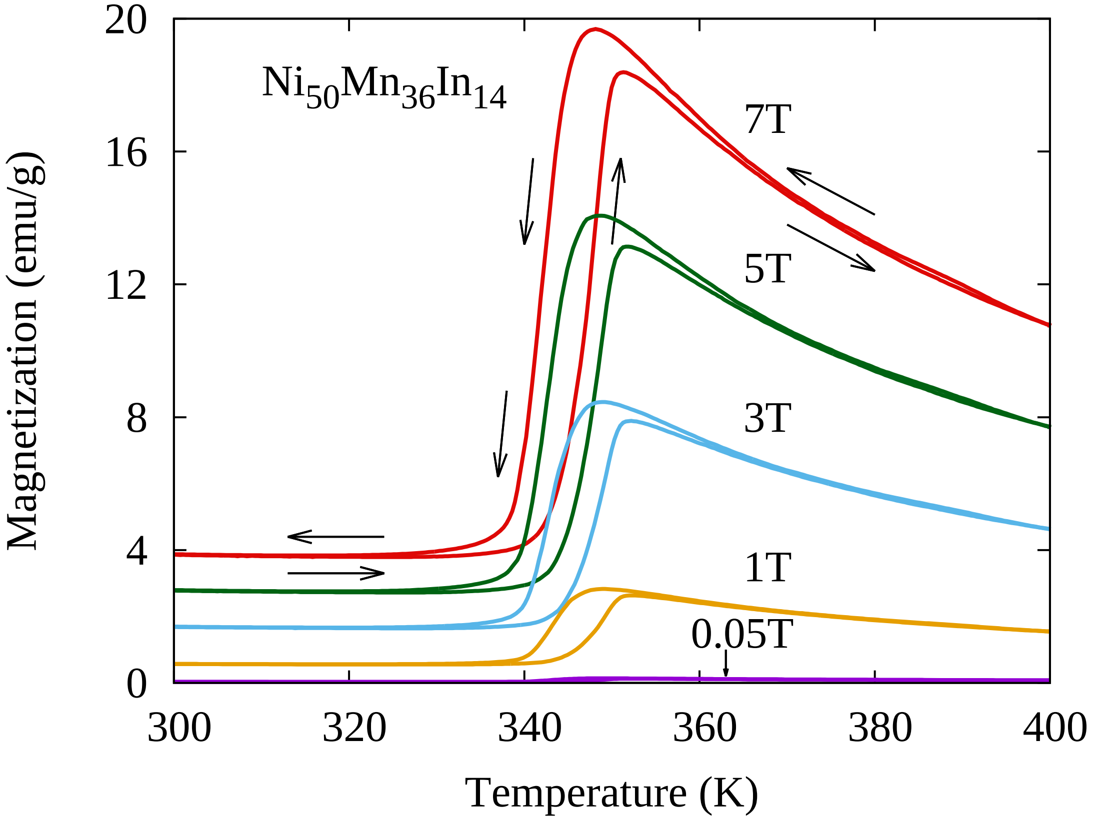

Figure 6.1: Temperature dependence of the magnetization for the $Ni_{50}Mn_{36}In_{14}$ (Ni50A) sample in different fields (0.05, 1, 3, 5 and 7 T as shown) and the error bars are smaller than the symbols.

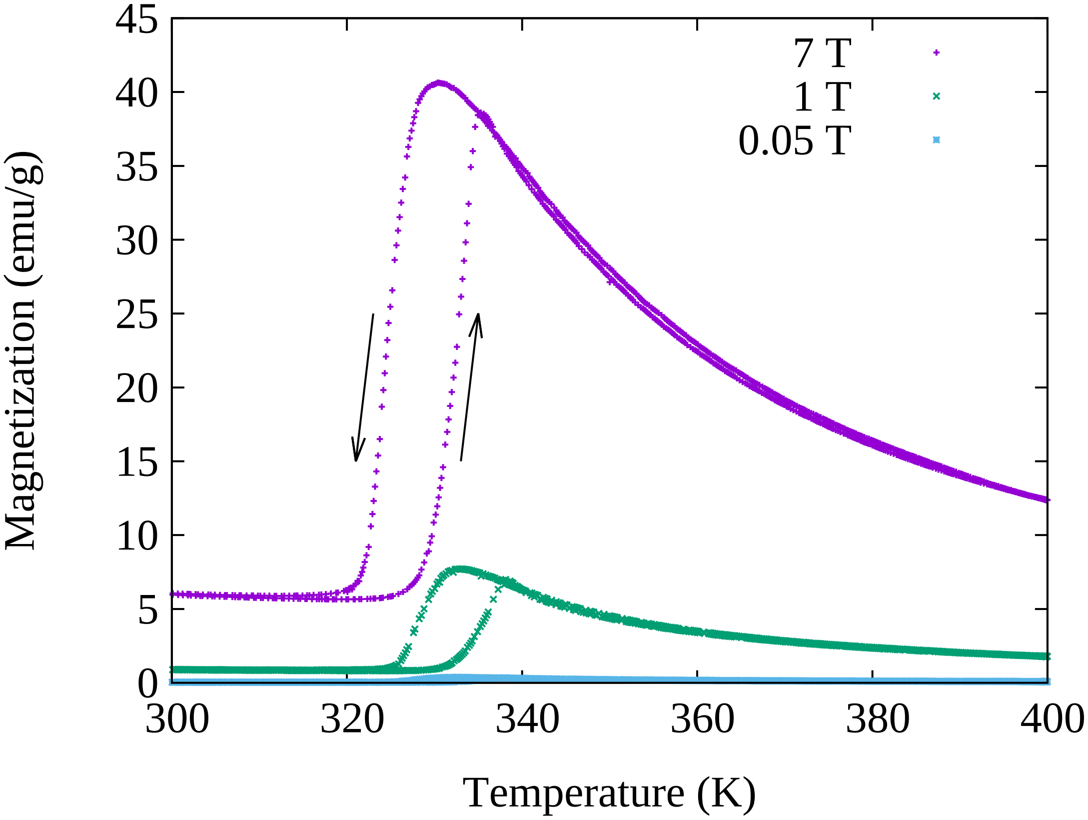

Figure 6.2: Temperature dependence of the magnetization for the $Ni_{50}Mn_{35.5}In_{14.5}$ (Ni50B) sample in different fields (0.05, 1, and 7 T as shown) and the error bars are smaller than the symbols.

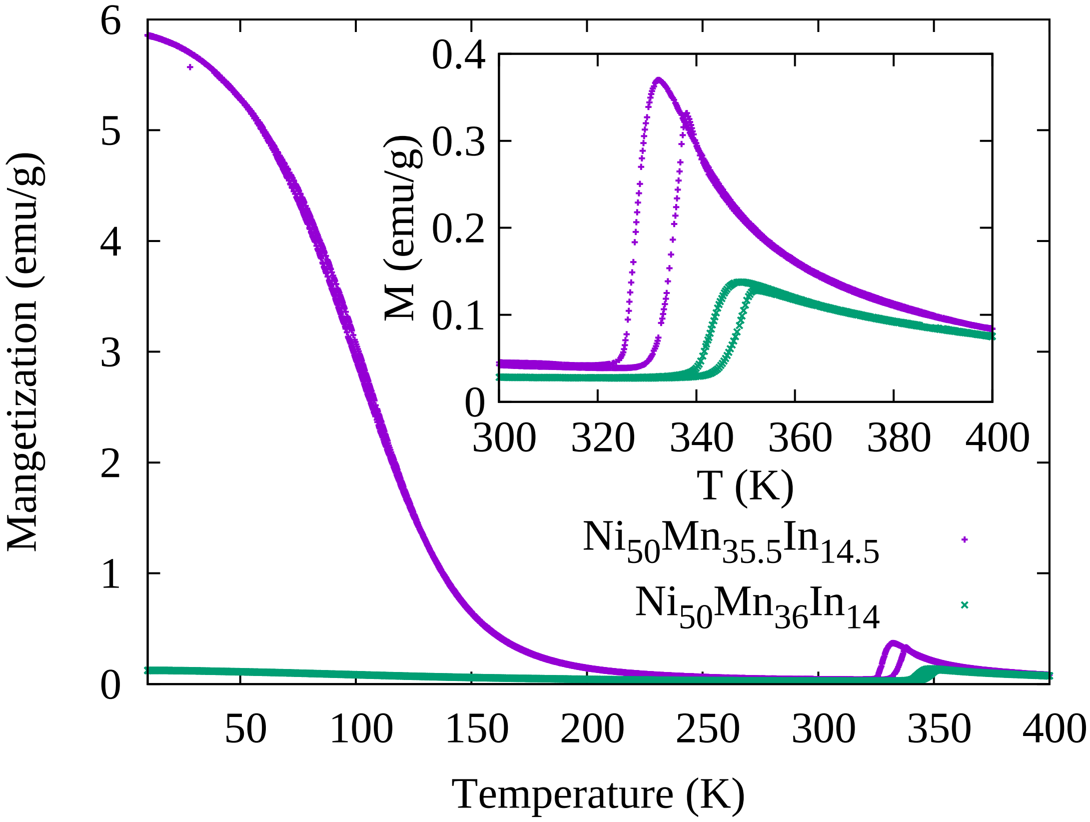

Figure 6.3: Temperature dependence of the magnetization comparison between $Ni_{50}Mn_{36}In_{14}$ (Ni50A) and $Ni_{50}Mn_{35.5}In_{14.5}$ (Ni50B) samples in 0.05 T and the error bars are smaller than the symbols. $Ni_{50}Mn_{35.5}In_{14.5}$ (Ni50B) has a relatively lower martensitic transition temperature.

The Curie-Weiss law,

$$M = \frac{N_A}{3k_B}\mu_{eff}^2\frac{H}{T - T_c} \times n, \tag{6.1}$$

where $\mu_{eff} = g\mu_B\sqrt{J(J+1)}$, T_c is the Curie temperature and $g = 2$, was used to fit the austensite magnetization curves of the two samples. Fitting $Ni_{50}Mn_{36}In_{14}$ (Ni50A) yielded $T_c = 292K$ and $J = 2.00$ per Mn while $Ni_{50}Mn_{35.5}In_{14.5}$ (Ni50B) yielded $T_c = 310K$ and $J = 1.99$. These values are slightly different from the results published in reference [59] because the fitting temperature range is different. However, this does not make any difference for the physical results we discuss in this thesis. This fitted spin value was obtained by assuming that the density of magnetic moments is identical to the manganese ion density n (from WDS). The fitted curves for $Ni_{50}Mn_{36}In_{14}$ (Ni50A) are shown in the inset of Fig. 6.4 for two of these fields. The linearity of these curves in M and T demonstrates the paramagnetism of the austenite phase. These results with a local magnetic moment of $4\mu_B$ agree with reported studies [36, 124–126] and are consistent with magnetic moments in the sample attributed to manganese with at most a very small moment on other atoms. Note that the Curie temperature apparent here is very similar to $T_c \approx 293$ K reported to be observed in a sample of $Ni_{50}Mn_{34}In_{16}$ [118]. Even though the structural transition temperatures are in general very sensitive to composition in the Ni-Mn-In alloys, T_c of the austenite is nearly composition-independent, a feature that holds even for the present case where the ferromagnetic fluctuations in the austenite phase are interrupted by the higher-temperature structural transition.

Besides increasing/decreasing the temperature of the sample, it was shown above that changing the external magnetic field can also drive the magneto-structural transition. However, for cases including a first-order transition through scanning the magnetic field, incorrect probing protocols can lead to spurious magnetic entropy changes [139, 141–145]. In order to correctly probe the phase transition, the following isothermal measurement was performed, resulting in curves such as plotted in Fig. 6.4 (main plot). The M-H measurements at a sequence of temperatures always included a loop bringing the sample below the lowest temperature, 325 K. That is to say, the materials were brought to complete martensite phase region before the next isothermal M-H measurements in order to avoid the hysteresis due to coexistence of two phase. The magnetization was recorded at each temperature with the field increasing to the maximum value and also while it was brought back to zero. Next, the temperature was reduced, bringing the sample into the complete martensite region, before going to the next measurement temperature. This was done with steps of $\Delta T = +3$ K near the phase transition, with the loop in temperature always performed at zero field before every isotherm. The magnetization for temperatures higher than 353 K and lower than 341 K shows similar paramagnetic behavior with no observable hysteresis or nonlinearity so only three representative curves are shown in Fig. 6.4.

6.4 Isothermal Entropy Change

In this section, we compare the two different experimental MCE entropy characterizations from calorimetric and magnetic measurement. The specific heat measurement across the transition was performed under fields of 1, 5, 7, 9 Tesla. The martensitic transition temperature is shifted to the lower temperature as the external field increases and it is consistent with the magnetization measurement under the corresponding fields. A schematic phase diagram of a typical inverse magnetocaloric effect material near the martensitic transition is shown in Fig. 6.5. The experimental measurement protocols for both methods are drawn as the dashed lines with arrows.

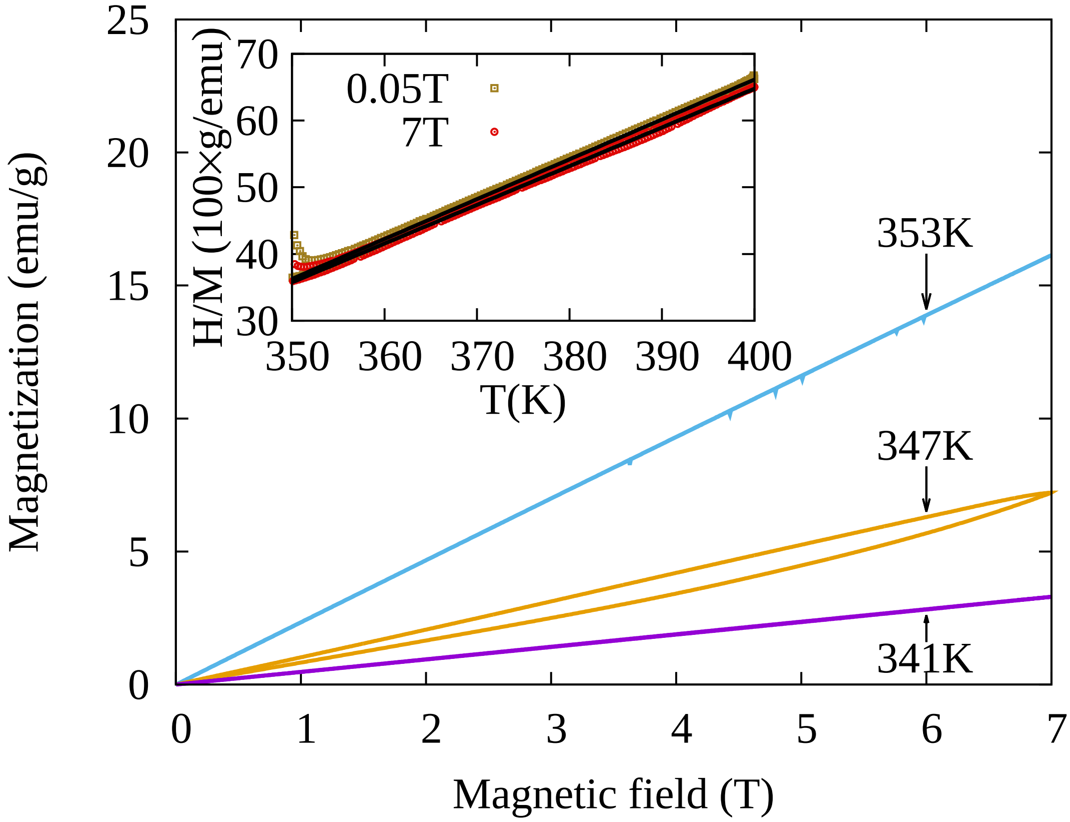

Figure 6.4: Three selected isothermal magnetization measurements for Ni50A sample. Magnetic hysteresis was only observed between 341 and 353 K (including the 347 K trace shown) and the error bars are smaller than the symbols. Inset: Isofield measurements for 0.05 T and 7 T, along with Curie-Weiss fittings (black lines) showing strong linearity of the results in the paramagnetic austenite phase [59].

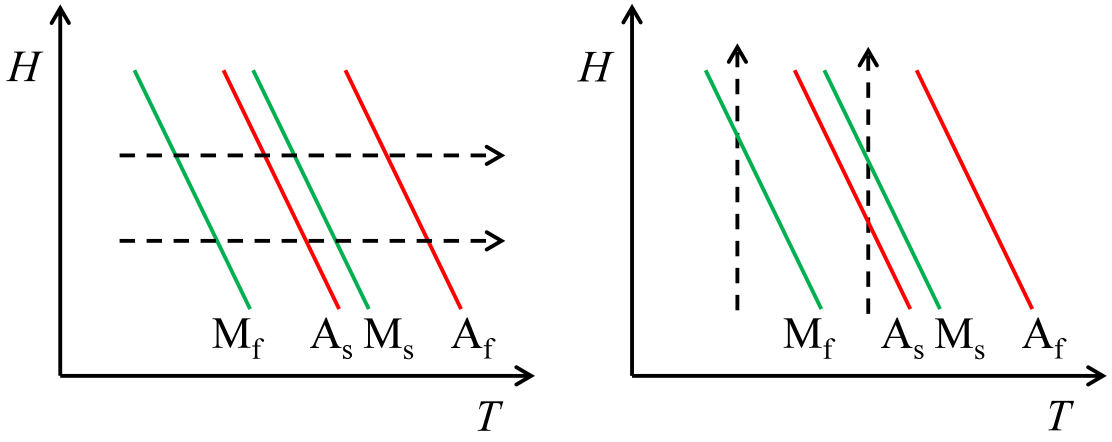

(a) Isofield specific heat measurement (b) Isothermal magnetization measurement

Figure 6.5: Schematic phase diagram of a typical inverse magnetocaloric effect material near the martensitic transition. Martensite starting and ending states are labelled as red lines while austenite starting and ending states are labelled as blue lines. (a) The horizontal dashed lines with arrows represents the isofield specific heat measurement. Each isofield measurement starts in the complete martensite phase and ends in the complete austenite phase. (b) The vertical dashed lines with arrows represents an isothermal magnetization measurement. The martensitic transition is not transformed completely by the available magnetic field shown. In order to do a comparison with the specific heat properly, we must go to complete martensite phase before proceeding to any higher temperature isothermal experiment.

Note that the martensitic transition in isofield measurements is entirely completed by the available magnetic field. In order to do the comparison with the specific heat properly, we must go to complete martensite phase before proceeding to any higher temperature isothermal experiment.

The entropy contribution due to the external field shown in Fig. 6.6 is obtained by using the relation [56].

$$\Delta S(T, 0 \to H) = \int_0^T \frac{C_p(T', H) - C_p(T', H=0)}{T'} dT'. \qquad (6.2)$$

Alternatively, an indirect experimental determination of the field-induced entropy can be evaluated from the isothermal magnetization by scanning the field with close enough temperature intervals [36, 57, 58]. This is done as a discrete approximation to the relation which is expressed as

$$\Delta S(T, 0 \to H) = \lim_{\Delta T \to 0} \frac{1}{\Delta T} \left[\int_0^H M(T + \Delta T, H') dH' - \int_0^B M(T, H') dH' \right]. \qquad (6.3)$$

The magnetic measurement were done by Nickolaus Bruno from the group of our collaborators from the Departments of Mechanical Engineering and Materials Science & Engineering in TAMU and the result of four analysis is shown as discrete symbols in Fig. 6.6.

It is important to recognize that the magnetic MCE measurements may be intrinsically erroneous if changes in the material are time dependent, i.e., if the response is not instantaneous, because the experiments were carried out in a sweeping magnetic field. In our experiment, we lowered the sweeping speed to a rate of 25 Oe/s for which the measurement results were found to be consistent with data taken at a higher speed, in order to avoid this situation.

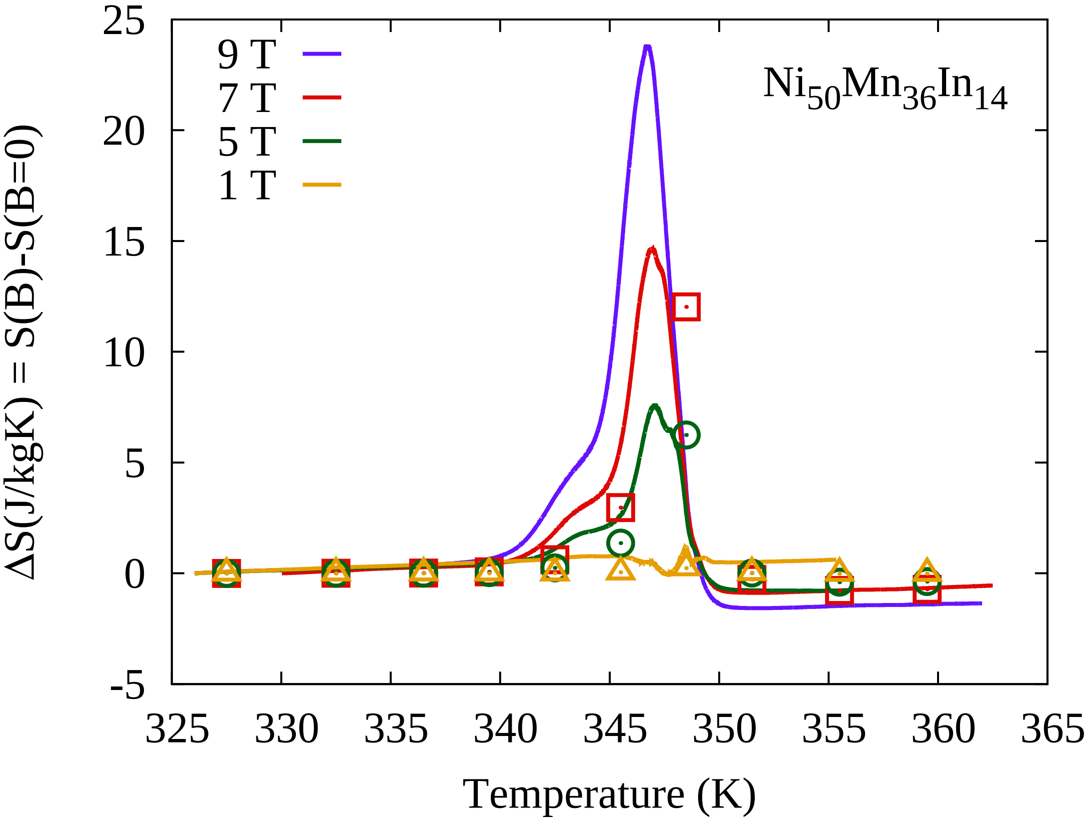

Figure 6.6: Reverse (martensite to austenite) field-induced entropy changes $(S(T, H) - S(T, 0))$ based on the heating-curve specific heat results (solid curve) for Ni50A ($Ni_{50}Mn_{36}In_{14}$) sample along with entropy results from the corresponding magnetic analysis (symbols).

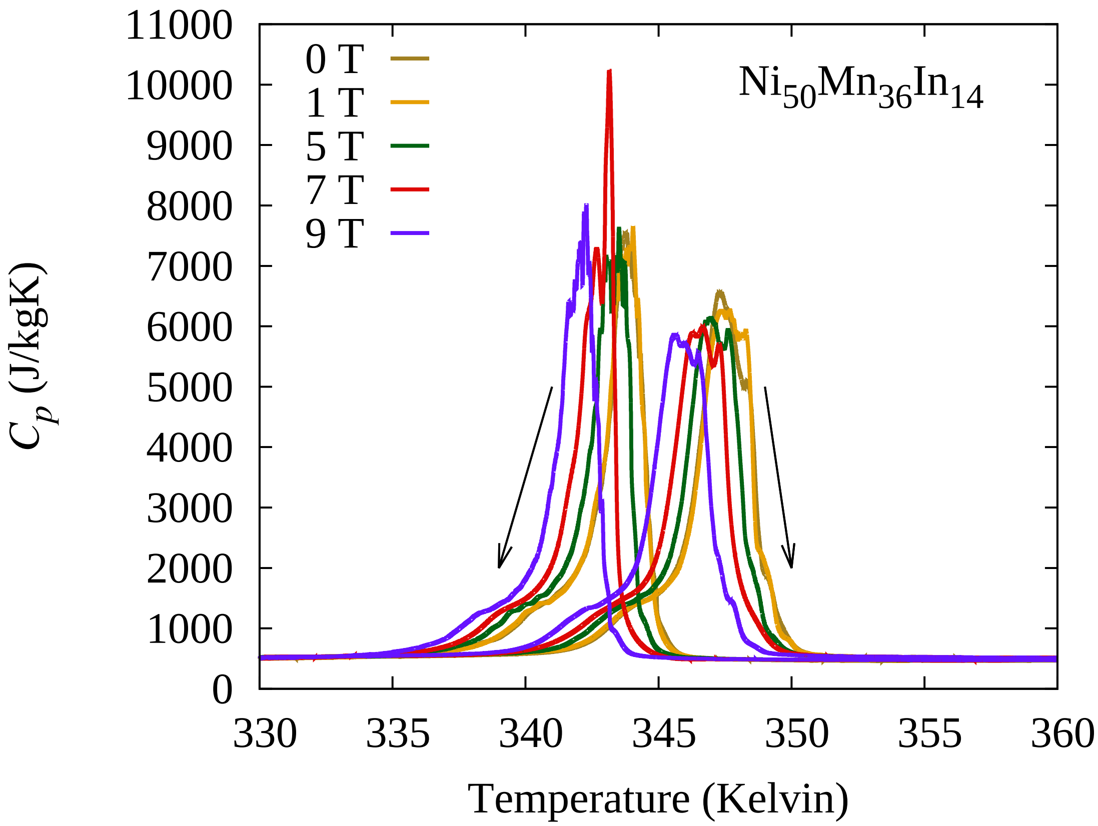

Figure 6.7: The specific heat measurement for $Ni_{50}Mn_{36}In_{14}$ (Ni50A) sample under various fields by using long-pulse method and the error bars are smaller than the symbols. Data both for heating and cooling protocol are shown as arrows.

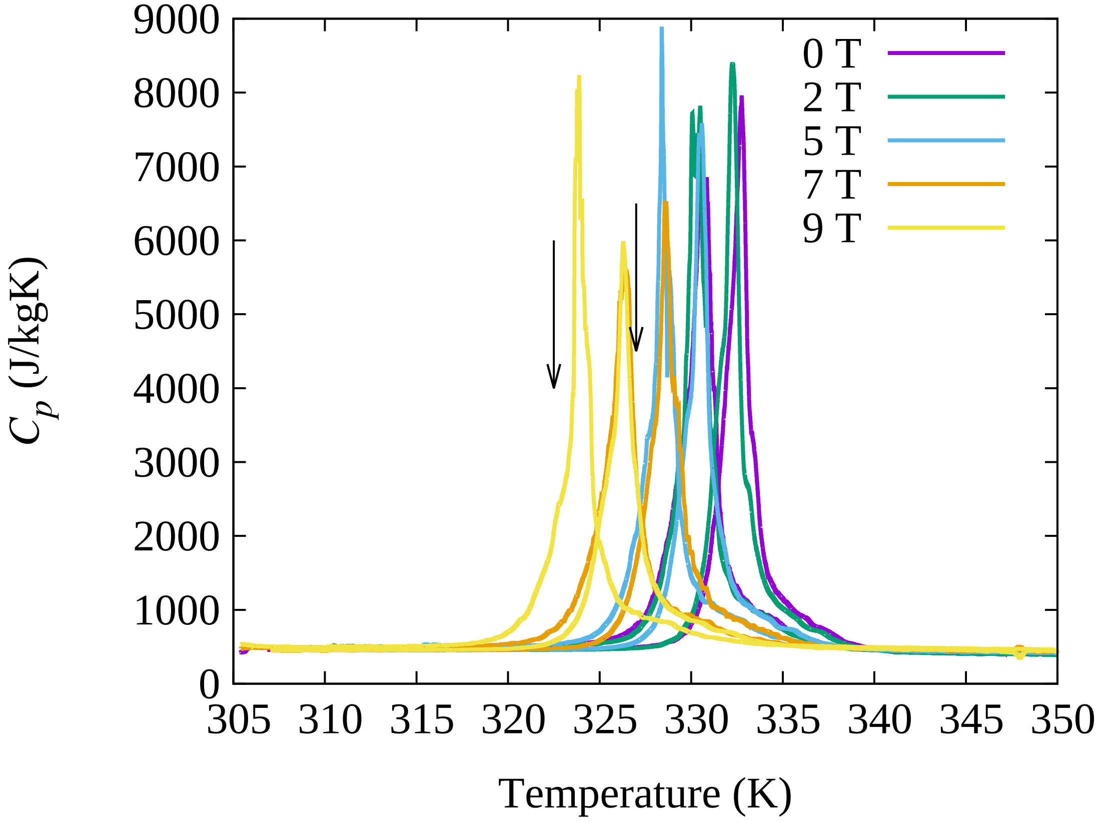

Figure 6.8: The specific heat measurement for $Ni_{50}Mn_{35.5}In_{14.5}$ sample under various fields by using long-pulse method and the error bars are smaller than the symbols. Data both for heating and cooling protocol are shown.

The specific heat results for two materials in various fields were shown in Fig. 6.7 and Fig. 6.8. Note that in these and following figures the data are reported per kg rather than per mole, following the convention from the literature on magnetiocaloric materials. The field-induced entropy change results obtained from these specific heat measurements while heating in various fields are shown in Fig. 6.6 and Fig. 6.9. In $Ni_{50}Mn_{36}In_{14}$ (Ni50A), the isothermal entropy obtained from magnetic measurements is also plotted in the same figure with the calorimetry results (Fig. 6.6) and they appear to be in good agreement with each other. A similar comparison was reported recently for other Ni-Mn-In materials [33, 59]. This result confirms that the isothermal entropy change obtained from the magnetic measurement is physically identical to the isothermal entropy change from the calorimetric measurement.

6.5 Relative Cooling Power Analysis

Another relevant quantity for evaluating the performance of MCE materials is the amount of transferred heat between cold and hot reservoirs in an ideal refrigeration cycle [60, 61]. This is referred to as the relative cooling power (RCP),

$$\mathrm{RCP}(H) = \int_{T_{cold}}^{T_{hot}} \Delta S(T, 0 \to H) dT,$$

where T_{cold} and T_{hot} are the temperatures of the two reservoirs. Therefore we can obtain RCP by calculating the area under the ΔS curves. Eq. 1.4 can also be rewritten [63] by using Eq. 1.3

$$\mathrm{RCP}(H) = \int_{T_{cold}}^{T_{hot}} \Delta S(T, 0 \to H) dT = \int_{0}^{H} M(T_{hot}, H') dH' - \int_{0}^{H} M(T_{cold}, H') dH'$$

which indicates that RCP can be determined from isothermal magnetic measurements at only two temperatures without knowing the details of the magnetic entropy

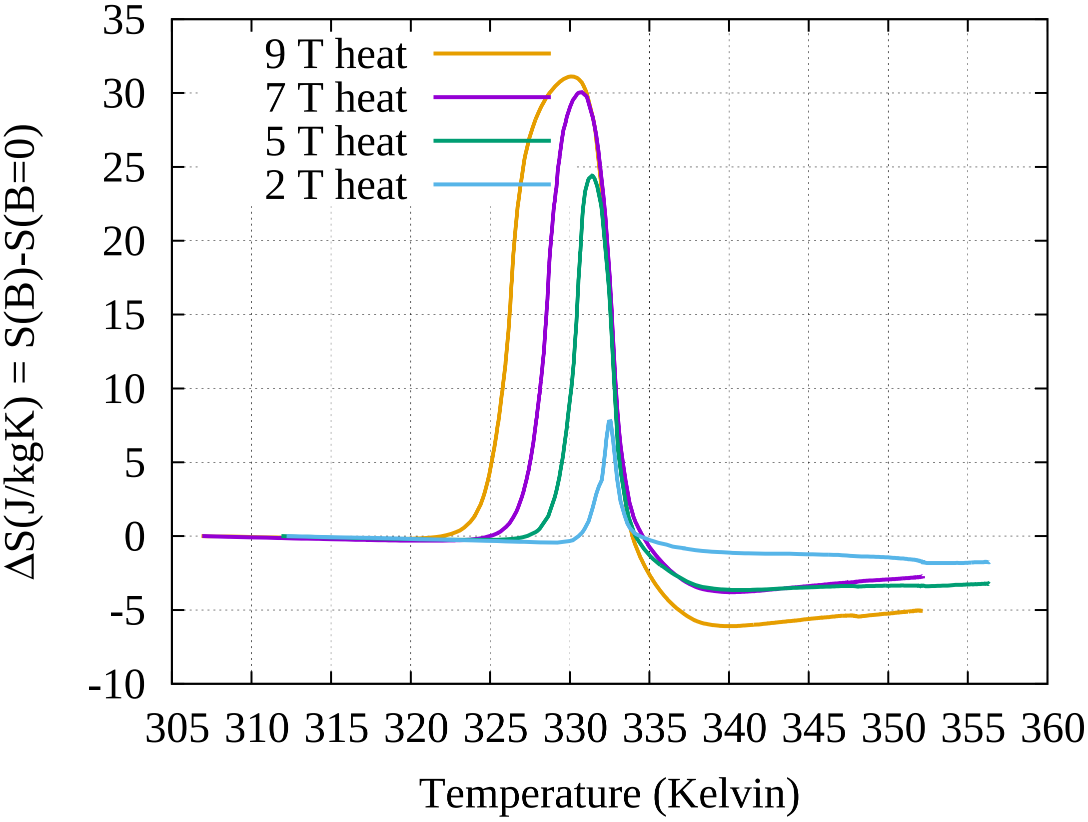

Figure 6.9: Reverse (martensite to austenite) field-induced entropy changes ($S(T,H) - S(T,0)$) based on the heating-curve specific heat results for Ni50B ($Ni_{50}Mn_{35.5}In_{14.5}$) sample.

at points between. Thus, despite the very sharp transition in this case, a larger number of magnetic isotherms (including cooling loops below the transformation) was not required to obtain RCP. On the other hand, since the entropy change obtained from specific heat data is much denser, we could calculate the entropy integral directly from the data. The results provide an additional useful comparison between methods.

Generally, the relative cooling power can be considered to be given by Eq. 1.4 or Eq. 1.5 evaluated with specific temperatures T_{hot} and T_{cold} bracketing the transition, corresponding to full martensite to austenite conversion. However, Fig. 6.10 displays the corresponding integrations evaluated with T_{hot} allowed to vary across the transition for a more generalized comparison. This provides an excellent comparison between the results obtained by both methods, since as Eq. 1.5 shows the structure of $\Delta S(T, 0 \rightarrow H)$ is properly accounted for even at intermediate temperatures where $M(H)$ has not been measured. The 1 T entropy change is small, giving an RCP integral (not shown) indistinguishable from the background. However, in 5 T and 7 T the results are in very good agreement, including the observed asymmetry of the ΔS peaks, which is reproduced with both methods. Also note that above 350 K, the ΔS integration curves slope downward since here in the paramagnetic phase, a conventional (non-inverse) MCE sets in.

To define the RCP in $Ni_{50}Mn_{36}In_{14}$ (Ni50A), in practice we chose the point where the integration curves of Fig. 6.10 reach a maximum, which is 349 K for all cases, at the temperature indicated in the figure. The resulting RCP values are 28 J/kg in 5 T, 48 J/kg in 7 T, and 79 J/kg in 9 T. For comparison RCP = 242 J/kg in 7 T has been reported for an annealed Ni-Co-Mn-Sn ribbon [142], and 104 J/kg in 5 T for bulk $Ni_{50}Mn_{34}In_{16}$ [42]. Therefore, for the Ni50A sample even though a large field-induced entropy change is observed, the RCP remains smaller than can be achieved

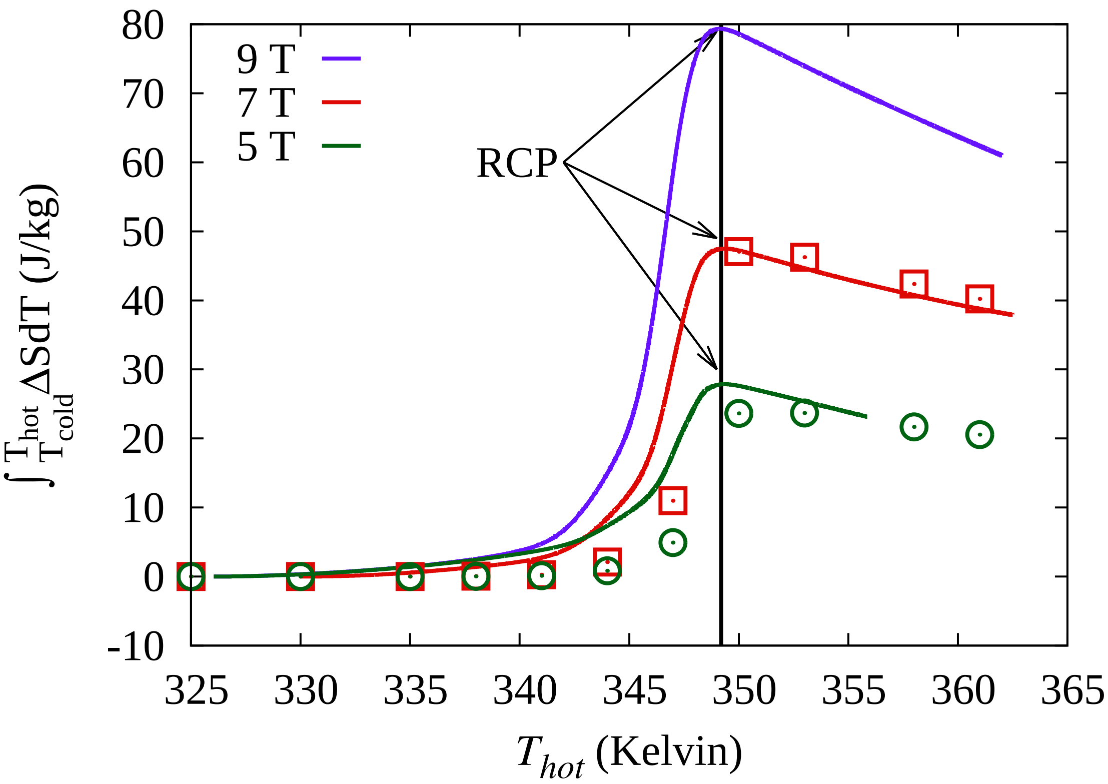

Figure 6.10: Integrated entropy obtained from specific heat (solid curves) for Ni50A ($Ni_{50}Mn_{36}In_{14}$) along with RCP for complete transformation, compared to values obtained from the difference of isothermal magnetic measurements (symbols).

in corresponding materials exhibiting a ferromagnetic austenite phase.

6.6 Molecular Field Theory Prediction

In this section, I will discuss the $\mathrm{Ni}_{50}\mathrm{Mn}_{36}\mathrm{In}_{14}$ (Ni50A) sample and $\mathrm{Ni}_{50}\mathrm{Mn}_{35.5}\mathrm{In}_{14.5}$ (Ni50B) separately. In fact, the measurement for $\mathrm{Ni}_{50}\mathrm{Mn}_{35.5}\mathrm{In}_{14.5}$ (Ni50B) samples were done several months after $\mathrm{Ni}_{50}\mathrm{Mn}_{36}\mathrm{In}_{14}$ (Ni50A), and the predictions in [59] turned out to work very well for this sample.

6.6.1 Theory and $Ni_{50}Mn_{36}In_{14}$ (Ni50A) Results

We now consider more generally the RCP obtainable in similar alloy systems with the transformation temperature T_m closer to T_c, where the austenite paramagnetic response will be stronger. As we established, the $\mathrm{Ni}_{50}\mathrm{Mn}_{36}\mathrm{In}_{14}$ austenite is described very accurately as a Curie-law paramagnetic with each Mn having a spin fitted to $J = 2.0$, and ferromagnetic correlations corresponding to $T_c = 289$ K. Similar behavior is observed in other Ni-Mn-In systems, and as noted above T_c is found to be relatively independent of composition. For the present alloy, since the magnetization curves are linear close to the transition in both phases (Fig. 6.4), Eq. 1.5 can be written, $\mathrm{RCP}(H) = \Delta\chi H^2/2$, with $\chi = M/H$ being the susceptibility. Based on the observed small martensite magnetic response, its contribution to RCP in 9 T is $-\chi_m H^2/2 = -21$ J/kg, which decreases rapidly at lower fields. Closer to T_c, the paramagnetic response of the austenite will become nonlinear, and to address this situation we have adopted a mean field approach [146]. Except for the critical region very close to T_c in small fields, this gives a good approximation for the spin polarization, and as long as T remains above T_c, coercivity effects need not be considered.

The inset of Fig. 6.11 shows representative spin polarization results obtained following a standard derivation [146], with the mean spin following a Brillouin function containing the applied magnetic field enhanced by the local ferromagnetic exchange field. We assumed each Mn to have a local moment with $J = 2$ and $g = 2$, coinciding with the magnetization fit, and used $T_c = 289$ K as measured, which determines the size of the exchange field. The magnetization is obtained from the average spin using the known moment per Mn, along with the Mn-ion density per kg for $Ni_{50}Mn_{36}In_{14}$. No adjustable parameters are needed to obtain $\int MdH$, which is the integral appearing in Eq. 1.5. Fig. 6.11 shows RCP results obtained this way vs. T_m/T_c, where the temperature at which the integration is evaluated is assumed to match T_m for different compositions along the horizontal axis. In this calculation we also assumed that the martensite-phase contribution to RCP, $-\chi_m H^2/2$, remains unchanged. While in practice this term will vary with processing, note that this term is in any case small, particularly near T_c. The circles on the graph represent the RCP extracted from specific heat for $Ni_{50}Mn_{36}In_{14}$ (with $T_m/T_c = 1.21$ as obtained in our analysis for this material). These are in a very good agreement with the calculated curves from the molecular field theory as shown in Fig. 6.11.

More generally, Fig. 6.11 shows the RCP that should be attainable in compositions similar to $Ni_{50}Mn_{36}In_{14}$ if T_m is adjusted along the horizontal axis through composition or local ordering changes. In this discussion, only magnetic contributions to the entropy are considered. For T_m close to T_c the RCP values become comparable to those reported in other Ni-Mn-X materials, as described above. Note that an approach typically used for these materials has been to maximize the austenite magnetization, for example in reference [14] by substitution of Co, in order to enhance the RCP. However, these results predict that compositions with $T_m \sim Tc$ having small or zero spontaneous magnetization in both phases may still exhibit comparable results. Since magnetic coercivity effects will not contribute to the thermal hysteresis, optimizing materials of this type may represent a promising approach for obtaining useful MCE materials.

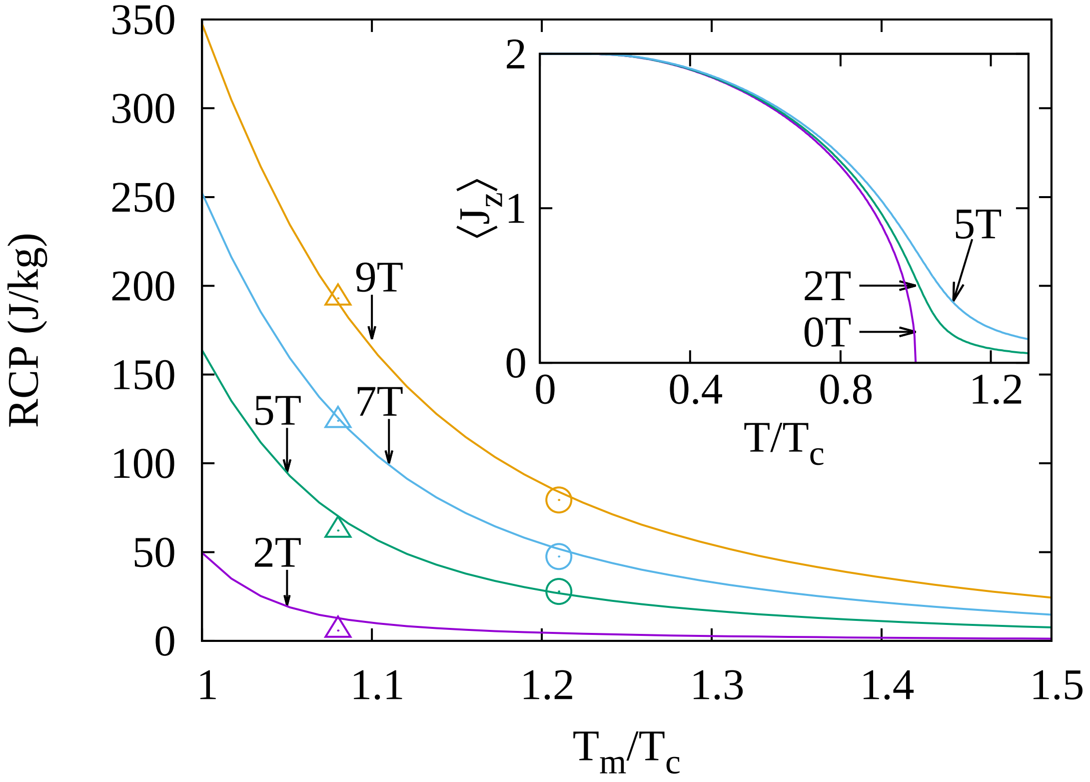

Figure 6.11: Relative cooling power vs. martensitic transformation temperature calculated for Ni-Mn-In compositions with paramagnetic austenite phase i.e. $T_m/Tc \geq 1$, as described in text. The circles represent the experimental RCP for $Ni_{50}Mn_{36}In_{14}$ (Ni50A) while the triangles represent those for $Ni_{50}Mn_{35.5}In_{14.5}$ (Ni50B). Inset: computed austenite average spin moment for the indicated fields.

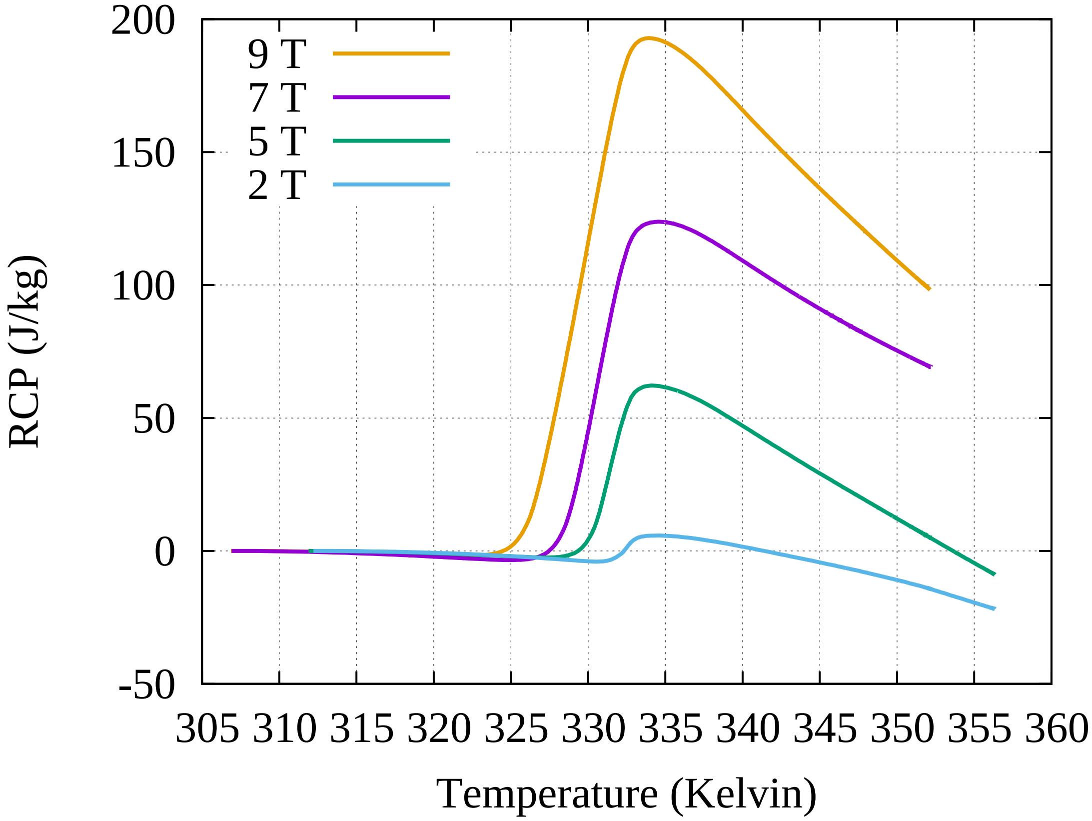

Figure 6.12: Integrated entropy obtained from specific heat for $Ni_{50}Mn_{35.5}In_{14.5}$ (Ni50B).

6.6.2 $Ni_{50}Mn_{35.5}In_{14.5}$ (Ni50B) Results

After confirming the agreement between the two experiments in $Ni_{50}Mn_{36}In_{14}$, we established confidently that the magnetic and calorimetric measurement yield consistent results. In the $Ni_{50}Mn_{35.5}In_{14.5}$ sample, we followed up with only the calorimetric measurements as was shown in Fig. 6.8. The integrated entropy obtained from the calorimetric measurement is shown in Fig. 6.12.

Picking out the peak of the integrated entropy as before as T_{hot}, the corresponding RCPs are obtained and are plotted as the triangles in Fig. 6.11. With $T_m/T_c = 1.08$

for this sample, which is smaller than $T_m/T_c = 1.21$ in $\mathrm{Ni_{50}Mn_{36}In_{14}}$, the RCP results are found to be large as expected in the molecular field theory. As shown in Fig. 6.12 these results are indeed in excellent agreement with the molecular field model previously developed for these materials as described in the last section. Further, we note that our collaborators, after developing the heat treatment for this sample [147], found an extremely small thermal hysteresis in this sample of 3 K, indicating that this may indeed be a promising route for development of useful materials for magnetocaloric applications.

6.7 Summary

We examined the magnetocaloric effect in $\mathrm{Ni_{50}Mn_{36}In_{14}}$ and $\mathrm{Ni_{50}Mn_{35.5}In_{14.5}}$, heat treated to exhibit a narrow structural phase transition to the martensitic phase near 345 K. Above the transformation this composition is paramagnetic with no spontaneous magnetization, unlike similar compositions typically studied with somewhat lower structural transition temperatures. Field-induced entropy changes were analyzed both through indirect magnetic and direct calorimetric measurements. For the latter, we demonstrated a procedure based on relaxation calorimetry using extended heating and cooling curves extending across the first-order phase transition. The results are in excellent agreement with magnetization-based methods, which provide a firm basis for the analytic evaluation of field-induced entropy changes. In particular, the relative cooling power (RCP) can be assessed in this way, and the associated analysis shows that a large RCP may be generated in materials with the structural transition tuned very close to the Curie temperature. Follow-up measurements were indeed in excellent agreement with the predictions of this model.

7. CONCLUSION

The recent discovery of giant magnetocaloric effects at around room temperature has triggered research and development aimed to produce a magnetic refrigerator that operates at ambient temperatures. Among new magnetocaloric materials, Ni-Mn-In Heusler alloys have attracted considerable attention as candidates for novel rare-earth free magnetic refrigerants. In order to fully understand the properties of the martensitic phase transition in Ni-Mn-In Heusler alloys and its influence on the MCE properties, we prepare four samples with different compositions which are $Ni_{50}Mn_{36}In_{14}$, $Ni_{50}Mn_{35.5}In_{14.5}$, $Ni_{48}Mn_{35}In_{17}$ and $Ni_{48}Mn_{38}In_{14}$. The former two samples exhibit a paramagnetic to antiferromagnetic transition from high temperature to low temperature while the later two samples exhibit an additional ferromagnetic transition in the high temperature phase.

Calorimetric experiments were performed in order to understand the total entropy of the system and to compare with magnetization measurements. A modified calorimetric analysis technique was developed in order to properly probe the first order transition. We observed the complete martensitic transformation by sweeping of the temperature under zero field conditions for the four samples. The entropy of the systems are obtained from $S = \int \frac{C(T)}{T} dT$ which includes contributions due to magnetism (S_{mag}), lattice vibrations (S_{vib}) and conduction electrons (S_{el}):

$$S_{tot} = S_{mag} + S_{vib} + S_{el}. \tag{7.1}$$

In the $Ni_{50}Mn_{36}In_{14}$ and $Ni_{50}Mn_{35.5}In_{14.5}$ samples, this includes an additional contribution due to the magneto-elastic coupling, which can be explained in terms of the renormalization of the Debye temperature coupled with magnetism. The origin of the correlation between the magnetic transitions and the lattice expansion, and the influence of magnetostructural coupling on MCE have been the focus of several previous studies. However, magnetization experiments were more often conducted rather than calorimetric measurements. However, the magnetization data can only give the field-induced entropy change instead of the total entropy of the material. On the other hand our measurements represent the first time in the literature as far as we are aware of the observation of the excess entropy directly from calorimetric measurements.

Besides these results, we analyzed the field-induced entropy change through both magnetization and direct field-dependent calorimetry measurements in $Ni_{50}Mn_{36}In_{14}$ and $Ni_{50}Mn_{35.5}In_{14.5}$. The results provide a firm basis for the analytic evaluation of field-induced entropy changes and relative cooling power in related materials. In particular, we predict the relative cooling power in the molecular field theory, and the associated analysis shows that a large RCP may be generated in materials with the structural transition tuned very close to the Curie temperature.

REFERENCES

[1] E. Warburg, Annal. Phys. **249**, 141 (1881).

[2] C. Zimm et al., Description and Performance of a Near-Room Temperature Magnetic Refrigerator, in *Advances in Cryogenic Engineering*, edited by P. Kittel, volume 43, pages 1759–1766, Springer US, 1998.

[3] K. A. Gschneidner, Jr. and V. K. Pecharsky, Int. J. Refrig. **31**, 945 (2008).

[4] G. V. Brown, J. Appl. Phys. **47**, 3673 (1976).

[5] V. K. Pecharsky and K. A. Gschneidner, Jr., Phys. Rev. Lett. **78**, 4494 (1997).

[6] H. Wada and Y. Tanabe, Appl. Phys. Lett. **79**, 3302 (2001).

[7] F.-x. Hu et al., Appl. Phys. Lett. **78**, 3675 (2001).

[8] A. Fujita, S. Fujieda, Y. Hasegawa, and K. Fukamichi, Phys. Rev. B **67**, 104416 (2003).

[9] O. Tegus, E. Brück, K. H. J. Buschow, and F. R. De Boer, Nature **415**, 150 (2002).

[10] N. T. Trung et al., Appl. Phys. Lett. **94**, 102513 (2009).

[11] N. H. Dung et al., Adv. Energy Mater. **1**, 1215 (2011).

[12] T. Krenke et al., Nat. Mater. **4**, 450 (2005).

[13] E. Liu et al., Nat. Commun. **3**, 873 (2012).

[14] J. Liu, T. Gottschall, K. P. Skokov, J. D. Moore, and O. Gutfleisch, Nat. Mater. **11**, 620 (2012).

[15] N. T. Trung, L. Zhang, L. Caron, K. H. J. Buschow, and E. Brück, Appl. Phys. Lett. **96**, 172504 (2010).

[16] P. J. Shamberger, *Engineering Phase Changes in Heusler Alloys: Towards Better Magnetic Refrigerants*, PhD thesis, University of Washington, 2010.

[17] A. M. Tishin and Y. I. Spichkin, *The Magnetocaloric Effect and its Applications*, Condensed Matter Physics, Taylor & Francis, 2003.

[18] A. M. Tishin, Cryogenics **30**, 127 (1990).

[19] J. R. Gómez, R. F. Garcia, A. D. M. Catoira, and M. R. Gómez, Renew. Sust. Energ. Rev. **17**, 74 (2013).

[20] B. F. Yu, Q. Gao, B. Zhang, X. Z. Meng, and Z. Chen, Int. J. Refrig. **26**, 622 (2003).

[21] K. A. Gschneidner, Jr. and V. K. Pecharsky, Annu. Rev. Mater. Sci. **30**, 387 (2000).

[22] K. A. Gschneidner, Jr., V. K. Pecharsky, and A. O. Tsokol, Rep. Prog. Phys. **68**, 1479 (2005).

[23] E. Brück, J. Phys. D: Appl. Phys. **38**, R381 (2005).

[24] V. K. Pecharsky and K. A. Gschneidner, Jr., J. Alloys Compd. **260**, 98 (1997).

[25] V. K. Pecharsky and K. A. Gschneidner, Jr., Appl. Phys. Lett. **70**, 3299 (1997).

[26] V. K. Pecharsky, K. A. Gschneidner, Jr., A. O. Pecharsky, and A. M. Tishin, Phys. Rev. B **64**, 144406 (2001).

[27] A. O. Pecharsky, K. A. Gschneidner, Jr., and V. K. Pecharsky, J. Magn. Magn. Mater. **267**, 60 (2003).

[28] V. Provenzano, A. J. Shapiro, and R. D. Shull, Nature **429**, 853 (2004).

[29] A. Giguère et al., Phys. Rev. Lett. **83**, 2262 (1999).

[30] H. D. Chopra, C. Ji, and V. V. Kokorin, Phys. Rev. B **61**, R14913 (2000).

[31] Y. Takamura, R. Nakane, and S. Sugahara, J. Appl. Phys. **105**, 07B109 (2009).

[32] R. Kainuma et al., Nature **439**, 957 (2006).

[33] F. Guillou et al., J. Phys. D: Appl. Phys. **45**, 255001 (2012).

[34] V. A. Chernenko et al., J. Magn. Magn. Mater. **324**, 3519 (2012).

[35] V. Recarte, J. I. Pérez-Landazábal, S. Kustov, and E. Cesari, J. Appl. Phys.

107, 053501 (2010).

[36] A. Planes, L. Mañosa, and M. Acet, J. Phys.: Condens. Matter **21**, 233201 (2009).

[37] K. Oikawa et al., Appl. Phys. Lett. **88**, 122507 (2006).

[38] M. Khan, N. Ali, and S. Stadler, J. Appl. Phys. **101**, 053919 (2007).

[39] F. S. Liu et al., J. Magn. Magn. Mater. **324**, 514 (2012).

[40] F.-x. Hu, J.-r. Sun, G.-h. Wu, and B.-g. Shen, J. Appl. Phys. **90**, 5216 (2001).

[41] A. B. Pakhomov, C. Y. Wong, X. X. Zhang, G. H. Wen, and G. H. Wu, IEEE Trans. Magn. **37**, 2718 (2001).

[42] V. K. Sharma, M. K. Chattopadhyay, and S. B. Roy, J. Phys. D: Appl. Phys. **40**, 1869 (2007).

[43] A. Planes and L. Mañosa, Ferromagnetic shape-memory alloys, in *Materials science forum*, volume 512, pages 145–152, Trans. Tech. Publ., 2006.

[44] T. Krenke et al., Phys. Rev. B **72**, 014412 (2005).

[45] T. Krenke et al., Phys. Rev. B **73**, 174413 (2006).

[46] J. Du et al., J. Phys. D: Appl. Phys. **40**, 5523 (2007).

[47] V. D. Buchelnikov and V. V. Sokolovskiy, Phys. Met. Metallogr. **112**, 633 (2011).

[48] L. Pytlik and A. Zieba, J. Magn. Magn. Mater. **51**, 199 (1985).

[49] H. Fjellvåg and A. Kjekshus, Acta Chem. Scand. **38A**, 1 (1984).

[50] C. Kuhrt, T. Schittny, and K. Brner, Phys. Status Solidi A **91**, 105 (1985).

[51] H. Wada et al., Physica B **328**, 114 (2003).

[52] H. Wada, K. Taniguchi, and Y. Tanabe, Mater. Trans. **43**, 73 (2002).

[53] A. Fujita, Y. Akamatsu, and K. Fukamichi, J. Appl. Phys. **85**, 4756 (1999).

[54] B. G. Shen, J. R. Sun, F. X. Hu, H. W. Zhang, and Z. H. Cheng, Adv. Mater. **21**, 4545 (2009).

[55] K. A. Gschneidner, Jr., Y. Mudryk, and V. K. Pecharsky, Scr. Mater. **67**, 572 (2012).

[56] N. A. de Oliveira and P. J. von Ranke, Phys. Rev. B **77**, 214439 (2008).

[57] K. H. J. Buschow, *Handbook of Magnetic Materials*, Elsevier Science, 2013.

[58] V. K. Pecharsky and K. A. Gschneidner, Jr., J. Appl. Phys. **86**, 565 (1999).

[59] J.-H. Chen et al., J. Appl. Phys. **116**, 203901 (2014).

[60] V. K. Pecharsky and K. A. Gschneidner, Jr., J. Appl. Phys. **90**, 4614 (2001).

[61] K. A. Gschneidner, Jr., V. K. Pecharsky, A. O., and C. B. Zimm, Recent developments in magnetic refrigeration, in *Materials science forum*, volume 315, pages 69–76, Trans. Tech. Publ., 1999.

[62] M. D. Kuz'min and A. M. Tishin, Cryogenics **33**, 868 (1993).

[63] J. S. Amaral and V. S. Amaral, J. Magn. Magn. Mater. **322**, 1552 (2010).

[64] W. D. Callister, *Materials Science and Engineering: An Introduction*, Wiley Plus Products, John Wiley & Sons, Incorporated, 2006.

[65] C. Kittel, *Introduction to Solid State Physics*, Wiley, 2004.

[66] S. Chikazumi and C. D. Graham, *Physics of Ferromagnetism*, International Series of Monographs on Physics, Clarendon Press, 1997.

[67] R. Serway and J. Jewett, *Physics for Scientists and Engineers*, Cengage Learning, 2007.

[68] J. Patterson and B. Bailey, Lattice Vibrations and Thermal Properties, in *Solid-State Physics*, chapter 2, pages 41–112, Springer Berlin Heidelberg, 2010.

[69] J. H. Van Vleck, J. Chem. Phys. **9**, 85 (1941).

[70] A. B. Lidiard, Rep. Prog. Phys. **17**, 201 (1954).

[71] J. H. Van Vleck, *The theory of electric and magnetic susceptibilities*, Clarendon Press Oxford, 1932.

[72] J. E. Greedan et al., Phys. Rev. B **54**, 7189 (1996).

[73] A. Maignan, U. Varadaraju, F. Millange, and B. Raveau, J. Magn. Magn. Mater. **168**, L237 (1997).

[74] A. Maignan, A. Sundaresan, U. V. Varadaraju, and B. Raveau, J. Magn. Magn. Mater. **184**, 83 (1998).

[75] X. L. Wang, J. Horvat, H. K. Liu, and S. X. Dou, J. Magn. Magn. Mater. **182**, L1 (1998).

[76] J. Pérez, J. García, J. Blasco, and J. Stankiewicz, Phys. Rev. Lett. **80**, 2401 (1998).

[77] I. O. Troyanchuk, N. V. Samsonenko, E. F. Shapovalova, H. Szymczak, and A. Nabialek, Mater. Res. Bull. **32**, 67 (1997).

[78] H. Onodera, H. Kobayashi, H. Yamauchi, M. Ohashi, and Y. Yamaguchi, J. Magn. Magn. Mater. **170**, 201 (1997).

[79] S. Nishigori, Y. Hirooka, and T. Ito, J. Magn. Magn. Mater. **177-181, Part 1**, 137 (1998).

[80] W. Greiner, D. Rischke, L. Neise, and H. Stöcker, *Thermodynamics and Statistical Mechanics*, Classical Theoretical Physics, Springer New York, 2000.

[81] M. W. Zemansky and R. Dittman, *Heat and Thermodynamics: An Intermediate Textbook*, International Series in Pure and Applied Physics, McGraw-Hill, 1997.

[82] A. Arrott, Phys. Rev. **108**, 1394 (1957).

[83] I. Yeung, R. M. Roshko, and G. Williams, Phys. Rev. B **34**, 3456 (1986).

[84] R. L. Hadimani, Y. Melikhov, J. E. Snyder, and D. C. Jiles, J. Magn. Magn. Mater. **320**, e696 (2008).

[85] P. J. v. Ranke, N. A. de Oliveira, C. Mello, A. M. G. Carvalho, and S. Gama, Phys. Rev. B **71**, 054410 (2005).

[86] B. Linder, *Thermodynamics and Introductory Statistical Mechanics*, Wiley

InterScience online books, Wiley, 2004.

[87] E. Palacios et al., Entropy **17**, 1236 (2015).

[88] T. Kihara, X. Xu, W. Ito, R. Kainuma, and M. Tokunaga, Phys. Rev. B **90**, 214409 (2014).

[89] C. Kittel, Phys. Rev. **120**, 335 (1960).

[90] W. H. Cloud, T. A. Bither, and T. J. Swoboda, J. Appl. Phys. **32**, S55 (1961).

[91] T. A. Bither, P. H. L. Walter, W. H. Cloud, T. J. Swoboda, and P. E. Bierstedt, J. Appl. Phys. **33**, 1346 (1962).

[92] H. S. Jarrett, Phys. Rev. **134**, A942 (1964).

[93] P. H. L. Walter, J. Appl. Phys. **35**, 938 (1964).

[94] J. S. Kouvel, J. Appl. Phys. **37**, 1257 (1966).

[95] J. B. McKinnon, D. Melville, and E. W. Lee, J. Phys. C **3**, S46 (1970).

[96] B. Li et al., Appl. Phys. Lett. **95**, 172506 (2009).

[97] M. P. Annaorazov, S. A. Nikitin, A. L. Tyurin, K. A. Asatryan, and A. K. Dovletov, J. Appl. Phys. **79**, 1689 (1996).

[98] C. P. Bean and D. S. Rodbell, Phys. Rev. **126**, 104 (1962).

[99] T. Tegusi, *Novel Materials for Magnetic Refrigeration*, PhD thesis, Van der Waals-Zeeman Institute, 2003.

[100] R. W. De Blois and D. S. Rodbell, Phys. Rev. **130**, 1347 (1963).

[101] R. Zach, M. Guillot, and J. Toboa, J. Appl. Phys. **83**, 7237 (1998).

[102] N. A. de Oliveira and P. J. von Ranke, Phys. Rep. **489**, 89 (2010).

[103] P. K. Thiruvikraman, *Study of Electronic Phase Transitionsat High Pressures*, PhD thesis, Manjabre University, 1999.

[104] E. Gmelin, Thermochim. Acta **29**, 1 (1979).

[105] P. F. Sullivan and G. Seidel, Phys. Rev. **173**, 679 (1968).

[106] Y. Kohama, C. Marcenat, T. Klein, and M. Jaime, Rev. Sci. Instrum. **81**,

104902 (2010).

[107] R. Bachmann et al., Rev. Sci. Instrum. **43**, 205 (1972).

[108] J. S. Hwang, K. J. Lin, and C. Tien, Rev. Sci. Instrum. **68**, 94 (1997).

[109] *Physical Property Measurement System Heat Capacity Option Users Manual*, 2013.

[110] V. Hardy, Y. Bréard, and C. Martin, J. Phys.: Condens. Matter **21**, 075403 (2009).

[111] H. Suzuki, A. Inaba, and C. Meingast, Cryogenics **50**, 693 (2010).

[112] G. Grosso and G. P. Parravicini, *Solid State Physics*, Elsevier Science, 2000.

[113] E. S. R. Gopal, *Specific Heats at Low Temperatures*, The International cryogenics monograph series, Plenum Press, 1966.

[114] D. K. C. MacDonald, *Introductory Statistical Mechanics for Physicists*, Dover Books on Physics Series, Dover Publications, 2006.

[115] J. E. Mayer and M. G. Mayer, *Statistical Mechanics*, J. Wiley & Sons, Incorporated, 1940.

[116] L. H. Bennett et al., J. Alloys Compd. **525**, 34 (2012).

[117] T. Krenke et al., Phys. Rev. B **75**, 104414 (2007).

[118] Y. Sutou et al., Appl. Phys. Lett. **85**, 4358 (2004).

[119] Z. D. Han et al., Appl. Phys. Lett. **89**, 182507 (2006).

[120] L. Tocado, E. Palacios, and R. Burriel, J. Therm. Anal. Calorim. **84**, 213 (2006).

[121] L. F. Bao et al., Appl. Phys. Lett. **101**, 162406 (2012).

[122] Y. J. Huang, Q. D. Hu, and J. G. Li, Appl. Phys. Lett. **101**, 222403 (2012).

[123] J. S. Dugdale, *Entropy And Its Physical Meaning*, Taylor & Francis, 1996.

[124] J. Li et al., Physica B **409**, 35 (2013).

[125] C.-M. Li et al., Phys. Rev. B **86**, 214205 (2012).

[126] W. Ito et al., Appl. Phys. Lett. **97**, 242512 (2010).

[127] S. K. Ghatak, M. Avignon, and K. H. Bennemann, J. Phys. F: Met. Phys. **6**, 1441 (1976).

[128] J. Kübler, A. R. William, and C. B. Sommers, Phys. Rev. B **28**, 1745 (1983).

[129] D. Y. Cong, S. Roth, and L. Schultz, Acta Mater. **60**, 5335 (2012).

[130] U. Mizutani, *Introduction to the Electron Theory of Metals*, Cambridge University Press, 2001.

[131] M. Blackman, Rep. Prog. Phys. **8**, 11 (1941).

[132] J. Monroe, private communication, 2015.

[133] G. L. F. Fraga, D. E. Brandão, and J. G. Sereni, J. Magn. Magn. Mater. **102**, 199 (1991).

[134] V. V. Khovailo, K. Oikawa, T. Abe, and T. Takagi, J. Appl. Phys. **93**, 8483 (2003).

[135] A. N. Vasiliev et al., J. Phys. D: Appl. Phys. **43**, 055004 (2010).

[136] G. J. Liu et al., Appl. Phys. Lett. **88**, 212505 (2006).

[137] Z. Li et al., Solid State Commun. **203**, 81 (2015).

[138] M. Pugaczowa-Michalska, Solid State Commun. **140**, 251 (2006).

[139] V. Franco, J. S. Blázquez, B. Ingale, and A. Conde, Annu. Rev. Mater. Res. **42**, 305 (2012).

[140] V. K. Pecharsky and K. A. Gschneidner, Jr., J. Magn. Magn. Mater. **200**, 44 (1999).

[141] L. Caron et al., J. Magn. Magn. Mater. **321**, 3559 (2009).

[142] N. M. Bruno et al., Acta Mater. **74**, 66 (2014).

[143] H.-W. Zhang et al., J. Magn. Magn. Mater. **320**, 1879 (2008).

[144] L. Tocado, E. Palacios, and R. Burriel, J. Appl. Phys. **105**, 093918 (2009).

[145] A. M. G. Carvalho, A. A. Coelho, P. J. Von Ranke, and C. S. Alves, J. Alloys

Compd. **509**, 3452 (2011).

[146] S. Blundell, *Magnetism in Condensed Matter*, Oxford University Press, 2001.

[147] N. M. Bruno, private communication, 2015.